U.PORTO
FEUP FACULDADE DE ENGENHARIA
UNIVERSIDADE DO PORTO

Modelling and analysis of composite joint reinforced by composite fastener

André Macedo Leite

Supervisor:

Prof. Dr. Shijun Guo

Prof. Dr. António Torres Marques

A Thesis submitted for the degree of

Master of Science in Mechanical Engineering

to the Faculty of Engineering, University of Porto

Porto, June 2016

Abstract

Through this work, a new design of a composite countersunk rivet made of rolled laminates for aeronautical application is proposed and numerically analysed. Two distinct categories of three-dimensional solid finite element models have been developed.

The first category is based on four composite single lap joints models subjected to shear, two of them are adhesively bonded whereas the other two are bonded-bolted. One of the bonded-bolted model is fastened with the composite countersunk rivet while the other one is fastened with a countersunk titanium rivet. One of the adhesively bonded joints has the countersunk hole geometry drilled on its structure. The modelling of progressively adhesive damage is included on these category through a cohesive zone model (CZM).

The comparison between those models allows the investigation of the load carrying ability from this new fastener when the adhesive damage is occurring, comparatively to the bonding and metallic bonding-bolting. A detailed comparison has been performed between the contribution of the composite rivet and the titanium rivet for the shear requesting. The main purposes of this first category is to study the efficiency of this new rivet and whether this technique is viable comparatively to the analogous joining techniques when the bonding link is compromised.

The second category of models is composed by a group of four large scale models based on an aircraft wing box section. Those models have a bonded-bolted joint between the skin and one rib of the wing box and along this length the new fastener's design is distributed through six positions. Each model has a specific level of adhesive's flaw in

order to simulate four levels of adhesive damage supposedly produced by random events. On this category the structures are subjected to typical pulling load applied on the skin.

The main purpose of that second category is to study the effectiveness of the composite rivet to reduce the stress level on its surrounding when applied on a damaged wing section. If some hazard occurrences damage the adhesive layer, the knowledge of the stress redistribution within the rivets surfaces are an important baseline for understanding if the composite rivets have the ability to handle, on a structural level, the consequences of an adhesive disbond. Also the stress distributions on adhesive layers are investigated and correlated with the role of the composite rivets.

Keywords: Composite Fastener, Rivet Fastening, Finite Element Analysis, Composite Single Lap Joint, Composite Bonded-Bolted Joint, Wing Box, Composite Rivet, Joint Reinforcement, *Abaqus®*, CZM.

Resumo

Através deste trabalho, um novo design de um rebite em material compósito de cabeça escareada para aplicação aeronáutica, produzido através do enrolamento de um laminado, é proposto e analisado com recurso a métodos numéricos. Foram desenvolvidas duas categorias distintas de modelos 3D de elementos finitos.

A primeira categoria é baseada em quatro modelos de juntas de sobreposição simples em compósito sujeitas ao corte, duas das quais são coladas apenas com recurso a um adesivo enquanto que as restantes são também coladas mas reforçadas com um rebite. Um destes modelos é reforçado com um rebite de cabeça escareada em material compósito enquanto o outro é reforçado com um rebite de cabeça escareada em titânio. Em relação aos dois modelos com junta apenas colada, um deles possui o furo respetivo à forma dos rebites considerados. Nesta categoria é introduzida a simulação de dano progressivo do adesivo através da utilização de um modelo de dano coesivo (CZM).

A comparação entre modelos permitiu investigar a capacidade do rebite em compósito suportar carga à medida que occore dano da ligação adesiva, comparativamente com os modelos de juntas coladas e o de junta colada reforçada com o rebite metálico. Foi realizada uma comparação mais detalhada entre a contribuição do rebite em compósito e do rebite em titânio quando implementados nas respetivas juntas solicitadas ao corte. Os principais objetivos desta primeira categoria passa por estudar a eficiência deste novo protótipo e perceber se esta nova técnica é viável comparativamente com alguns métodos de ligação análogos quando na presença de adesivos danificados.

A segunda categoria de modelos é composta por um grupo de quatro modelos de larga escala baseados na secção da caixa central de uma asa de uma aeronave. Estes modelos possuem uma junta colada e reforçada com rebites entre o revestimento da asa e uma das nervuras da caixa central. Ao longo dessa junta o rebite proposto é distribuído ao longo de 6 posições. Cada um destes modelos possui um nível de dano específico de forma a ser possível a simulação de quatro níveis de dano, alegadamente induzidos por um acontecimento de origem aleatória. Nesta categoria a estrutura dos modelos é sujeita a uma carga típica de arrancamento aplicada no revestimento.

O principal motivo desta segunda categoria baseia-se no estudo da capacidade do rebite em compósito reduzir os níveis de tensão das zonas circundantes quando introduzido numa secção danificada da asa. Se porventura, alguma eventualidade danificar a qualidade da ligação adesiva, o conhecimento da redistribuição de tensões ao longo da superfície dos rebites permite obter uma importante base no entendimento da capacidade que estes elementos de ligação apresentam para suportar as consequências estruturais da rotura do adesivo. Também as distribuições de tensão no filme de adesivo foram alvo de avaliação, sendo finalmente correlacionadas com o papel desempenhado pelos rebites em compósito.

Acknowledgements

First of all, I would like to acknowledge my both supervisors, Prof. Dr. Shijun Guo from SATM of Cranfield University and Prof. Dr. António Torres Marques from FEUP for their constant support, useful discussions and continuous availability.

To Marco Parente, scientific researcher at INEGI, for all the advices, patience and shared knowledge about FEA and *Abaqus®*.

To all the people I met and worked during this whole journey and, directly or indirectly, have contributed to my success. I address a special word of thanks to my friends Marco Alves and Álvaro Oliveira for their friendship and for all our pleasant moments during the last 5 years.

To Bruno and Sofia Leite, for their kindness and hospitality when I went to Zürich. They have been extremely nice and provided me a delightful experience.

To my family, for make this adventure possible. Their love and continuous encouragement were the biggest motivation to push me forward everyday. A special thanks to my brothers for their patience and friendship and to my parents for the efforts they still make to offer me as much as I need, whenever I ask.

Finally, to my girlfriend Mariana Marques for all the love, care, emotional support and for believe in my abilities whatever the situation I was in. She was there for me every time I needed and that is priceless. I am thankful for her truly and integrally honest proof of love.

Contents

List of Figures

List of Tables

List of Acronyms

CRM Composite Rivet Model.

CTE Coefficient of Thermal Expansion.

CZM Cohesive Zone Modelling.

DCB Double Cantilever Beam.

DLJ Double Lap Joint.

ENF End Notch Flexure.

FEA Finite Element Analysis.

FEM Finite Element Method.

FRP Fibre Reinforced Plastics.

GUI Graphics User Interface.

NDT Non-Destructive Technique.

PR Pop Riveted.

SPR Self Piercing Riveted.

TRM Titanium Rivet Model.

VCCT Virtual Crack Closure Technique.

WBDM Wing Box Damaged Model.

WBM Wing Box Model.

Chapter 1

Introduction

Nowadays the permanent evolution of aeronautical and aerospace industries demands for more reliable, strength and lighter solutions. Therefore, current engineers are responsible to provide the answers for all the related specifications, having always in mind the constraints imposed as geometry, budget or manufacturing features.

Composite materials are widely used on aircrafts fuselages, in some cases among many different types of metals. The lightweight allied to high stiffness, good fatigue properties and corrosion resistance of this type of materials allows a reliable life of the structure with less fuel consumption, which reduce costs and levels of pollution. Composites are common used on heavily loaded primary structures of the aircraft as the centre wing box or the vertical tail , for example. Figure 1.1 illustrates the major components made of composites on Airbus A380.

An important question related to the use of these materials remains on the way they are joined together, either in a skin splice joint on the fuselage or between a rib and a spar inside a wing box. Most of the joints on aeronautical and aerospace industry still use mechanical metallic fasteners, mostly made of titanium.

Mechanical fastening is widely used to join aircraft structures, but there are some difficulties associated. When a hole is drilled on a plate the stress field is disturbed

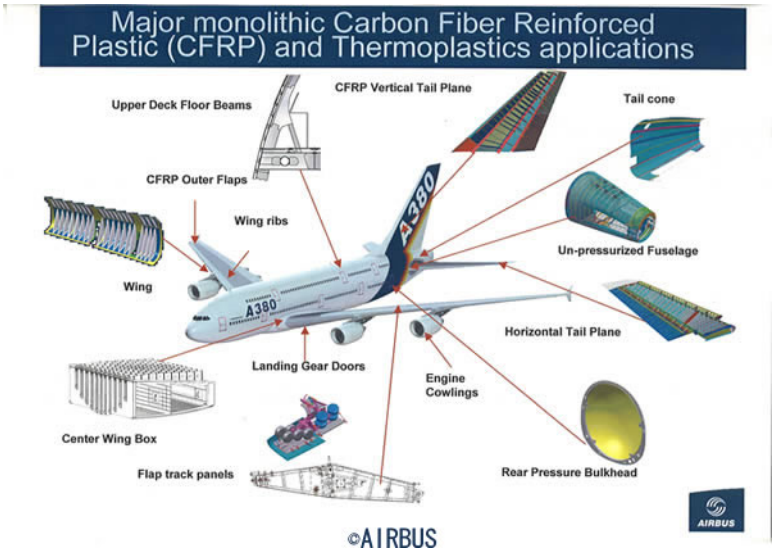

Figure 1.1: Major composite parts of Airbus A380; [1]

producing stress concentrations on the vicinity of the hole. If the hole is filled with a bolt or a rivet those stress concentrations become bigger. Besides the stress gradients, if the plate is made of composite, the drilling operation causes damage of the fibres which induce the weakening of the structure. For that reason, bolted joints deserves a special overlooking when designed because could be acting like weak spots on a structure, even more if made of composites materials. [1]

Adhesively bonded joints have been a solution since many years ago, not only in aircraft structures but also in other industries as the automotive. However, as the lack of reliable, feasible and economical non-destructive inspection methods for this technology has been a constant issue, the use of adhesively bonded joints is still away from the ideal numbers. [2] This method ensures a more uniform stress distribution comparatively to bolting or riveting if the joint is properly designed. However it presents high stress concentrations at the ends of the overlap region which is undesirable when using composite joints, since the weakest strength direction of a composite is on the out-of-plane direction. Nevertheless, there are some techniques to avoid those stress concentrations. [3]

Another option largely used on aerospace field is the hybrid-joint where an adhesive joint is combined with a fastener to provide not only the adhesive properties, but also the attributes of the fastening. This technique could be interpreted as an insurance of the joint integrity with the fastener even if the adhesive bond is overwhelmed. Regarding this technique, an interesting solution to join composite parts arises if the fastener material is made from the same material than the parts to be joined. When composite parts have to be joined, the application of a composite fastener could bring some advantages comparatively to the traditional hybrid-joint technique with metallic fastener.

The understanding of the stress distribution within the rivet as a monitoring system for aircraft structures could be an interesting point of view for this solution. The development of this fastener could provide a new approach on the real time stress redistribution when any kind of damage initiates on the component. With this fastener a monitoring system could be inserted within it and the register of real time stress gradients becomes possible. Hence, although a composite fastener could mean leverage on performance and on weight savings comparatively to the metallic solutions, the monitored behaviour field and the real-time stress surveillance could start a new way to interact with aircraft structures and increase the efficiency to solve damage problems.

The joint design on an aerospace structure is still considered one of the main concerns on project design as Hart-Smith claims: "The most appropriate way to design aerospace structures is to design the joints first and to fill in the gaps in between afterwards." [4]

Thesis Framework

The research presented along this thesis was developed on School of Aerospace, Transport and Manufacturing (SATM) from Cranfield University located at United Kingdom under the supervision of Dr. Shijun Guo. Dr. Guo is the course director of the Aerospace Vehicle Design (AVD) at SATM and a Reader specialised in the subject of Aeroelasticity and Composite Structures. This visiting research was possible due to an Erasmus+

Placements mobility program of 5 months based on a partnership of both universities.

The guidance on Faculdade de Engenharia da Universidade do Porto was carried out by Dr. António Torres Marques, Professor at FEUP while some advices, tips and enriching discussions about FEA were performed with the researcher Marco Parente from FEUP/INEGI.

Thesis Objectives

The aim of this research is to study, through Finite Element Analysis, a new design of a composite fastener for composite joint reinforcement. It is important to understand the behaviour of a composite fastener on a bonded-bolted joint when the adhesive is subjected to damage. On that case the author pretends to know if this component could be a viable solution to carry stresses after adhesive damage or even after adhesive failure.

The comparison between this new design and a common titanium rivet on the same conditions is one of the main focus to infer if this solution allows a positive reinforcement over the bonded joint and what is the level comparatively to the existing techniques.

Another objective is based on understanding the role of a set of composite rivets applied to a damaged bonded joint on a wing box structure. On that case it is necessary to understand if those new fasteners have the ability to hold on the failure of the wing in case of adhesive damage caused by a random event.

Summing up, the primary objective behind this work is to understand if the purposed composite fastener has the overall ability to replace the existing techniques on aircrafts bonded-bolted joints, even if it is only for joint repair.

Thesis Layout

The thesis is firstly divided into two main parts. Part 1 collects the literature review performed about the different subjects addressed on this research while part 2 refers to the numerical study with the subsequent discussion and results interpretation.

Chapter 2 introduces the main components of a common wing box structure and their respective functionality. Also concepts as wing air loads are briefly explained to help to understand some modelling features adopted further away on chapter 7.

Chapter 3 has a collection of mechanical fastening features from unthreaded fasteners (rivets). Some investigations performed with metallic fastened joints are referred on this chapter in order to understand their applicability, their pros and cons and their considerations.

The author had a special care with chapters 4, 5 and 6 in order to study only joints made of composite materials. Some exceptions may occur but the special purpose of those chapters was to analyse specifically composite joints.

On chapter 4 the state of art of composite fastened joints is described. Composite fastened joins means any joint fastened with rivets, bolts, pins or any similar metallic object. Several considerations, design rules and respective terminology are indicated. Also the failure modes of this type of joints are introduced.

Chapter 5 introduces the state of art of adhesively bonded composite joints. The chapter is mainly dedicated to composite bonded joints. Several design considerations, parameters that influence joint strength and fatigue life are discussed. Also failure modes, strength prediction and damage modelling are other subjects of interest addressed on this

chapter.

With chapter 6 the state of art of bonded-bolted composite joints is described. The works reviewed admit rivets, bolt and pins as fasteners. Also a wide variety of adhesives is found. Many parameters that influences the performance of bonded-bolted composite joints is discussed.

Chapter 7 includes the detailed description of the creation of all numerical models. This chapter includes the first stage of validation, the development of the first category of models (Single Lap Joint Models) and the second category of models (Wing Box Section Models).

Chapter 8 involves the results of interest for this research divided through two categories of models. Results discussion is performed along the chapter and conclusions are draw at the end of each category.

Part I

LITERATURE REVIEW

Chapter 2

Aircraft Wing Structures

Wings on an aircraft are airfoils that when moved very fast through the air, creates a flow that generates lift. The principle of aircraft flying is based on this assumption: considering all the loads acting on the structure, when the aircraft is intending to take-off, the resultant force should be created by the lift. Wings could be made of various shapes and sizes according the required characteristics for each flight. The main structures of a wing are the spars, the ribs, the stringers and the skins. They are illustrated on Figure 2.1. Air loads act directly on the wing skins and are transmitted to the ribs. Then, the ribs divide the load through their webs and transfer it by shear to the stringers and spars.

Wings can be attached to the aircraft through three points, at the top of the fuselage, at the middle of the fuselage and at the bottom of the fuselage as seen on Figure 2.2. The extension of the wings can also be aligned with the perpendicular plane of the middle fuselage or can have a slightly inclination. This angular displacement is known as the wing dihedral and its also briefly introduced on Figure 2.2.

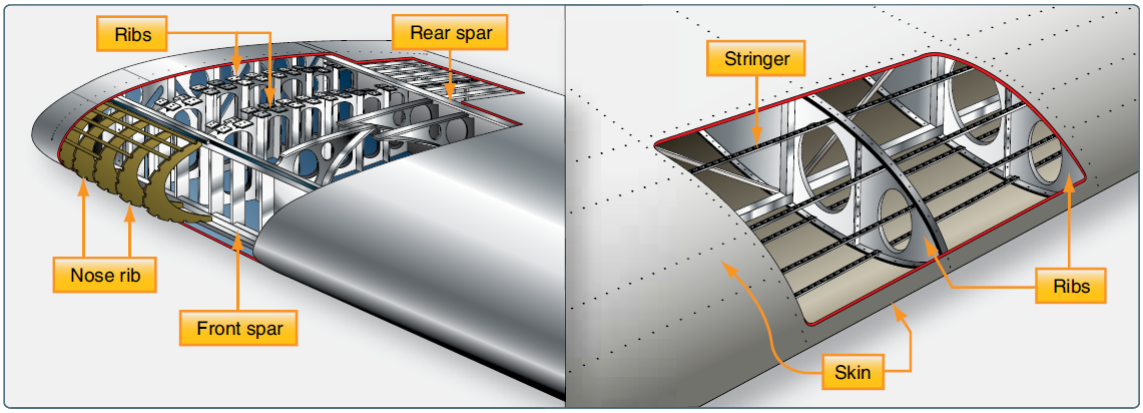

Figure 2.1: Wing structure nomenclature; [5]

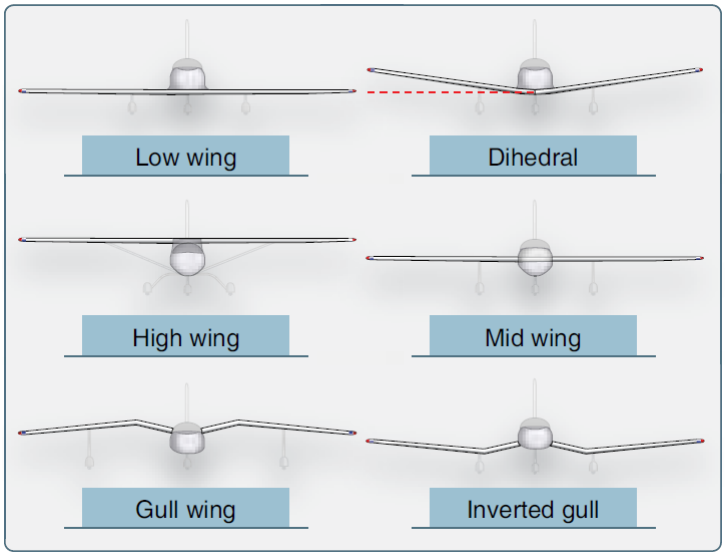

Figure 2.2: Attaching points of wings and the dihedral angle definition; [5]

2.1 Spars

The spars are the principle structural members of a wing and running spanwise, on the same direction of the stringers. This direction is parallel to the lateral axis of the aircraft, from the wing root towards the wing tip. There are 3 types of possible spar constructions

on a wing, as:

- Monospar;
- Multispar;
- Box Beam Type.

For the first one only one spar is used, however this configuration is not so common. For the second one, the wing has several longitudinal components along the spanwise direction. But the box beam type is often used by air transport category aircraft because of space requirements for the housing of fuel tanks and landing gears. It consists on two main spars, front and rear, with connecting bulkheads and ribs running chordwise to provide additional strength. The front spar is usually placed at 15 % of the chordwise and the rear spar at 55 % to 60 % of the chordwise to ensure enough space for control systems elements.[6]

These components could be made of various shapes and materials according the purpose of each vehicle (Figure 2.3). The I-beam shape could be divided into two pieces, the top and bottom regions named ”caps” which provide a foundation for the skin attachment and the ”web” which is the vertical section connecting the top and bottom caps. The spars could be extruded into a single piece or obtained by multiple extrusions and mechanical fastening. A fail-safe spar is usually made by a riveted spar web with a splice joint and a upper spar cap riveted as well to the upper spar web. This part is presented on Figure 2.4 and is often used since if one of the spar sections fail the remaining one is able to carry the load.

They support all the distributed loads and concentrated weights (as the fuselage, landing gears and engines) and take an important role on carrying wing bending moments. When all the other structural members of the wing are under load, the resultant stresses are transferred to the spars and for that reason these components are of crucial importance on wing structure.

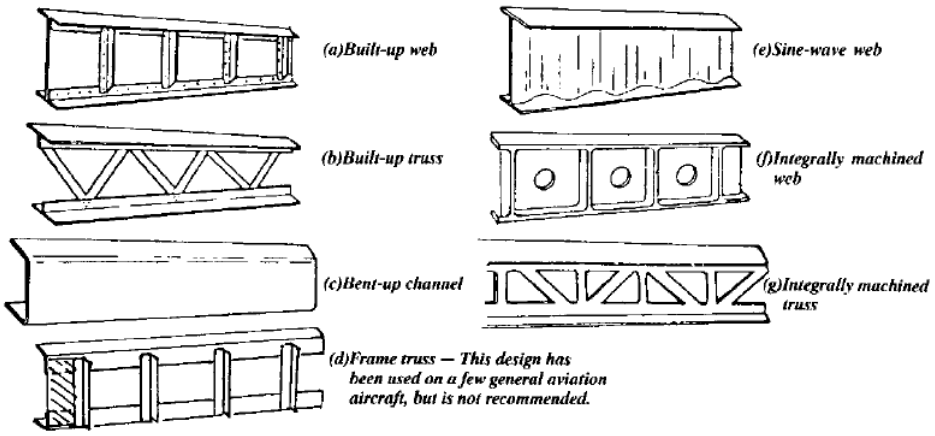

Figure 2.3: Typical spar configurations; [5]

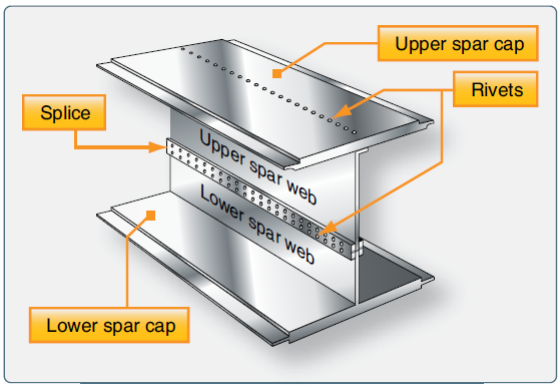

Figure 2.4: Example of fail-safe spar; [5]

2.2 Ribs

Ribs are the structural components that extend from the leading edge to the trailing edge of the wing and along with the stringers and the spars make up the framework of the wing. Usually, are constructed as solid webs although webs with lightening holes or trusses could also be found. Sometimes the lightening holes are used for access by the aircraft operators since the size of the hole is large enough to allow them to pass through

those holes.

Ribs transmit the primary loads from wing skins and stringers to the spars and ensure the contour shape of the cover panel acting as a compressive load carrier. These structural members are also provided for flap, aileron, pylon, nacelle and landing gear support. Inertia loads as fuel, structure or equipments could also be carried by them. Ribs are also composed by caps, stiffeners and webs as the spars components. A wing rib could have a specific name according to its function or position on a wing. For example, there are nose ribs, false ribs, butt ribs and a lot of other specific functional ribs. Some of them are presented on wing structure of Figure 2.5.[6]

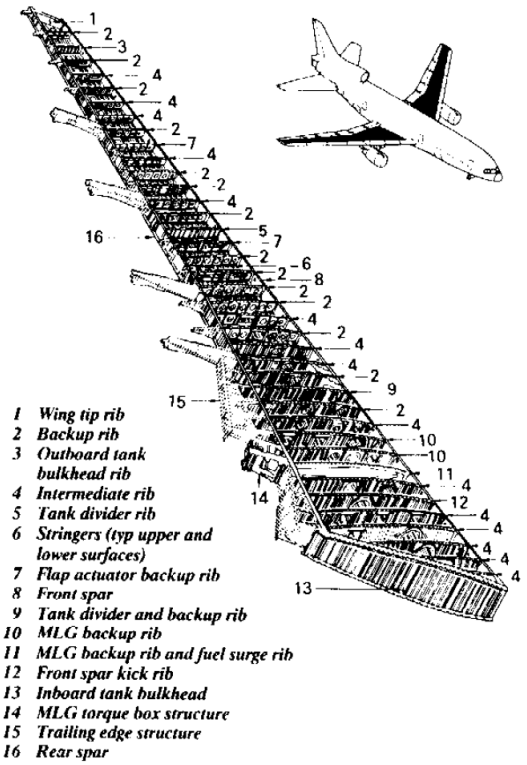

Figure 2.5: Typical ribs functions and locations for a two spar wing configuration; [6]

The ribs spacing is an important question when designing a wing box section because it could represent an high amount of total box weight. Choosing an higher rib spacing

could lead to saving costs and less fatigue hazards. [6]

As illustrated on Figure 2.6 the cover panel weight increases with the rib spacing since an higher stiffness is needed to counterbalance it. It is important to note that an optimum wing would have a variable rib spacing with the maximum spacing at the inboard end. [6]

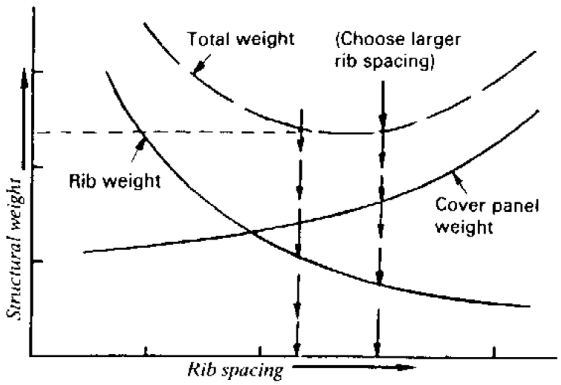

Figure 2.6: Determination of wing rib spacing by structural weight comparison; [6]

2.3 Skins

Frequently, the wing skins of an aircraft have full cantilever beam design (Figure 2.7 on the left). This means that no external bracing is needed through struts or jury struts. Figure 2.7 on the right presents an example of externally braced wings by struts. The absence of external bracing means that the skins of the wing would share some of the carried ground and flight loads. The aim for sharing load between wing spars, wing ribs and wing skins leads to the development of a wing stressed-skin design, visible on Figure 2.8 a). On this case, the skin is stiffened to aid with this function. [5]

Usually, commercial aircraft with stressed-skins carry the fuel inside the wing boxes (the military fighter aircraft usually store it in the fuselage or on external tanks). This is known as wet wing design and is illustrated on Figure 2.8 b). For this, the joints within the wings are made of special leak-proof, sealing and fuel resistance compounds even as

the chemical inert materials of the structural components. [6] [5]

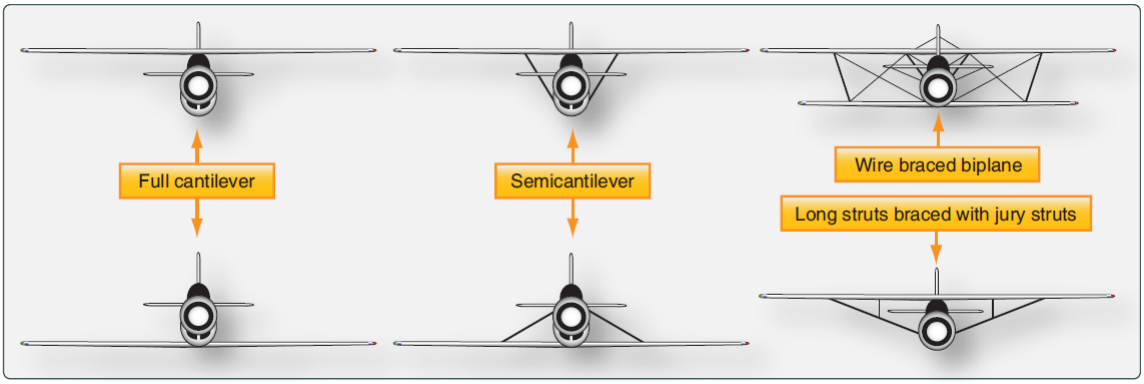

Figure 2.7: Wing configuration of full cantilever, semi-cantilever and external braced wing with struts and vertical jury struts; [5]

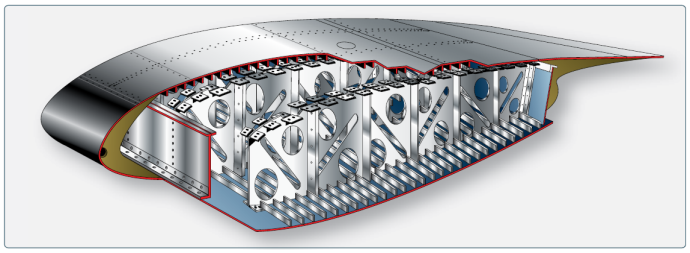

(a) Wing stressed-skin design

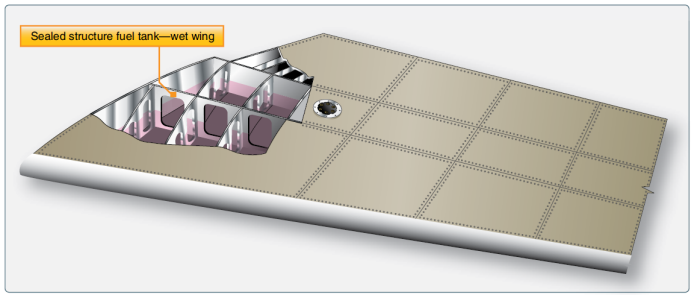

(b) Wet wing design

Figure 2.8: Stressed-skin for carrying part of the stresses and the configuration of a wing for carrying fuel; [5]

The correct fuel management through a certain fuel tank geometry inside a wing is

responsible for a lighter weight structure and lead to an optimisation of the structural loads. As illustrated on Figure 2.9, for three fuel tank geometries the bending moment relief on the wing root is different. On that case, the engineer should look for a geometry which relieves the highest bending moment since it aids on the structure balance. The tanks are fed from the inboard tank to the outboard tank, from the wing root towards the wing tip for a correct increase of bending moment. The case C with three tanks reveals a better performance on the bending moment relief and it is advantageous to use this solution, although sometimes the implementation of the recommended solutions is not possible. [6]

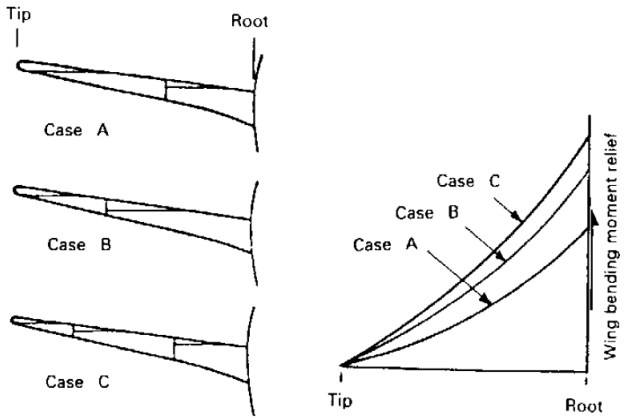

Figure 2.9: Fuel tank geometry and its effect on the wing bending moment relief; [6]

2.4 Wing Air Load

The air loading on a wing could be divided into two subcategories: additional loading or basic loading. Additional air loading is strongly dependent by the angle of attack of a wing (α on Figure 2.10) whereas the basic loading is the set of loads applied to the wing when the total lift is zero. This type of loading is caused by wing twist. The twist of a wing would generate a dissimilar lift coefficient distributions along the spanwise direction

since the angle of incidence also vary along it. [6] This section only has an approach to additional loading.

The shape of the most common aircraft wings are based on aerofoils, streamlined bodies designed to produce lift. Some specific terms should be used when discussing topics about aerofoil's theory and that terminology is briefly introduced on Figure 2.10. [7]

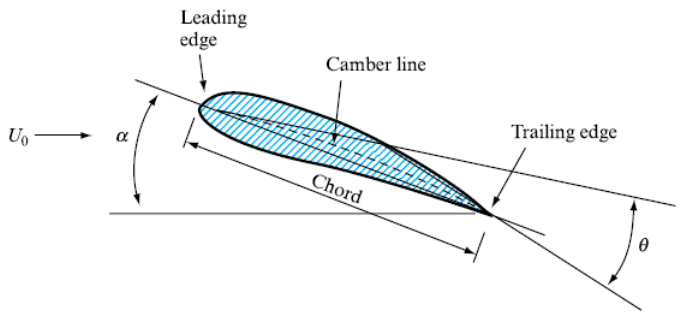

Figure 2.10: Aerofoil shape and characteristic terms; [7]

The angle α and θ are the angle of attack of the aerofoil and the angle of deviation, respectively. The angle of attack is measured between the direction of the stream motion and the chord line whereas the deviation is measured between the tangent to the camber line at the leading edge and the tangent to the camber line at the trailing edge. The camber line is represented by a straight line joining the centres of curvature of the leading and trailing edges. [7]

The main purpose of an aerofoil is to produce lift. However, during this lift generation some drag is also initiated at the same time.

$$Lift = \frac{1}{2}\,\rho\, C_L\, U_0^2\, A \quad [7] \tag{2.1}$$

$$Drag = \frac{1}{2}\,\rho\,C_D\,U_0^2\,A \quad [7] \tag{2.2}$$

$$\frac{Lift}{Drag} = \frac{C_L}{C_D} \quad [7] \tag{2.3}$$

The usefulness of a wing is measured by the lift to drag ratio ($\frac{C_L}{C_D}$). The higher the ratio is, the better the aerofoil. The aim of these structures is to produce the maximum lift with the lowest drag penalty. [7]

For the common wings , with aspect ratio > 3, the lift generation varies directly with the angle of attack. [6] Thus, for an air stream flowing through an aerofoil with some inclination it will split the flow into two streams, one located over the lower side of the wing and one over the upper side of the wing. Both flows are subjected to different aerofoil contours and therefore the two flows will have unequal velocities. When both streams meet at the trailing edge, the difference in velocity caused by the inclination of the aerofoil forms a starting vortex. If the velocity on the top surface of the aerofoil is higher than the velocity on the bottom surface and according Bernoulli's equation,

$$p + \frac{1}{2}\,\rho\,V^2 + \gamma z = constant \quad [8] \tag{2.4}$$

where p, $\frac{1}{2}\,\rho V^2$ and γz are the static pressure, the dynamic pressure and the potential pressure [8], respectively, such velocity distributions will provoke lower pressures on the top surface and higher pressures on the bottom surface of the wing. Those pressure distributions along the wing (Figure 2.11) would create a resultant force, namely the lift which pushes the aircraft upwards. Therefore, a positive inclination of a wing generates such a resulting pressure distribution that gives rise to lift.

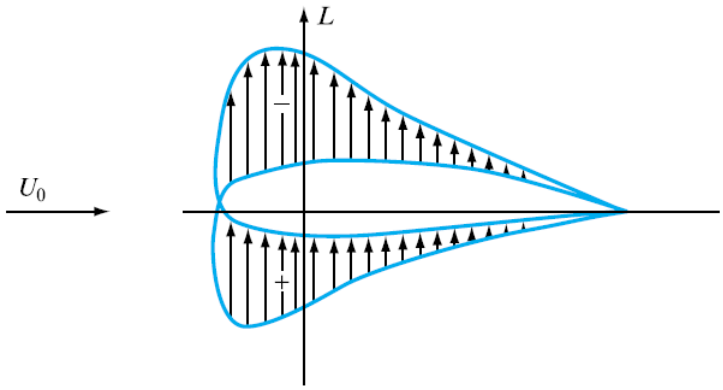

Figure 2.11: Pressure distribution around an aerofoil; [7]

As the angle of attack is increasing, the lift coefficient is also rising whereas the drag coefficient remains at low levels. During this evolution the point of separation of the boundary layer on the aerofoils top surface is being moved forward according the scheme on Figure 2.12 b). The separation point will move until a point called stall point, where an increase on the angle of attack will not generate any increase on lift. At this critical angle of incidence, the aircraft suddenly loses lift and an high amount of drag is rapidly generated. The plot illustrated on Figure 2.12 a) shows the calculated and experimental lift and drag coefficient distributions in function of the angle of attack (α). A reference to the stall region is also made.

It is important to note that the concepts discussed before are related to flow past infinitely long aerofoils, where the variation of the flow patterns could be neglected on the spanwise direction. Actually, the best approximation for real life experiments is performed with a three-dimensional flow, where the aerofoil is more similar to a real aircraft wing. In that case, the span has a finite length and its denoted by b. The lift distribution on this case is considerably modified because the tips of the wings extend into the surrounding fluid.

When a wing is subjected to lift, the pressure on the lower side is higher than the

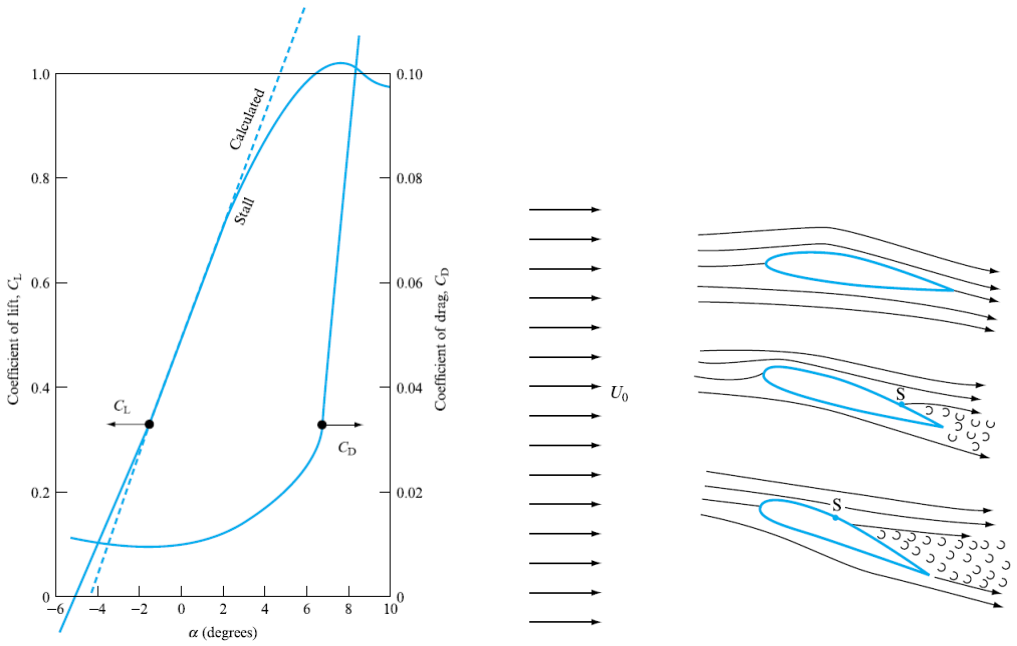

(a) Lift and drag coefficients

(b) Separation point

Figure 2.12: Calculated and experimental lift and drag coefficients distribution in function of angle of incidence and the evolution of the boundary layer separation point due to the increased angle of incidence; [7]

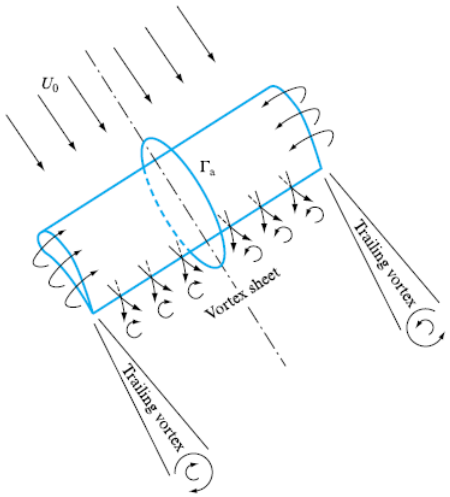

Figure 2.13: Three-dimensional flow effects on a finite span aerofoil; [7]

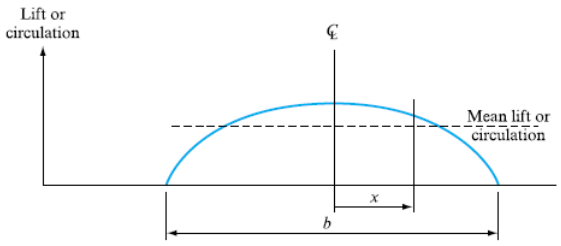

Figure 2.14: Lift distribution along a finite span aerofoil; [7]

pressure on the upper side and hence, for a finite span aerofoil (wing) the flow moves from the lower side to the upper side through the ends of the wing as presented on Figure 2.13. The lower stream is deflected from the centre towards the wing tip whereas the upper flow is deflected from the wing tip towards the centre. This opposite motion produces some vortex sheet along the span of the wing that develops to trailing vortex at the trailing edges. [7]

The resultant pressure distributions will be maximum at the middle section of the wing and decreases until zero towards the tip. As the resultant pressure distribution has direct effect on the lift distribution, the trend for the lift will be also affected. For that case, the lift distribution would have the distribution illustrated on Figure 2.14.

Chapter 3

Mechanical Fastening

One of the most used techniques to join aircraft fuselage skins and the supporting structures beneath them is mechanical fastening. It could be mainly divided through riveting and bolting. Bolted joints are not so common on airframes as riveted joints because the manufacturing of threaded fasteners is more expensive than clearance fasteners. The clinching of rivets could be performed very quickly with automatic machinery which reduces labour time. Some rivets provide also better aerodynamic properties (as flush-head rivets) and less weight than the equivalent bolt. Some advantages of rivets comparatively to other mechanical fasteners include [9]:

- Low fabrication cost;
- Low installation cost;
- Ability to produce semi-permanent joints that can be readily inspected upon installation;
- Ability to allow relative rotation between parts (acting as pivot shafts);
- Ability to join dissimilar materials;
- Attractive appearance (they can be made flush and virtually invisible);

- Ability to provide an aerodynamically smooth contour when countersinking and shaving techniques are used;
- Wide variety of materials, shapes and sizes;
- Wide variety of tools and equipments for installation.

Nevertheless, there are some disadvantages regarding the use of rivets comparatively to the other mechanical fasteners, namely bolts, like [6], [9] :

- Lower tensile and fatigue strength;
- High enough tensile forces can pull out the rivet from the joint;
- Sever vibration can loosen the joint and retightening can be difficult;
- Impossibility of disassembly for maintenance or repair;
- Lower dimensional precision due to high volume production.

The most common materials for aircraft fasteners include aluminium alloys, titanium and nickel-based alloys. Some special purpose ones could be made of mild steel, monel and cooper. [10] [11]

Along this chapter only the subject of riveting will be addressed since the specific characterization of bolting features is out of the scope of this investigation.

3.1 Solid Rivets

These rivets are used when the access of both sides of the assembly structure is available. Indeed, they are mainly used on longitudinal fuselage joints due to the higher strength comparatively to blind rivets. Solid rivets are not indicated for tensile applications nor for joining thick sheets since the tensile strength is lower comparatively to

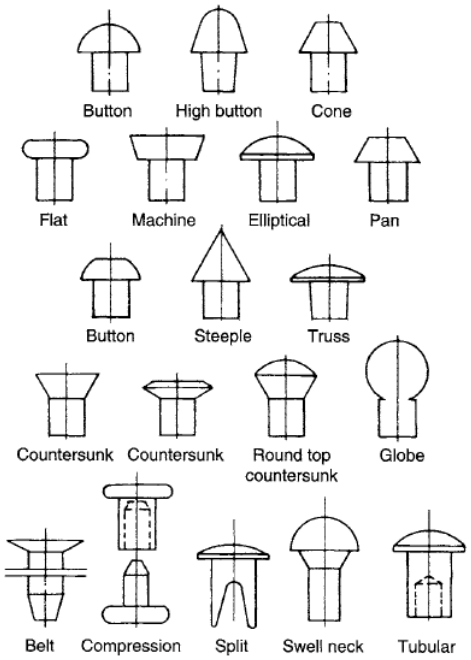

Figure 3.1: Schematic illustration of some types of solid rivets; [9]

shear strength and as the grip thickness increases (grip is the thickness of both sheets to join) the lock of the rivet turns more difficult. [5] They are composed by only one piece and can have flush or protruding heads. Those head types are the most used on aircraft structures. Flush-head rivets can also be called as countersunk rivets. [10]

A wide variety of rivet shapes could be found according to specific applications or industries. Some of them are illustrated on Figure 3.1. However, the most common rivets used on airframe structures are presented on Figure 3.2. Countersunk rivets are used for high aerodynamic efficiency applications as the longitudinal lap joints along the fuselage. The brazier head rivet is commonly used on external surfaces of non-combat aircrafts while the round head and flat head rivets are used on internal structures. The universal head rivet was developed exclusively to aircraft industry in order to replace both round and brazier rivets. [5]

Solid rivets are classified according to the head shape, the manufacturing material

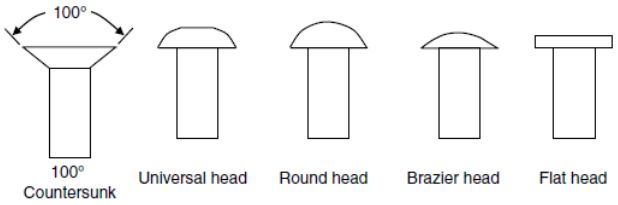

Figure 3.2: Common types of aircraft solid rivets; [10]

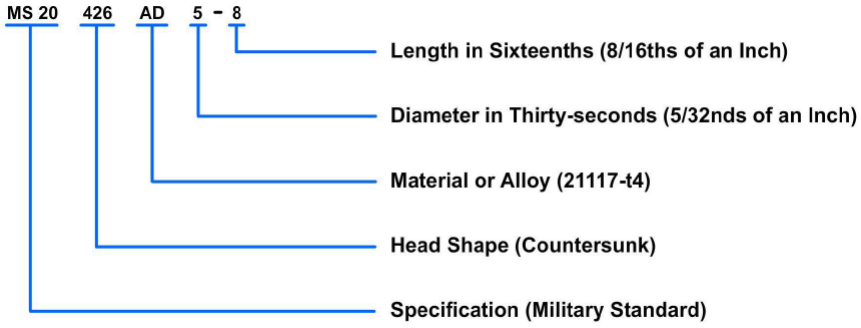

Figure 3.3: Rivet designation system; [5]

and by their size. There is a specific nomenclature system for rivets designation. That identification is properly sub-coded according to the following categories:

- Standard specification;
- Head Shape;
- Material or Alloy;
- Shank diameter (in thirty seconds - 1/32nds of an Inch);
- Rivet Length (in sixteenths - 1/16ths of an Inch).

An example of a full rivet code is showed on Figure 3.3. The first letters of the designation refers to the used standard and the most common used are the MS20 (Military

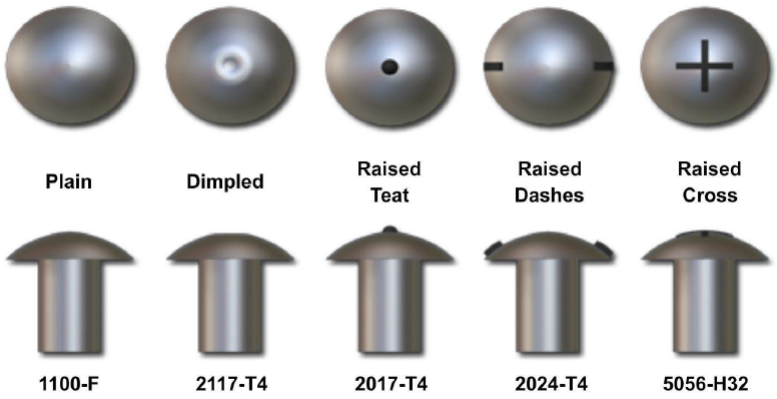

Figure 3.4: Rivet head marks and the respective aluminium alloys; [11]

Material	Aluminium		Aluminium alloy	
	1100-F	2117-T4	2017-T4	2024-T4	5056-H32
Material code	A	AD	D	DD	B
Markings	Plain	Dimple	Raised dot	Raised double dash	Raised cross

Figure 3.5: Rivet head marks, aluminium alloys and their respective letter code; [10]

Standard specification), AN (Air Force/ Navy Standards specification) and NAS (National Aerospace Standard specification). The following numbers refer to the head style. The head style is usually based on the options from Figure 3.2.

Aluminium alloys are considered the standard material for rivets manufacturing and a standard identification code exists for classifying them according to the aluminium alloy. These identification code is assured by markings on rivet heads. Therefore, each mark corresponds to a specific aluminium alloy and these combination would have a letter code. Figure 3.4 and 3.5 illustrate the rivet head marks and the associated code numbers.

Finally, the last two numbers of the code spaced by a dash are correspondent to the shank diameter and rivet length measured according to some parcelling of imperial units.

3.1.1 Installation

Before the installation, a rivet corresponds to a smooth cylindrical shank with a manufacture head on one end. The other end of the shank is called bucktail [5] or tail [12] and is the region of the rivet that will suffer deformation to originate the driven-head.

The hole is drilled on the sheets just with a small gap relatively to the rivet diameter to ensure the correct fit of the rivet after deformation. Using a manual hammer, a pneumatically, hydraulically or electromagnetically driven squeezing tool the driven-head is shaped while the manufactured or original head is supported by an anvil [13] or bucking bar. That procedure expands the shank of the rivet and ensures a perfect locking of the rivet, achieving fastening. [5] Figure 3.6 illustrates schematically the installation of a solid rivet.

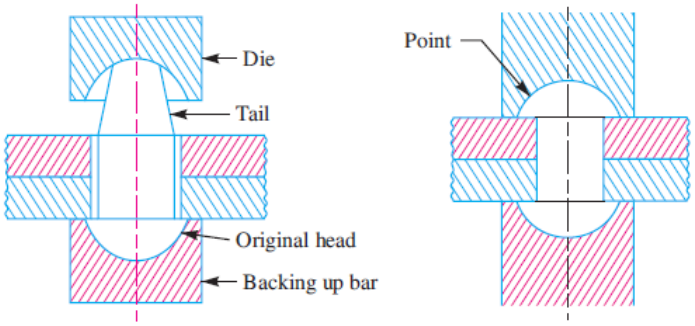

(a) Initial position (b) Final position

Figure 3.6: Riveting process; [12]

For countersink procedure, the drilling of the hole is only performed when the sheet thickness > 1 mm. Otherwise, if the sheet thickness is $\leqslant 1$ mm the countersink is obtained according to a plastically formation known as dimpling. Dimpling is better than drilling on this cases since the walls of the hole will be very small, inducting an abnormal bearing pressure leading to a significant decrease on joint strength. [13] Figure 3.7 shows the aspect of a dimpled countersunk rivet joint. With this type of joint the load transfer

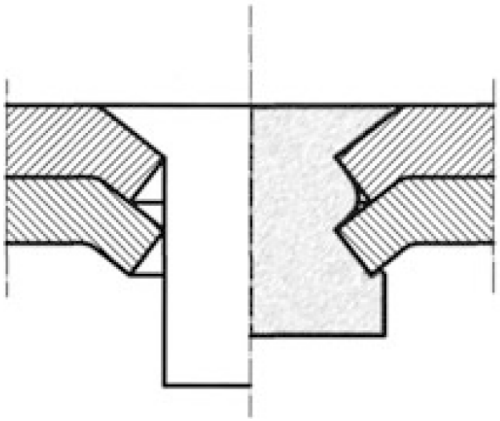

Figure 3.7: Dimpled countersink. Left - before installation; Right - after installation; Adapted from [13]

is more pronounced along the dimple tabs than through the rivets. The cost of using countersunk rivets can increase comparatively to the use of protruding head rivets due in part to the costs of dimpling operations.

The incorrect design of countersunk riveted joints with sheet thickness > 1 mm could lead to an undesirable phenomena known as knife edge effect. This event occurs when the head depth of the rivet is coincident with the thickness of the countersunk sheet, $h = t$, schematically illustrated on Figure 3.8. According to that, Niu [6] postulates that the thickness (t) of the countersunk sheet should be at least 1.5 times the depth (h) of the rivet head. Also Fokker Aerostructures suggests a design rule and requires $(h - t) \geqslant 0.2mm$. [13]

The stress concentration around the countersunk hole and the fatigue life are extremely important subjects when designing a riveted joint. On this case, avoiding the knife edge effect, as it was discussed before, is advantageous to ensure a good fatigue life. As the thickness of the plate increases comparatively to the head depth of the countersunk rivet, the stress concentration around the hole decreases abruptly for t/h ratios close to 1, which corroborate the design rule to eliminate the knife edge effect. Figure 3.9 a) shows this K_t

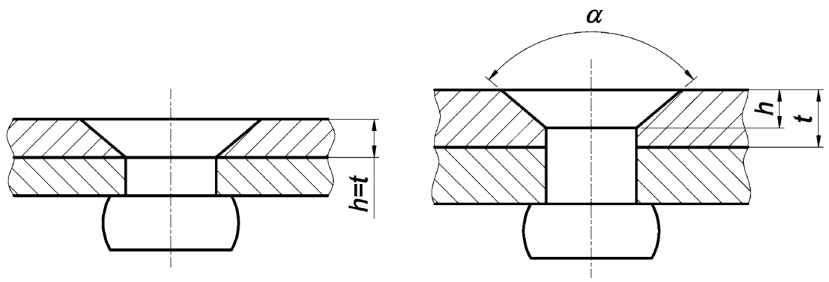

(a) Knife edge effect (b) Recommended geometry

Figure 3.8: Countersunk design; [13]

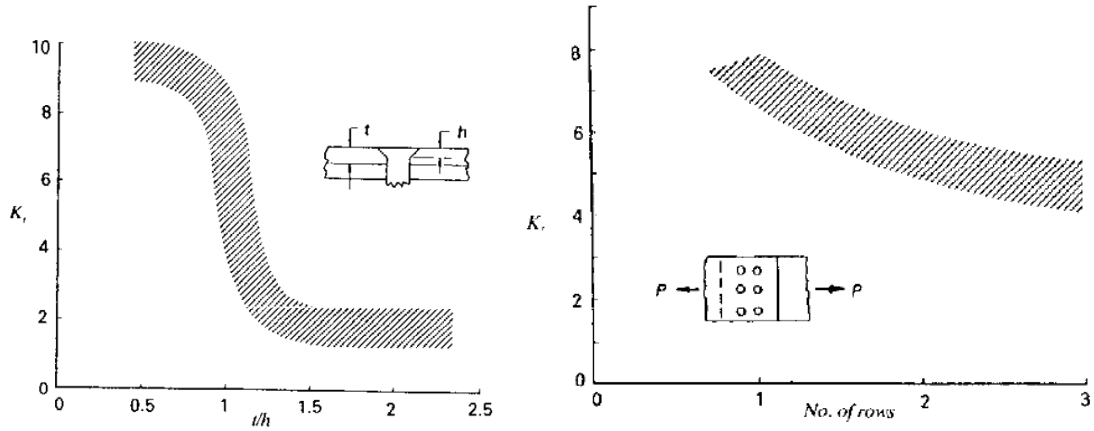

(a) t/h (b) Rows of fasteners

Figure 3.9: Stress concentration factor in function of: a) t/h ratio; b) number of rows of fasteners; [6]

reduction in function of t/h ratios.

The increase of rows of fasteners along aircraft splice joints also promotes the reduction of stress concentration factor around the holes. That is why most of the airframe joints are composed by two or more rows of fasteners. This behaviour is illustrated on Figure 3.9 b).

3.2 Blind Rivets

These rivets can be considered special purpose fasteners and are installed when the access from both side of the structure assembly is not possible or impractical. [13] It is important to note that this type of rivets does not provide the same strength as a solid rivet. They are a two-part fastener usually composed by a shell or sleeve and a stem. The stem is placed within the shell and has a significant height to allow its pulling. [14] One sample of this type of rivets is presented on Figure 3.10 a)

Those type of rivets are not used in longitudinal fuselage connections nor on structural parts. They may also be used to join non-structural parts of an aircraft or connect them to the airframe.

The common materials for this type of rivets are identical to the ones used with solid rivets. Usually, the materials of the shell are aluminium alloys, steel, stainless steel and nickel-cooper alloys while for the stem, which induces the shell deformation, the strength of its material should be at least equivalent to the material of the shell. [14]

Moroni and Pirondi [15] investigated two sub-categories of joints named PR and SPR with the aid of adhesive bonding. Those acronyms mean Pop Riveted and Self Piecing Riveted joint, respectively. Both techniques are applied to join sheets of galvanized steel and aluminium recurring to an aluminium rivet. PR is a fastening method that allows any kind of joining since it only involves the plastic deformation of the rivet. This method can be done with access by only one side of the joint, which means that the rivet used on this technique is a common blind rivet. The SPR is a technique similar to clinching and produces plastic deformation either of the rivet and of the adherends. Figure 3.11 illustrates the fracture area of both types of joints. On the right it is possible to confirm the plastic deformation of the adherends caused by the clinching of self pierced rivets.

This investigation was done recurring to bonded-riveted joints for both techniques and compared to single-riveted joints and single-bonded joints. Various scales of environmen-

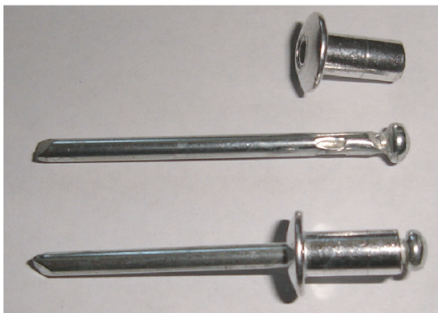

(a) Example of a blind rivet; Adapted from [16]

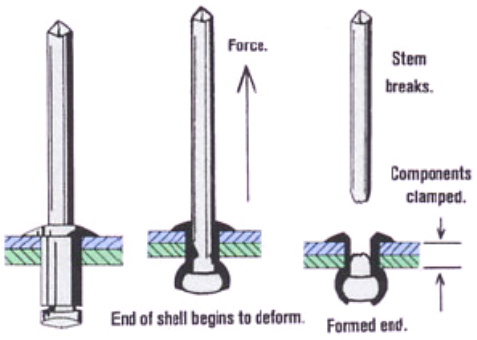

(b) Blind rivet installation; [14]

Figure 3.10: Blind rivet and common installation procedure;

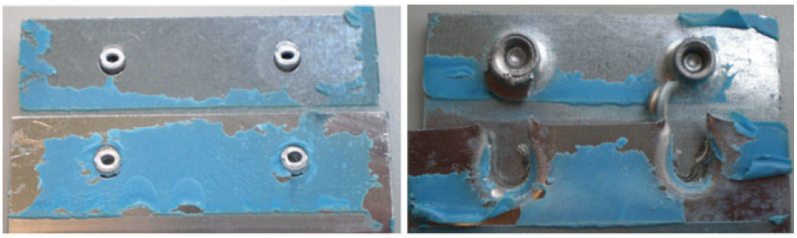

Figure 3.11: Fracture region of PR and SPR joints: Left - PR; Right - SPR; [15]

tal temperatures were tested and some FE models were developed considering a cohesive zone model for the adhesive layer and a ductile damage model for the rivets. The general conclusion is that bonded-riveted joints depend mostly on the strength of adhesive bond and the rivet becomes relevant for carrying stresses when the adhesive performance decreases.

The work performed by Sadowski et al. [16] deals with experimental and numerical investigation of steel double lap joints reinforced by aluminium blind rivets. The problem was also treated for riveted joint, adhesive joint and bonded-riveted joint. The experiments were done recurring to digital image correlation system ARAMIS to perform an exact monitoring of deformation. *Abaqus ®* software was used to produce FE models recurring to a cohesive zone model for the adhesive layer and a material non-linearity for the metallic components.

The general trend of those results shows that the reinforcement of adhesive bonded joints by blind rivets improve the static strength and the stiffness of the joint. The fracture of those joints is divided into two stages and enables the increase of energy absorption up to 35 %. The stiffening induced by the rivets promote durability and reliability of the structural applications where these bonded-riveted joints are employed.

3.2.1 Installation

The installation of a blind rivet just needs the access from one side of the joint, so usually some special tools are used and controlled by manual handling, pneumatics or electricity. After the positioning of the rivet, the stem is pulled out through the normal direction of the plate and the end of the stem forces the shell to deform. That deformation of the shell on the bottom location of the plates ensures the necessary clamping force to stick the plates together. When the desired level of clamping force is achieved the stem breaks and is removed by the operator/equipment. [14] This procedure is presented on Figure 3.10 b). It is important to note that this procedure is valid for a specific method

and specific blind rivet named Cherry rivet. This rivet is one of the most popular since the company Cherry Aerospace was the first entity to introduce this concept on aircraft industry. There are other numerous techniques and types of blind rivets as extensively indicated by Messler [9]. The description of other special purpose fasteners as *Hi-Lock* ®, *Jo-Bolt* ® or *CherryMax* ®, for example, can be found in [5], [6], [11] and [9].

If the load in the stem causes its break before the achievement of the recommended clamping force the integrity of the joint might be compromised. As solid rivets, the grip range of these rivets is a subject of interest because if it is too small, the excess material left on blind side requires more load to break the stem whereas if the grip range is too high, the length of the rivet is not enough to clamp the joint.

Chapter 4

Mechanically Fastened Composite Joints

Composite materials behave on a different manner comparatively to metallic materials due to their anisotropy and inhomogeneity when on service. The loading response is more complex so the strength and failure strength are much more difficult to predict. However, when a structure is designed, the behaviour of these structure under static and dynamic loads should be known, also the fatigue life should be correctly estimated for every kind of possible in-service environments. In order to decrease the possibilities of error and wrong predictions, several investigations, analytical models and finite element analysis have been performed to ensure a correct design of composite joints. Currently, joining techniques and failure prediction of composite materials are subjects under high development by the scientific community. [2]

As it was described before, a wide technique used to join composite materials is adhesive bonding with a mechanical fastener and that type of joining induces stress concentrations and weakness around the hole. These events decrease the strength and fatigue life of composites irreversibly, so an accurate design process should be carried out.

Before catastrophic failure of a composite fastened joint, fatigue damage has a pre-

ponderant role. This event is mainly generated around bolt holes and could be divided into three categories:

- Hole wear;
- Damage in the contact surface;
- Growth of delamination around the bolt holes induced by drilling.

The first one is generated due to the friction forces between the fastener and the hole resulting in erosion of the material. The damage in the contact surface is provoked by bending of the fastener under loading and causes an elongation of the hole. The causes for the last one is very explicit and it decreases the fatigue life of the joint. Upon this damage stage, the composite bolted joint could fail permanently if some grieve conditions are created/maintained.

There are several composite joints failure modes as presented on Figure 4.1. Some of them are known as catastrophic or 'premature' mechanisms and should be strongly avoided since they lead to the instantaneously collapse of the structure.

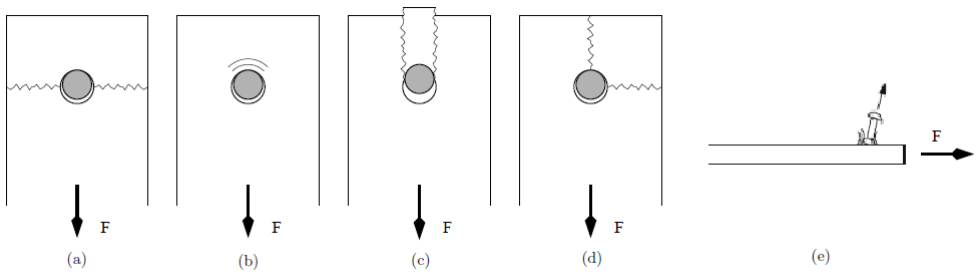

Figure 4.1: Macroscopic failure mechanisms of composites bolted/riveted joints: (a) Net-tension (b) Bearing (c) Shear-out (d) Cleavage (e) Pull-through; Adapted from [1]

According to these types of failure modes, the failure plane representation for each of them is illustrated on Figure 4.2. Each plane shows the contact area along which the frac-

ture propagates. The occurrence of a specific failure mode for a composite fastened joint is highly dependent of geometrical parameters, composite lay-up and stacking sequence.

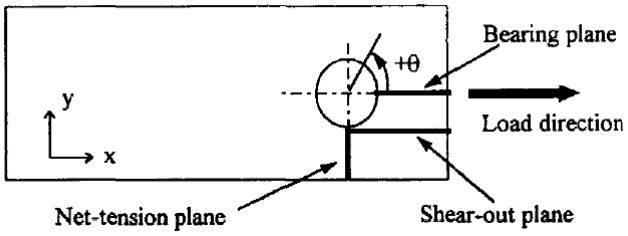

Figure 4.2: Failure planes; [17]

Several authors [18], [19] and [2] have investigated the relationship between the development of a certain failure mode and the following geometrical parameters, illustrated on Figure 4.3:

- Specimen width (w);
- Hole diameter (d);
- Hole-to-edge distance (e);
- Laminate thickness (t);
- Type of fastener [20].

Bearing failure is considered as the intended fracture mode since it holds a higher strength of the joint and the fracture is not too brittle as the other mechanisms. According to Hart-Smith, this failure mode occurs when the bolt diameter is a small fraction of the plate width and usually it tends to produce an elongation of the hole. [17] Shear-out is a particular case of bearing failure and a relation between them and hole-to-edge distance was found: when hole-to-edge distance decreases the bearing failure mode is replaced by shear-out failure. Net-tension occurs when the diameter (d) of the hole represents

a large portion of the specimen's width, always dependent of lay-up and used material. Cleavage failure can be triggered by net-section failure and tends to occur when there are not enough transverse plies or e is improper. The pull-through mode occurs specially with countersunk fasteners due to their head shape, which facilitates its pull-off. Another situation of pull-through failure could be when $\frac{t}{d}$ ratio is too high.

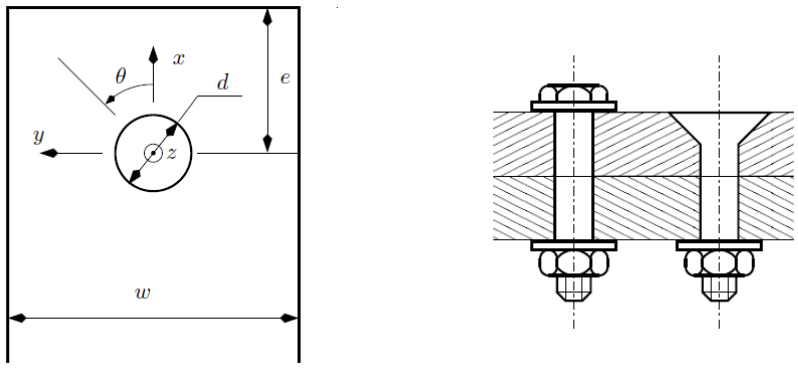

(a) Joint dimensions (b) Protruding and coutersunk fastener

Figure 4.3: Typical dimensions of joint geometry and two types of fasteners used on aircraft structures. Extracted from [1]

The effect of laminate stacking sequence is also a common parameter investigated so far. A general trend is that quasi-isotropic and near quasi-isotropic laminates provide higher failure strengths and failure modes like bearing failure and net-section failure. Whether angular plies and transversal plies are not enough or the longitudinal plies are in large quantity a premature failure mode could be developed through shear-out mode. Generally, a quasi-isotropic stacking sequence should be adopted for mechanically fastened composite joints.

The maximum bearing strengths for many joints are achieved when $2.5 < w/d < 4$ [2] or $w/d \geqslant 4$ [1] and when e/d is increased up to 4 the shear-out mode shifts to bearing failure.

The type of fastener could also influence the level of bearing strength. Some investi-

gations revealed that the higher contact area of protruding fasteners with the bolt hole ensure higher bearing strengths. The presence of washers on this type of fasteners provides also lateral constraint which avoids the spreading of damage and consequently increases the bearing strength. [1], [21]

Duthinh [22] investigated the differences between steel and FRP connections and found that for FRP connections the stress concentration around the hole is larger. This author concluded that the ductile behaviour of metals allows the relieve of those concentrations whereas a fibrous material like FRP does not have this ductility. Therefore, Hart-Smith plotted the joint efficiency according to the ratio of $\frac{d}{W}$ for 3 different materials categories and the result is illustrated on Figure 4.4. Ductile metals have higher bearing strength comparatively to the fibrous materials. For those metals the transition between bearing and net-section failure is more pronounced for a certain level of $\frac{d}{W}$ ratio. The joint efficiency is the ratio between the joint strength based on nominal cross-section and the standard unnotched strength of the material.

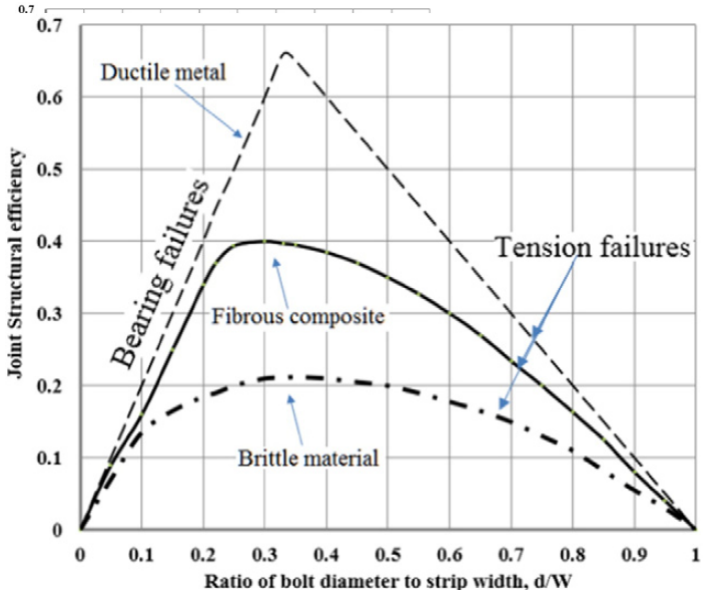

Figure 4.4: Relative structural efficiencies of bolted joints for 3 types of materials. Extracted from [4];

Kapidzic et al. [23] investigated numerically the failure of mechanically fastened composite-aluminium joints with a titanium countersunk rivet and compared the FEA results with the experimental results of Ireman [20]. The composite plate was modelled with a Progressive Damage Model known as ply-discount method which takes into consideration the accumulation of damage during the analysis. Figure 4.5 illustrates the comparison between the numerical results according to some variants and the experimental results picked from [20].

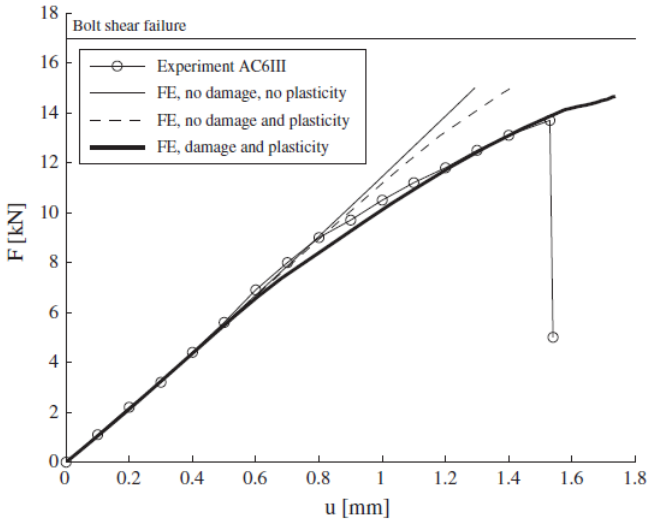

Figure 4.5: Comparison between FE results and experimental results; [23]

The author concluded that the linear response on the beginning of the load-displacement curve reveals the absence of pretension and hole clearance adopted within the FE models. The major conclusion is that joint fails by bearing failure mode through the composite and the closest numerical behaviour is obtained with the modelling of composite damage and metal plasticity. The composite damage initiates at low load levels. However, load-displacement curves do not present damage until half of the maximum load. Therefore, this behaviour should be treated carefully on design procedures. Another conclusion has to do with the thermal effects when using adherends with different CTEs. Fastener forces

for a $\Delta T = 50$℃ are of significant magnitude and should be taken into consideration on aircraft design.

4.1 Stress Prediction for Failure Modes

4.1.1 Bearing Failure

For a single-bolt composite joint, considering d as the hole diameter, t as the thickness of the laminate, P_{br} as the bearing tensile load, the bearing stress is defined as follows:

$$\sigma_{br} = \frac{P_{br}}{dt} \quad [24] \tag{4.1}$$

where σ_{br} is the bearing stress and dt is the resistance area of the fastener projected on diametral plane. When two or more fasteners are present in the same row, the resistance area dt is multiplied by n, number of fasteners in the row.

To ensure the integrity of the joint and avoid this specific failure mode, the applied tensile load should not reach the bearing tensile load,

$$P \leq P_{br} \quad [24] \tag{4.2}$$

The bearing failure behaviour is commonly influenced by several aspects as the bolt hole diameter, laminate thickness, material, lay-up, washer and clamping pressure.

Figure 4.6 illustrates a typical bearing stress-strain curve for composite bolted joints. This curve have 3 delimited regions, namely:

- Initial Sliding;
- Linear bearing response prior to the damage;

- Non linear post damage stress region.

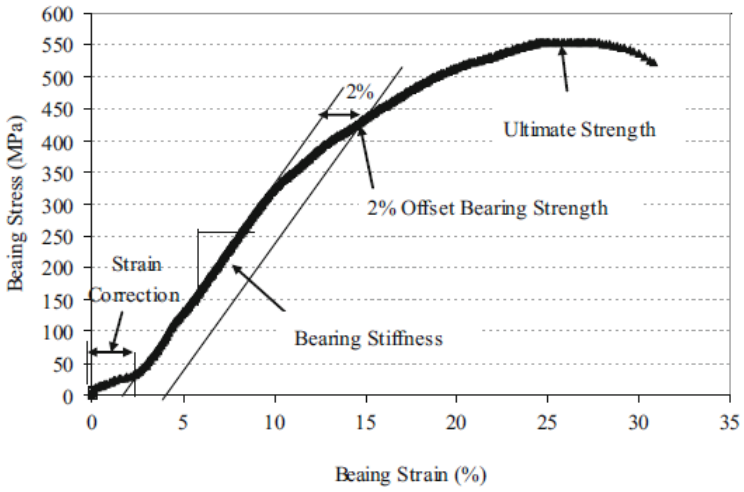

Figure 4.6: Bearing stress-strain curve of a composite bolted joint; [2]

4.1.2 Net-tension failure

For this failure mode the resistance area of the tensile load P is the area between holes. This area corresponds to,

$$A_t = (w - d)t \quad [24] \tag{4.3}$$

where d is the diameter of the hole, t the laminate thickness and w is the width of the plates. In case of a row of fasteners, the resistance area would be,

$$A_t = (w - n \times d)t \quad [24] \tag{4.4}$$

where n is the number of fasteners in a row.

Considering a single-bolt composite joint, the net-section stress is defined as follows,

$$\sigma_{ns} = \frac{P_{ns}}{(w-d)t} \quad [24] \tag{4.5}$$

where σ_{ns} is the net-section stress, P_{ns} is the net-section tensile load and $(w-d)t$ is the resistance area. For a multi-fastener joint through a single row, the resistance area is replaced by the one calculated in (4.4).

To ensure the integrity of the joint and avoid this specific failure mode, the applied tensile load should not reach the net-section tensile load,

$$P \leq P_t \quad [24] \tag{4.6}$$

4.1.3 Shear-out Failure

In case of shear-out failure the resistance areas will be along ab and cd planes as presented on Figure 4.7. The hole-to-edge distance has being represented by m. Therefore, the resistance area of shear-out failure mode is defined as follows:

$$A_s = 2mt \quad [24] \tag{4.7}$$

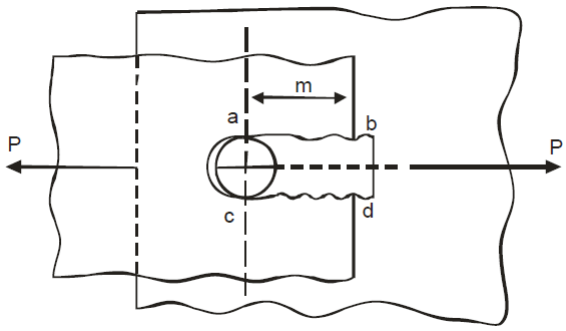

Figure 4.7: Representation of shearing planes on shear-out failure mode; [24]

For a single composite-bolt joint the shear-out stress is defined as follows:

$$\tau_s = \frac{P_s}{A_s} \quad [24] \tag{4.8}$$

where τ_s is the shear-out stress, P_s is the shear-out tensile load and A_s is the resistance areas of shear-out.

To ensure the integrity of the joint through this failure mode, the applied tensile load should not reach the shear-out tensile load,

$$P \leq P_s \quad [24] \tag{4.9}$$

Chapter 5

Adhesively Bonded Composite Joints

For adhesive bonding, the problems related to mechanical fastening as fibre damage and stress concentrations around the hole do not exist. Instead of that, the stress distribution is uniform along the overall bonded area and usually the fatigue resistance is higher than the other joint technologies. Bonded joints also avoid the problem of galvanic corrosion between the components of a fastened joint and allow the connection between any kinds of materials, since both surfaces have high enough surface energies in order to promote a correct wetting phenomena. [25] [3] The high strength to weight ratio, the electrical and thermal insulation, the conductivity and the damping ability of this type of joints are some of the most interesting abilities. [26]

Although adhesively bonded joints end up most of the problems of mechanical fastening, there are some features from this technique which are inconvenient for the service life of structural applications like the high sensibility for environment conditions as humidity and temperature, the high shear and peel stresses present at overlap edges, the impossibility of disassembly without damage and the instantaneously failure mode of this joints. Nowadays, many design engineers still have some apprehension regarding adhesive bonded joints since there is an uncertainty on the long-term service life, consequence of the characteristic problems discussed before. [27] Another issue is related to the assur-

ance of a good bonding quality and consequently this is related to the lack, in the past, of non-destructive techniques that would permit an effective detection of bad adhesions. However, in the last few years a lot of research has been performed on this field and NDT as Ultrasonics, Radiography, Thermography and Lamb waves, for example, were improved and currently employed in aero-structures when high detection resolution and accuracy is needed. [28] Recent researches revealed other potential techniques as the Electromechanical Impedance [29] and Infrared Thermography [28].

As it has been introduced before, the main categories to take into consideration when designing adhesively bonded composite joints and which could affect later the performance of a bond in service are:

- Surface preparation;
- Adherends properties and joint configuration;
- Adhesive thickness and properties;
- Environmental factors;
- Failure modes;
- Analysis through analytical methods;
- Analysis through finite element methods.

Probably, the last two items do not suit directly the intended scope of parameters that influence the bonding behaviour. However, they are two vital subjects when the topic is about strength prediction and analysis of bonded joints.

5.1 Surface preparation

Surface preparation of the adherends prior to bonding is a crucial step to ensure a good performance of the bonded joint. The links of a bonded connection requires not only a

clean surface but also an appropriate surface chemistry. The links between the adherends and the adhesive are usually covalents, although some static attractive and ionic bonds are present sometimes. Thus, if the pretreatment is correctly handled and those links are correctly established an increase on mechanical strength of the joint is obtained. Davis and Bond [30] concluded that the production of an appropriate surface chemistry will improve either the mechanical strength of the joint and the durability of the bond. It is important to understand that if the surface of adhesion is clean it does not mean reliability and good long-term life for the joint. To achieve this, the generation of a proper surface chemistry should be recognised as an important step in surface preparation.

The surface preparation procedures for thermosetting resins composites and for thermoplastic resins composites are quite different mainly due to the typical low surface energy of thermoplastics. Regarding that, solvent clean and abrasion is widely used for thermoset composites whereas the surface chemistry change and the topographical irregularity (increase of roughness) are more used with thermoplastics. These changes in terms of degreasing, roughness and chemistry composition are responsible to improve bond strength and durability.

5.2 Adherends properties and joint configuration

Joint configuration interferes directly on the strength of the joint due to the alteration of the stress distribution through-out its components. Indeed, the joint strength, for a given load, depends on the stress distribution, which depends directly on the joint geometry and properties of adhesive and adherends. Thus, a lot of research works have been performed in order to understand which configuration could provide the best option for joint designing. There is no universal optimal joint and each configuration will depend on the application, adhesive and adherends materials, the allowed budget for this design and many other variables. The single lap-joint is the most used type of joint due to its simplicity, low cost and efficiency. However, many other types are used to match industrial

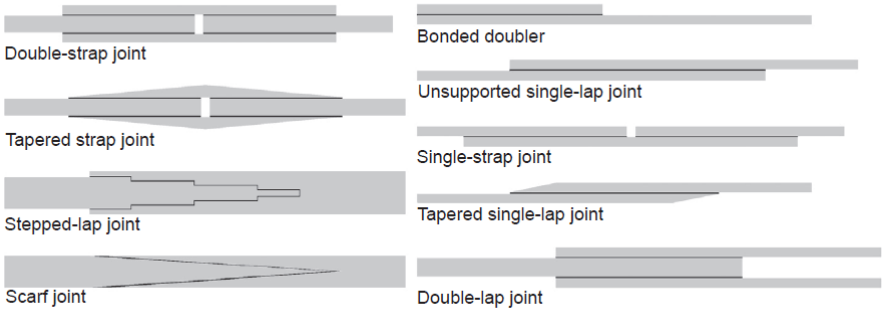

Figure 5.1: Some of typical structural joints configurations; Extracted from [31]

purposes. On Figure 5.1 some structural joint types are presented.

Some of the joints presented on Figure 5.1 are not so common to be made by composite materials because of the high machining cost and consequent fibre damage induction.

One main concern of the single-lap joints is the high level of peel stresses and shear stresses on overlap edges. When the adherends are made by composite materials, which are known by their low inter-laminar strength, the peel stress state on the overlap edge could lead to delamination of the composite adherends if an high strength adhesive is being used, for example. This event is schematically demonstrated on figure 5.2. Some research works were made in order to find geometrical configurations which would reduce the stress level on this regions. [32] [33] [34]

Manufacturing an adhesive fillet on the edges, changing the adherends shape with a tapering process on the same region or apply more than one adhesive along the overlap could be responsible for a significant decrease on peel stresses (Figure 5.3). It is important to note that each type of these solutions have a lot of possible geometrical configurations and each one presents its own level of efficiency and reliability as it was shown through some research works mentioned in [3]. Another recent studied technique is the graduation of adherends materials along the overlap region recurring to a special braiding technology. It allows for a local variation on composite adherends modulus and/or geometry. [33]

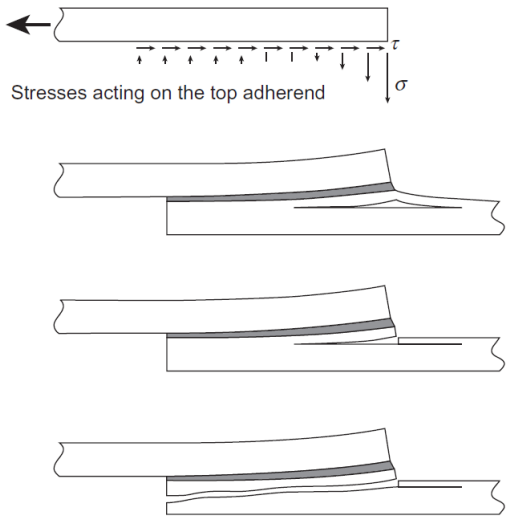

Figure 5.2: Composite inter-laminar failure due to the high stress state present on the overlap edge of and adhesively lap joint; Extracted from [3].

[34] These authors have concluded that those gradual adherends are able to smoothly decrease the peaks of stresses on overlap edges and allow for a more uniform adhesive stress distribution.

Thermal loads are a very important subject on designing adhesive joints because of the difference on coefficients of thermal expansion between materials. If two materials are bonded together and the difference on their CTE is large, high thermal loads will be developed and could promote a premature failure of the joint. The pair composite-to-aluminium is widely used for aircraft structures, however represents a risky combination since the CTE for those materials are significantly different. Composite materials usually have low CTEs and metallic materials usually have considerable values of CTEs. The effect on joint stress distribution is presented on Figure 5.4. For that cases the joint design must be dealt with precaution.

Rastogi et al. [36] investigated the thermal stresses for the latter material pair and found that the corners of the overlap area are potential zones for debonding initiation.

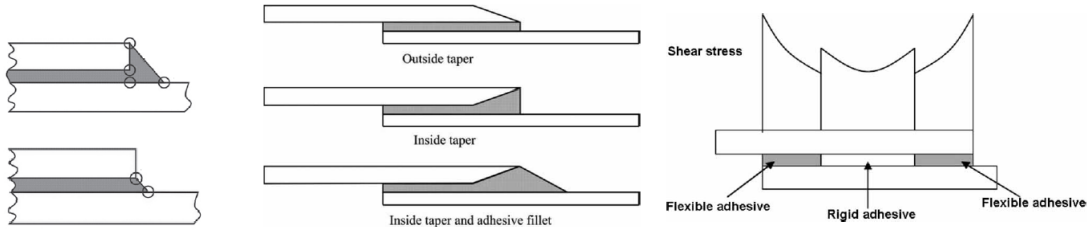

(a) Spew - fillet (b) Adherend Tapering (c) Mixed Adhesive

Figure 5.3: Used techniques to decrease the peel stresses on composite adherends; Adapted from [35] and [3].

The thermal stress effects should be considered on designing adhesively bonded joints because they lead to a joint strength reduction in most of the cases. [37]

The overlap length could be considered as a factor that affects joint strength and the each type of adhesive will have its own influence on joint strength along different overlap lengths. There are 3 universal cases which should be considered for the influence of the overlap length on the joint strength [3]:

- Elastic adherends and ductile adhesive;
- Elastic adherends and brittle adhesive;
- Adherends that yield.

The latter case is not valid for composite bonded joints since composite laminates exhibits an elastic behaviour. For the first case, the joint strength is almost proportional to the overlap length because of the ability of the ductile adhesive to redistribute the stresses along the bonded area. If the bonded area increases, the redistribution will increase and the joint strength will be upgraded. For the second case, the same does not happen and for a certain level of strength a plateau is reached because of the main concentration of stresses at the overlap edges. A longer overlap will not redistribute or alter the shear stress distribution on that case. Therefore at some point, the increase of

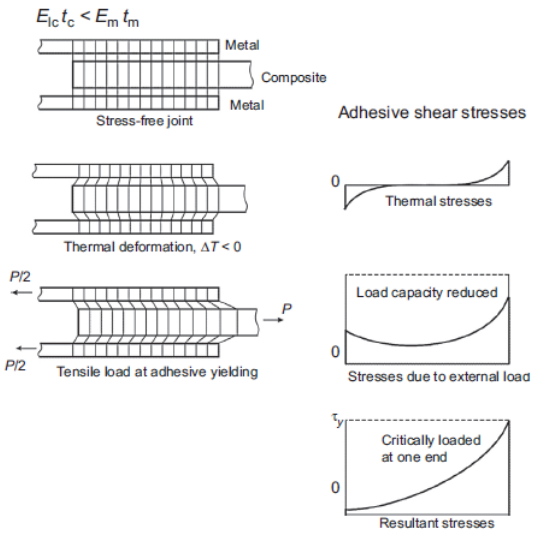

Figure 5.4: Shear stress developed through the adhesive overlap on a DLJ due to bonding materials with different CTEs (Composite-metal, where composite has lower longitudinal stiffness than the metal); [3]

the overlap length will be useless. Those differences on joint strength could be consulted on Figure 5.5 where the results of an investigation performed by Neto et al. [38] shows the dissimilar evolution of joint strength as a function of overlap length according to the use of a ductile adhesive (*SikaForce 7888*) or a brittle adhesive (*AV138*).

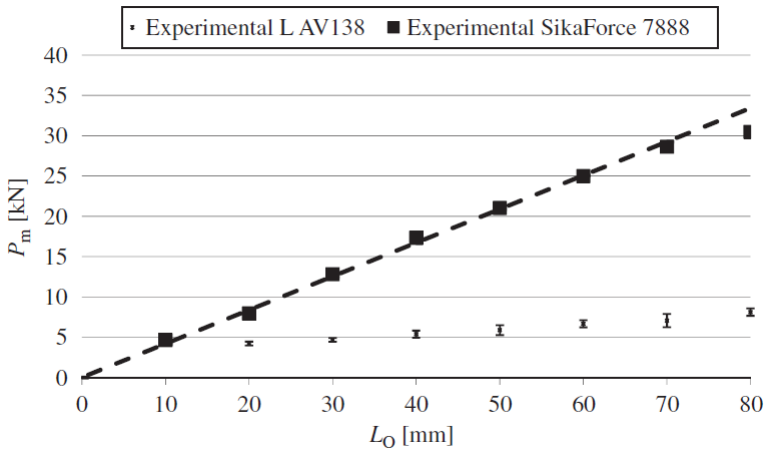

Figure 5.5: Experimental failures loads for composite single-lap joints bonded with a ductile adhesive (*SikaForce 7888*) and a brittle adhesive (*AV138*)[38]

5.3 Adhesive Properties

The adhesive strength and the joint strength are two completely different subjects and could not be comparable. Such comparison cannot be made because the joint strength depends not only on the adhesive strength but also on the ductility and flexibility of the adhesive. For ductile adhesives, the ability of the joint to uniformly distribute the stress will provide an higher joint strength although the adhesive itself is considered less stronger and has a lower modulus. For a brittle adhesive, the stresses usually concentrates on the overlap edges unlike the ductile adhesive which is able to redistribute the stress along the less stressed parts. Figure 5.6 illustrates this comparison for shear stress distribution. [3]

There are a wide series of adhesive types on the market and each one adapts better to the aim of each application. The selection of an adhesive could depend on many other factors such as the type of adherends to be bonded, the in-service temperature of the joint, the curing method and curing cycle, the application method and so on. They could be divided into categories and each of these categories could be directly related to some features. These features are in agreement with most of structural types of requirements.

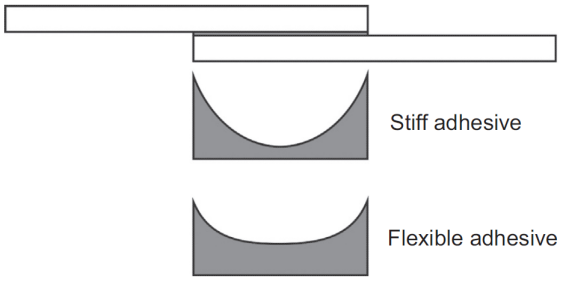

Figure 5.6: Effect of adhesive modulus on shear stress distribution; [3]

Table 5.1 provides some information about adhesive categories.

Table 5.1: Adhesive categories and respective features characterization; Adapted from [35]

Categories	**Features**
Epoxies	High strength and temperature resistance;
Cyanoacrylates	Fast bonding ability; Poor resistance to environmental factors;
Anaerobics	Suitable for sealing and tightening purposes;
Acrylics	Versatility; Suitable to bond non-treated surfaces; Fast curing;
Polyurethanes	Flexibility at low temperatures; Good fatigue strength;
Silicones	Excellent sealant; Good flexibility; Temperature resistance; Low stresses;
Phenolics, Polyimides and Bismaleimides	High-temperature resistance;

When an adhesive is applied to a specific application, its mechanical properties should

be already known and the adhesive should be already fully characterized. The joint strength prediction is not performed if the knowledge of the single adhesive behaviour is not well defined. Therefore, the mechanical properties and the mechanical behaviour of the adhesive are previously attained recurring to some experimental tests, correctly documented through ASTM and ISO standards.

5.4 Environmental factors

During the service life of an adhesive, it could be subjected to various environmental conditions and those conditions could affect the performance and the properties either of the adhesive or the whole joint. Temperature and humidity are the main environmental factors that could influence the reliability and durability of an adhesive joint and should be considered as critical factors when design is taken. Those factors produce physical and chemical changes on adhesive structure whether it is exposed for a long period. When moisture infiltrates through the adhesive it will not be only degrading adhesive strength but also the wellness of the interface between adherends and adhesive.

For FRP adherends, the mechanisms of moisture absorption are slightly different from the metal bonded joints. Wright [39] found that moisture entrapment on epoxy composite joints is responsible for a positive work of adhesion, which decreases the probability of interfacial failure for this type of joints. On the other hand Kinloch [40] agree that the presence of temperature and moisture within FRP materials could diminish mechanical properties and weaken the interface link between matrix and fibres. Moisture absorption from an adhesive or an FRP matrix (polymeric material) could lead to reversible and irreversible phenomenas known as plasticization, swelling and degradation.

Storing a composite laminate for long time also is not a healthy way to achieve the best performance of a bonded joint, since during this time the material is able to absorb significant quantities of humidity which would result on strength reduction. Thus, every time a composite is taken from a freezer, it should be dried before application. This

procedure will not permit the deterioration of the joint strength due to moisture effects. [41]

Nowadays, to predict failure and to model the behaviour of bonded joints subjected to specific environmental conditions, as moisture absorption for instance, Cohesive Zone Modelling (CZM) is being widely used with very good agreement between experimental and numerical tests.

Despite many studies have been performed about the influence of environmental conditions on the reduction of adhesive properties, there remains a lack of data for failure and fracture behaviour from specific combination of adherends and adhesives. As bonded joints are composed by some components (adherends and adhesives) and certain interphase regions the efficient understanding of the individual behaviour of each component should be done and only after that, the study of whole joint must be performed. Since from each constituent there are different reactions to environmental conditions, those reactions could affect the behaviour of the joint as a whole.

5.5 Failure modes

Failure modes of adhesively bonded joints depends directly on 3 parameters: quality of the bond, load level and joint configuration. Those subjects should be fully characterized to permit a better understanding of the failure region upon collapse. This concept works well for metallic bonded joints, for example (Figure 5.7) whereas for FRP laminate composite joints the failure strength and mode prediction remains a bit more complex. Failure modes for FRP laminate composite joints are illustrated on Figure 5.8. The changing of failure strength and failure modes in function of bonding methods and its parameters do not permit good predictions. Therefore, for FRP composites joints the possible modes of failure are different from the ones detected with metallic adherends. They could be one of the followings:

- Adhesive failure;
- Cohesive failure;
- Thin-layer cohesive failure;
- Fibre-tear failure;
- Light fibre-tear failure;
- Stock-break failure;

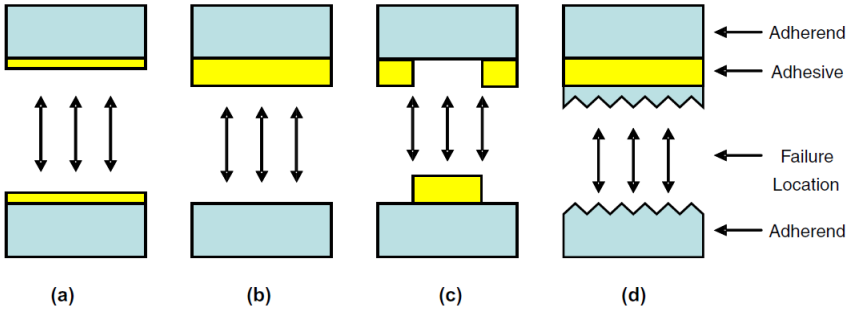

Figure 5.7: Failure modes definition for adhesively bonded joints with metallic adherends: a)Cohesive failure b)Adhesive failure c)Mixed failure d) Adherend Failure. Extracted from [27]

Figure 5.8: Possible failure modes for adhesively bonded joints with FRP laminate composite adherends; Extracted from [35]

5.6 Strength Prediction

For correctly designing a bonded joint, the stress state in service must be predicted, the failure load should be, at least, roughly known and the possible regions of failure must be understood to permit the correct design and suitability of the final joint. However, the prediction of failure strength could be performed recurring to many types of methods, because failure strengths will vary according to the various bonding methods and their correspondent parameters. In fact, there are two basic mathematical approaches to determine the failure strength of a designed joint:

- Closed-form analyses (analytical methods);
- Numerical methods (finite element analyses).

5.6.1 Closed-form analyses

The first analytical model to predict the behaviour of an adhesively bonded joint was presented in 1938 by Volkersen. However, this model did not account for the bending moment of the adherends and shear deformations of the joint. Thus, Goland and Reissner adapted the last model to a new one, where peel and shear stresses are taken into account. After that, Hart-Smith proposed a following model where the behaviour of the adhesive was completely reformulated. On this model, the adhesive layer is modelled with an elasto-plastic behaviour and the maximum load taken by the adhesive depends on the shear deformation energy. Thermal stresses were also take into account and the author concluded that as the adherends thickness or stiffness increases, there is a reduction in joint strength. The analytical model of Hart-Smith allows a good approximation, specially for the behaviour of ductile adhesives. A significant list of analytical models for adhesively bonded joints with FRP composite adherends is presented on literature. [35] Those models consider a linear elastic behaviour for the adherends because the use

of non-linear behaviour due to plasticity of the adherend would make the model very complex in terms of mathematical formulation. The adhesive layer sometimes is modelled with non-linear behaviour. Some models use the classical laminate plate theory with or without coupling effects or the laminate anisotropic plate theory. A wide combination of approaches is available between the research community nowadays. [35]

5.6.2 Finite Elements Method

The level of complexity reached with some models and the demand to model in-service behaviour of an adhesively bonded joint through various non-linear properties opened a new chapter on modelling tools with the arise of numerical methods. Finite elements method is the most used one on structural engineering.

This method allows to perform analysis of very complex shapes of joint configurations and nevertheless, it is possible to add very complex material behaviours, environmental conditions, varying loads, a significant number of boundary conditions, etc. However, the failure prediction is still a very complex subject since it depends from a significant number of variables as bonding methods and bonding parameters. The lack of a reliable failure criteria limits the widespread of this technique through an high number of structures and applications. The high cost and the time spent with experimental tests carried now before every joint design contributes to the avert of some engineers to this technology.

However, there are 3 approaches which are intended to predict joint strength and understand the behaviour of adhesively bonded joints with FRP laminate composite adherends. There are:

- Continuum mechanics approach;
- Fracture mechanics approach;
- Damage modelling.

According to the continuum mechanics approach, the modelling is performed considering a perfect bonding between the adhesive layer and the adherends with both being modelled by continuum elements. Upon the simulation, the strength prediction is based on maximum values of stress, strain or plastic energy, for example. However, some problems could arise due to the bi-material singularities available on bonded joints and the mesh-dependency of stress/strain methods. [35] Despite this disadvantages, these type of approach is commonly used for practical applications on industry due to its simplicity and convenience.

Unlike the continuum approach, the fracture mechanics approach uses an energy based failure criteria, where the toughness has the main role. One of the methods is based on the initiation and development of a fracture path starting on a crack tip. It is necessary to know the instantaneous energy release rate according to the different fracture modes during the simulation. The failure occurs when a local mode or mixed mode energy release rate criteria is reached. VCCT is a well-known method for failure criteria although it is only suitable for Linear Elastic Fracture Mechanics (LEFM). Another inconvenient is the need for an initial crack.

Another approach within the fracture mechanics assumes that the the defects or voids on a adhesively bonded joint are not macroscopic large enough to induce a crack initiation. Thus, the criteria is addressed with no initial crack and a generalized stress-intensity factor allows the prediction of fracture initiation. [35]

5.6.2.1 Damage Modelling

Through a single analysis, the progressive damage modelling allows to obtain the complete response of a structure along its load request. Nowadays it is an emergent field due to its ability to cover both previous approaches. The Cohesive Zone Model arises as a solution for the problems of the old approaches. Therefore, it is possible to analyse the linear evolution of the stresses during the first stage of carrying, damage initiation, the

consequent properties softening and the damage propagation through the adhesive until the final failure of the component. For this technique a traction-separation law is applied to failure paths and is ruled by the relationship between cohesive stresses and relative displacements connecting paired nodes of cohesive elements. Those traction-separation laws could be related to a pure mode (I or II) or to a mixed-mode where the combination of both modes for the initiation and propagation of damage are considered. Mode III is not considered through several investigations because most of the work done on this area was performed with 2D numerical models. For the case of 3D models, the t shear component of stress and strain should be included. Figure 5.9 illustrates two triangular traction-separation laws according to a fracture pure mode and a fracture mixed mode. Linear elastic evolution is visible at the beginning, followed by linear damage evolution.

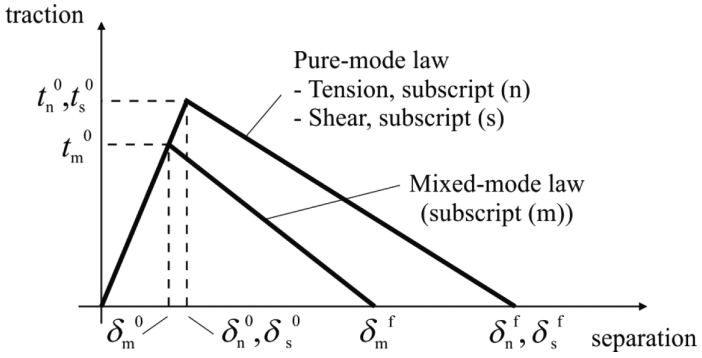

Figure 5.9: Triangular traction-separation laws for pure mode and mixed mode with linear softening; [42]

Dissimilar behaviours of a wide range of adhesives demand different law shapes for damage modelling. Thus, some cohesive law shapes have been studied in order to understand which one will suit better each type of adhesive for each overlap length. The law shapes investigated by Campilho et al. [43] were the triangular law shape, the exponential law shape and the trapezoidal law shape, all of them available on the commercial FEA software *Abaqus®* and presented on Figure 5.10. Those authors concluded that although

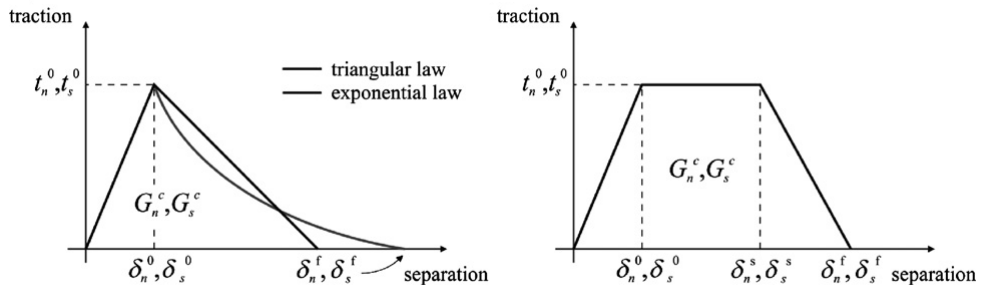

Figure 5.10: Triangular, exponential and trapezoidal traction-separation laws for mixed mode; [43]

the triangular shape is widely used due to its simplicity, convenience and easier convergence, for ductile adhesives the trapezoidal shape is more suitable because it captures the adhesive plastic flow at the end of plastic region. The brittle ones are more preciselly modelled by the triangular shape although any of them could ensure a good approximation with the experimental curves. Ridha et al. [44] performed an investigation on progressive failure of bonded scarf joints on composite repair panels and concluded that the use of a linear softening for ductile adhesives will under predict the experimental strengths of nearly 20 % because of premature softening on the overlap edges after damage initiation which is not coincident with the experimental behaviour of this type of adhesives.

For the fulfilment of this technique some parameters should be obtained to model the constitutive equations. For a triangular law shape, the initial linear elastic evolution is governed by an elastic constitutive matrix that relates tensile and shear stresses with tensile and shear strains,

$$\mathbf{t} = \begin{Bmatrix} t_n \\ t_s \\ t_t \end{Bmatrix} = \begin{bmatrix} K_{nn} & K_{ns} & K_{nt} \\ K_{ns} & K_{ss} & K_{st} \\ K_{nt} & K_{st} & K_{tt} \end{bmatrix} \begin{Bmatrix} \varepsilon_n \\ \varepsilon_s \\ \varepsilon_t \end{Bmatrix} = \mathbf{K}\boldsymbol{\varepsilon} \quad [38] \tag{5.1}$$

where K values are the stiffness parameters of the adhesive, $\boldsymbol{t}$ and $\boldsymbol{\varepsilon}$ are the tensor of stresses and strains, respectively, through each adhesive failure modes. For thin adhesive layers on 2D numerical models an approximation could be made assuming that $K_{nn} = E$, $K_{ss} = G$ and $K_{ns} = 0$ and the previous matrix will be simplified in order to remove the t component of the parameters.[38] For damage initiation, several criteria could be adopted and some parameters should be known, as the cohesive strengths for normal (t_n^0) and shear (t_s^0, t_t^0) modes. For example, the collection of available criteria on *Abaqus®* software [45] are listed below,

- Maximum nominal stress criterion;
- Maximum nominal strain criterion;
- Quadratic nominal stress criterion;
- Quadratic nominal strain criterion.

Maximum nominal stress criterion

Damage initiates when the maximum nominal stress ratio defined in the expression below reaches a value of one,

$$max \left\{ \frac{\langle t_n \rangle}{t_n^0}, \frac{t_s}{t_s^0}, \frac{t_t}{t_t^0} \right\} = 1 \quad [45] \tag{5.2}$$

Maximum nominal strain criterion

Damage initiates when the maximum nominal strain ratio defined in the expression below reaches a value of one,

$$max\left\{\frac{\langle\varepsilon_n\rangle}{\varepsilon_n^0},\frac{\varepsilon_s}{\varepsilon_s^0},\frac{\varepsilon_t}{\varepsilon_t^0}\right\}=1 \quad [45] \tag{5.3}$$

Quadratic nominal stress criterion

Damage initiates when the quadratic nominal stress function involving the nominal stress ratios defined in the expression below reaches a value of one,

$$\left\{\frac{\langle t_n\rangle}{t_n^0}\right\}^2+\left\{\frac{t_s}{t_s^0}\right\}^2+\left\{\frac{t_t}{t_t^0}\right\}^2=1 \quad [45] \tag{5.4}$$

Quadratic nominal strain criterion

Damage initiates when the quadratic nominal strain function involving the nominal strain ratios defined in the expression below reaches a value of one,

$$\left\{\frac{\langle\varepsilon_n\rangle}{\varepsilon_n^0}\right\}^2+\left\{\frac{\varepsilon_s}{\varepsilon_s^0}\right\}^2+\left\{\frac{\varepsilon_t}{\varepsilon_t^0}\right\}^2=1 \quad [45] \tag{5.5}$$

The $\langle\rangle$ brackets are known as *Macauly Brackets* and they mean that a purely compressive stress state does not induce damage. [38]

The damage evolution upon the onset of damage could present many shapes as discussed before (Triangular, Exponential and Trapezoidal). For these shapes, an energy or a displacement approach could be adopted although the first one is widely used for adhesively bonded joints. The damage evolution on this case is defined by a relationship between the instantaneous energy released rates G_n, G_s and G_t and the fracture energies

in tension (G_n^C) and shear (G_s^C and G_t^C) . The fracture energy is equal to the area under the traction-separation law curve. Within the chapter of energy evolution laws for mixed fracture modes and according to *Abaqus®* Documentation [45] it is possible to divide them through the follow categories:

- Tabular form;
- Power Law form;
- Benzeggagh-Kenane form (BK).

Power Law form

The failure under mixed mode on that case is governed by a power law evolution which allows the interaction between the required fracture energies to cause failure on individual modes. When the following condition is satisfied the damage evolution becomes a complete failure of the adhesive.

$$\left\{\frac{G_n}{G_n^C}\right\}^\alpha + \left\{\frac{G_s}{G_s^C}\right\}^\alpha + \left\{\frac{G_t}{G_t^C}\right\}^\alpha = 1 \quad [45] \tag{5.6}$$

where α is the power coefficient.

Benzeggagh-Kenane form (BK)

This fracture criteria was developed by Benzeggagh & Kenane, 1996 and is useful for adhesives with the same critical fracture toughness for mode II and III, $G_s^C = G_t^C$, i.e. the shear fracture behaviour can be treated as isotropic.

$$G_n^C + (G_s^C - G_n^C)\left\{\frac{G_S}{G_T}\right\}^\eta = G^C \quad [45] \tag{5.7}$$

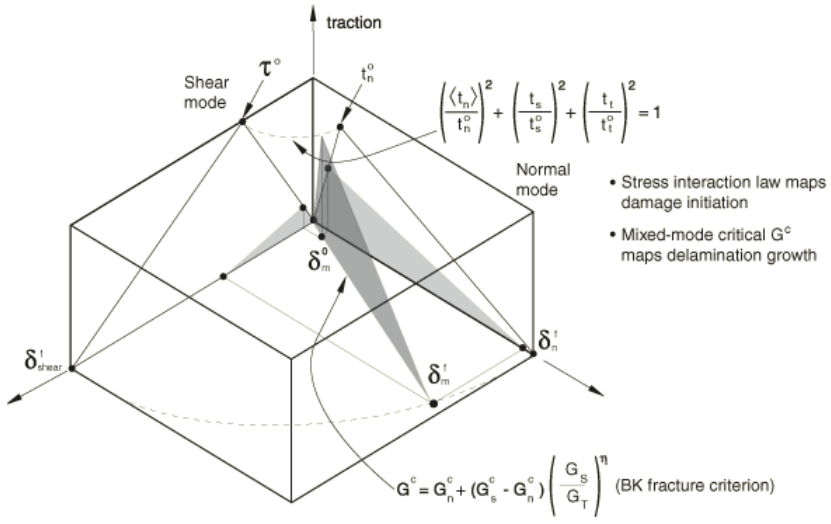

Figure 5.11: Mixed-mode response of cohesive elements with a triangular traction-separation law; Damage initiation criterion - quadratic nominal stress; Damage evolution criterion - Benzeggagh-Kenane; [45]

where $G_S = G_s + G_t, G_T = G_n + G_S$ and η is a material parameter.

It is important to note that *Abaqus®* allows these formulations only for linear and exponential evolutions of damage. If a trapezoidal law is pretended to be modelled through an energy mixed mode power law form this software does not allow it and another type of formulation should be adopted as, for example, the effective displacement damage evolution used on [43].

Figure 5.11 illustrates a general mixed-mode response of cohesive elements where a mixed-mode triangular traction-separation law is applied in combination with a quadratic nominal stress criterion for damage initiation and an energy Benzeggagh-Kenane fracture criterion for the damage evolution.

For the estimation of the parameters for the CZM (as the cohesive strengths and the critical fracture energies, for example) a few techniques are available and are known as

property identification technique, direct method and inverse method. However, although there are some options to perform this estimations, each technique has its own respective accuracy and complexity.

Chapter 6

Bonded-Bolted Composite Joints

Bonded-bolted joints could be considered as joints with an adhesively bonded area between a certain number of adherends with the addition of one or more fasteners along drilled holes through the adherends in order to achieve some specific properties or specific application purposes. One of the first works on this subject was performed by Hart-Smith [21] and consisted on a static strength design and analysis of high load transfer joints in advanced composite structures through the development of a set of Fortran computer programs. Large titanium to carbon/epoxy stepped bonded joints reinforced by mechanical fastening were theoretically investigated. The research was divided by three different sections. On the first one, the behaviour of intact bonded-bolted lap joints is studied, on the second one the use of bonding and bolting in repairs is discussed and the third one is based on the use of bonding and bolting in order to achieve damage tolerance.

The first specimen's geometry submitted to analysis is illustrated on Figure 6.1 and the bolts load transfer represents a small portion (barely 1%) of the total applied load, which can be explained by the stiffer load path of the adhesive. The adhesive is stronger than the adherends, so the critical location will be at the first bolt of the composite section.

Hart-Smith performed a comparison between the previous bonded-bolted joint and

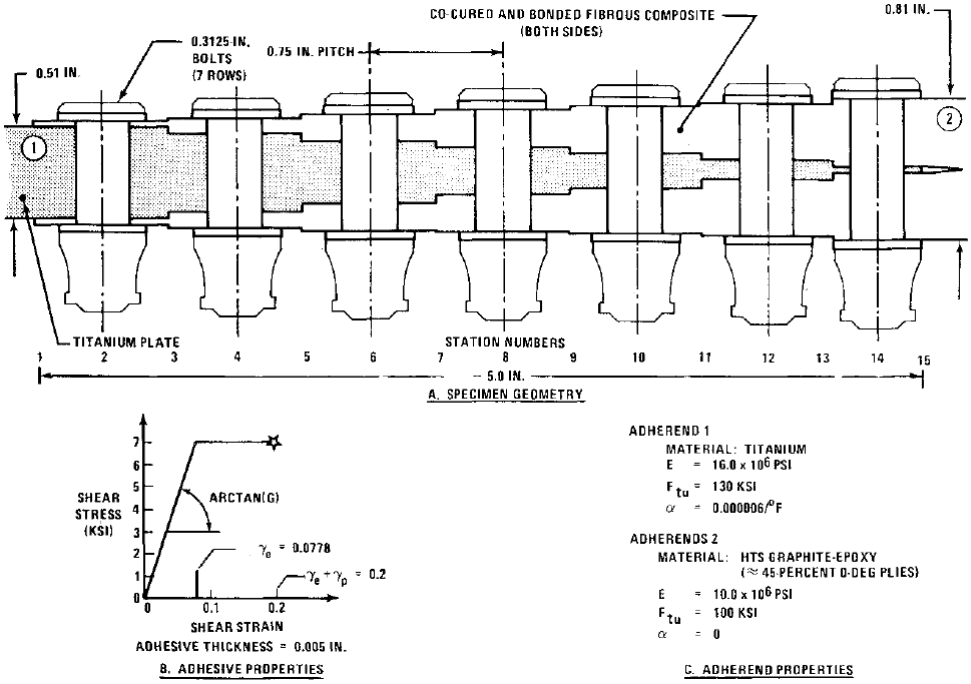

Figure 6.1: Joint geometry for the first analysis and the corresponding material properties; [21]

another two configurations: 1) keeping only the adhesive bond and 2) keeping only mechanically fastened connections. According to the results presented on Figure 6.2, the total adhesive bonded joint transfers slightly more load than the bonded-bolted joint since the removal of the bolts moved the critical location on composite laminate. For the fastened joint, the load transfer values are still below the load transfer values from totally bonded and bonded-bolted joints. However, the difference between those load transfer values is not too high. This can be explained by the higher relative displacement of the adherends for this joint configuration. With higher relative displacement of the adherends, there is an increase of joint flexibility. This flexibility induces a reasonable level of shear stresses through the cross-section of the bolts and are responsible for an increase of load transfer of about 70 times. This phenomena is also confirmed by Kelly [46].

The primer conclusion is, if a bonded-bolted joint is well designed, the load path through the adhesive bond will be stiffer than the load path through the bolt. Therefore, the contribution of fasteners to load carrying can be considerably low or even insignificant. Hart-Smith affirms that the combined joint strength is clearly not the sum of individual joint strengths and concluded that the use of bonded-bolted composite joints could be interesting only for repair and damage tolerance.

The second scenario consists on creating a deliberate disbond in the middle of the stepped joint for the bonded-bolted and total bonded joints in order to understand the effect on bolt load transfer and on adhesive's shear stress distribution. This flaw is located along 3 centre steps of the joint presented on Figure 6.1. On Figure 6.3, shear stress distribution for each disbond is presented. Clearly, for the right case, the fasteners on the middle region will carry higher loads than the outer ones. The peak of shear stresses changed its location to the boundary of the disbond and a load redistribution around the flaw takes place, comparatively to Figure 6.2. Hart-Smith affirms that this peak's movement is related to the size of the disbond but there is no universal flaw size to induce this kind of shift.

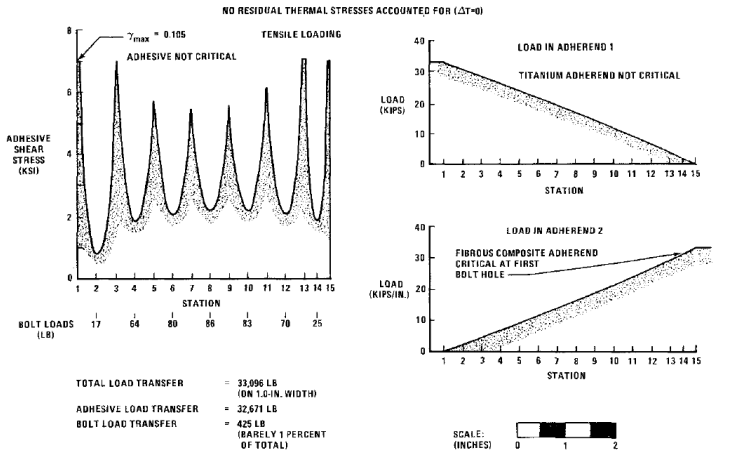

(a) Bonded - bolted joint

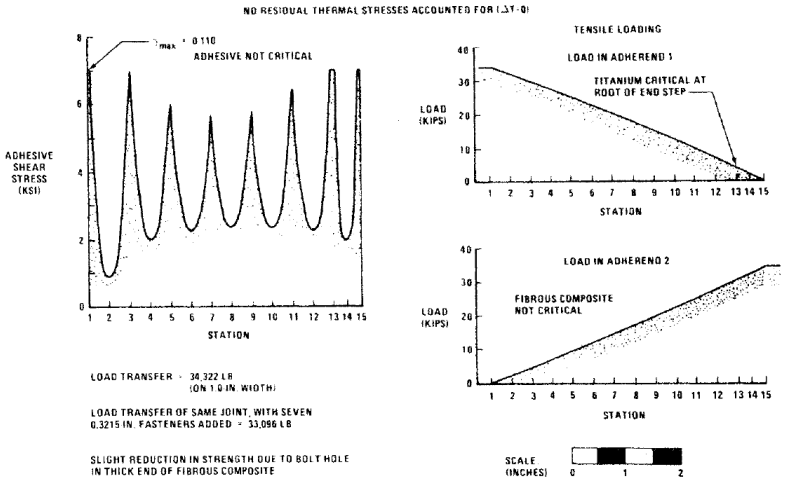

(b) Bonded joint

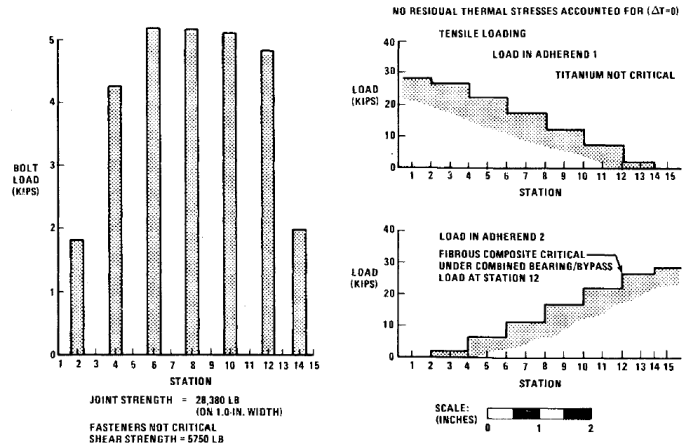

(c) Mechanically fastened joint

Figure 6.2: *Left:* Load transfer through three types of joint connections in function of overlap length/bolt position; *Right:* Withstood load by each adherend in function of overlap length; Adapted from [21].

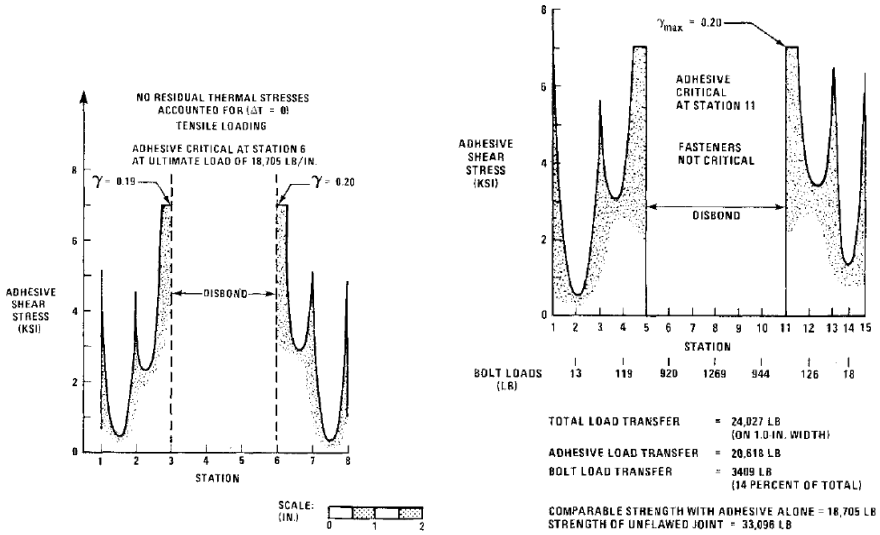

(a) Bonded joint (b) Bonded - bolted joint

Figure 6.3: Load transfer and shear stress distributions for a joint with an adhesive flaw at the centre region of the overlap; [21]

Although the bolts on the flaw are carrying significant levels of load, it represents only 14% of the total applied load. An interesting conclusion has to do with the ability of the middle bolts to reduce the critical adhesive strain on the boundary of the flaw. This reduction allows the adhesive to carry higher loads on the remaining area. For that reason, the adhesive in the fastened case is taking higher stresses (20.618 lb/in.) than in the bonded flawed one with no fasteners (18.705 lb/in.).

The third scenario is based on the use of bonding and bolting to achieve damage tolerance. According to Hart-Smith for bonded composite adherends in which one of them is broken or has a abrupt flaw without initial damage, the presence of bolts can provide a fail-safety mechanism for the bond and avoid the spreading of delamination through the entire structure. The use of fasteners on bonded joints could arrest the damage of an adhesive disbond or provide enough joint strength when the adherend's delamination is intended to grow up through the section of the laminate. On Figure 6.4

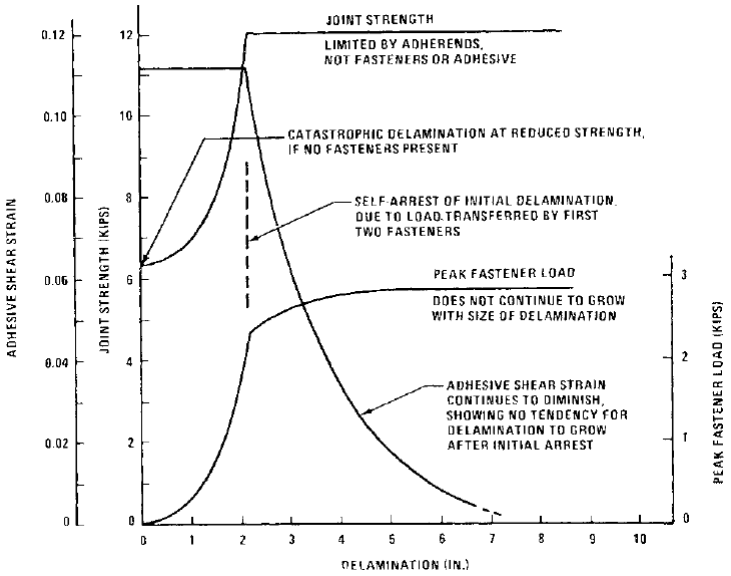

Figure 6.4: Damage tolerance for a bonded-bolted joint in function of delamination's size; [21]

it is illustrated the ability of a bonded - bolted joint to confine damage, to decrease the shear strain of the adhesive while delamination is developing and to follow the initial joint strength.

Lin [47] studied the failure modes and fracture behaviour of single-lapped mixed composite joints varying bolt arrangements, type of adhesive and clamping pressure through a C-Scan NDT (non-destructive) method.

The adherends were divided in cross-ply and quasi-isotropic, both made of graphite/epoxy laminates. A thermosetting (CN- Cyanoacrylate) and a thermoplastic (EA 9317) adhesive were used. Regarding the individual mechanical properties of those adhesives, the thermal-plastic one presents a better performance due to its high temperature resistance and its improved elongation with no loss of strength. In terms of fasteners, a 304 stainless steel bolt and a NAS 1919 C05 rivet were adopted, with 4 types of bolt arrangements:

- 1 x 1 (one bolt);

- 1 x 3, 3 x 1 (three bolts);
- 2 x 3 (six bolts);
- 3 x 3 (nine bolts).

where the first number of the arrangement indicates the number of bolts through the width of the specimen and second number indicates the bolts through the overlap length.

The chosen value for clamping pressure was 30 MPa because is the one which ensure the highest joint strength according to some numerical models developed. Mathews suggests a value of 25 MPa. [48]

The highest joint strength was achieved with the 2 x 3 (six bolts) arrangement due to the high disposition of bolts along the overlap. Higher overlaps provide higher joint strengths until the achievement of a constant asymptotically value. However the increase on bolts placement along the overlap should be treated carefully since it could create more damage zones.

Although the EA 9317 is individually better than the CN adhesive, when applied to a joint the CN adhesive shows a better performance. The design project for adhesive joints should take into consideration the mechanical properties of the adherends. Adherends with high modulus shall be bonded with an high modulus adhesive and adherends with low modulus shall be bonded with a low modulus adhesive.

The samples made by cross-plies presented an high level of strength comparatively to quasi-isotropic laminates. However, the author defends the use of the latter one since it allows more loading directions which is what mostly occurs on practical applications.

Lin demonstrated as well that tapering free lap edges prevents delamination and increase strength.

Kelly [46] investigated the load transfer in bonded-bolted composite single-lap joints through two type of methods. The first method was based on a parametrised finite element

model used to predict the load transfer by the adhesive and the bolt. This analysis was based on a calculated ratio of load transferred between the adhesive and the bolt for different joint configurations.

The second method was used to predict and validate the results of the finite element model, using an instrumented bolt that allows to measure shear load. At the end, the results from both methods were found to be in agreement.

This study concludes that the presence of the bolt have a low effect on the load at the ends of the overlap, while the maximum shear stress of the bonded-bolted joint is 50% lower than the shear stresses of the bonded joint.

Some other aspects were also object of analysis, like the adherend thickness, the adhesive thickness, the pitch distance and the adhesive modulus. With increasing the thickness of the adherends, the shear stress on the adhesive will be higher and the secondary bending will be lower which cause an higher x-displacement of the adherends. The higher x-displacement of the adherends produces an increasing of bolt load transfer. This relationship is shown on Figure 6.5 (a).

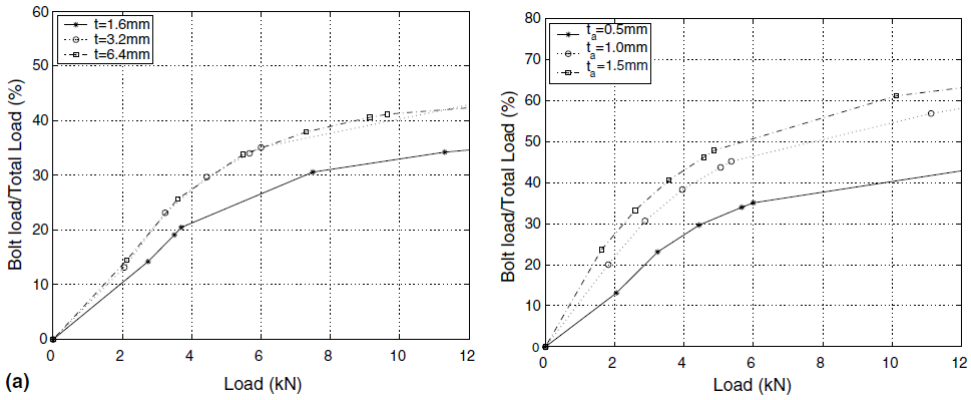

(a) Adherends thickness (b) Adhesive thickness

Figure 6.5: Effect of adherends and adhesive thickness on bolt load transfer; [46]

Relatively to adhesive thickness, Kelly affirms that a joint with an higher adhesive thickness will provide a better flexibility of the joint and this flexibility is responsible

for increasing the relative displacement of the adherends. The increase on relative displacement of the adherends allows the bolt to have contact with the adherends and this phenomena will cause more transferred load.These results could be consulted on Figure 6.5 (b).

The joint overlap length has also a significant influence on bolt load transfer. Kelly found that with increasing the overlap length the role of the bolt is less important than with lower overlap lengths. As large overlap lengths cause a reduction on average shear stresses at the centre area of the lap, the bolt, which is located on this region will transfer less load than for short overlap lengths where the stress state is higher either on edges or on middle region. Another explanation can be based on the relative displacements of the adherends. As larger overlaps produce a minimum secondary bending, the relative displacement of adherends is low and the bolt transfer load will not be too high comparatively to the bolt transfer load of short overlap lengths. This relationship can be over viewed in Figure 6.6 (a).

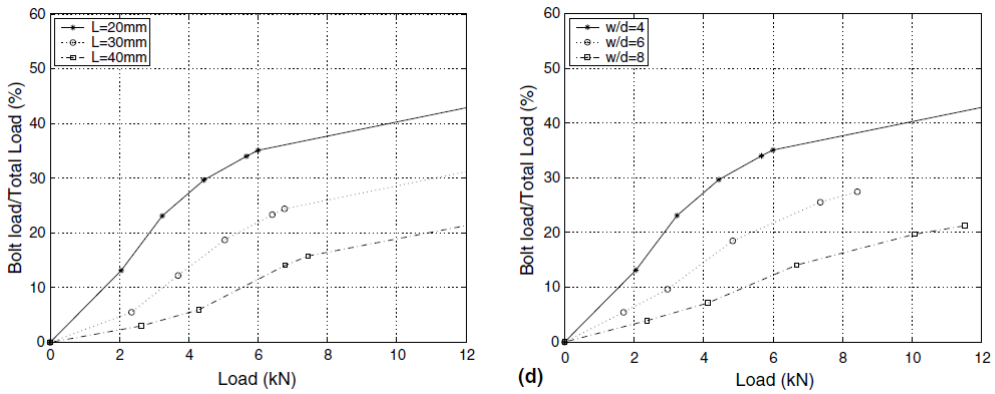

(a) Overlap length (b) Pitch distance

Figure 6.6: Effect of overlap length and pitch distance on bolt load transfer; [46]

The fastener pitch distance is considered the distance between fasteners in a row. For a single-lap joint with only one fastener, the pitch distance can be considered equal to the width of the adherend (w). For study purposes the parametric analysis was performed

considering w/d ratios and keeping d constant. Despite the widely known influence of this parameter on failure modes of composites, in terms of bolt load transfer an increase of pitch distance results in a reduction of load transfer. This increase will reduce as well the changing rate of load transfer with total applied load. This reduction of load transfer could be explained by the increase of bonded area which will be responsible to withstand the most part of the load. The relationship between the bolt load transfer and the total applied load for 3 different w/d ratios is presented on Figure 6.6 (b).

The adhesive modulus can affect as well the ratio of bolt load transfer. According to the work of Kelly, 3 adhesives were used for investigation. Two of them were epoxy adhesives while the third one was a polyurethane. The experimentally obtained tensile-strain curves of these adhesives are presented on Figure 6.7 (a). Figure 6.7 (b) illustrates the influence of different adhesive modulus on bolt load transfer. It is possible to understand that adhesives with higher modulus will provide less bolt transfer load, whereas ductile adhesives as *Pilogrip 7400/7410* ensure an higher ratio of load transferred by the bolt. Stiffer adhesives are responsible for carrying more load than ductile ones and another reason for that results could be the increase of relative displacement of the adherends when bonded with a ductile adhesive as *Pilogrip 7400/7410*. As it was referred before, high relative displacements of the adherends lead to higher ratios of bolt load transfer.

Kweon et al. [27] performed an experimental study with composite-to-aluminium double lap joints in order to understand the influence of combined mechanical fastening and adhesive bonding on failure modes and to establish a comparison between three types of joints: bolted joint, bonded joint and bonded-bolted joint. Two types of adhesive were used: a film adhesive and a paste adhesive. The latter one is more brittle and have a lower shear strength. For analysis purposes the joint strength was considered as the maximum carried load divided by the cross-sectional area of the laminates adherends since they are prone to delamination.

The typical failure modes of bonded-bolted specimens were mixed failure with some

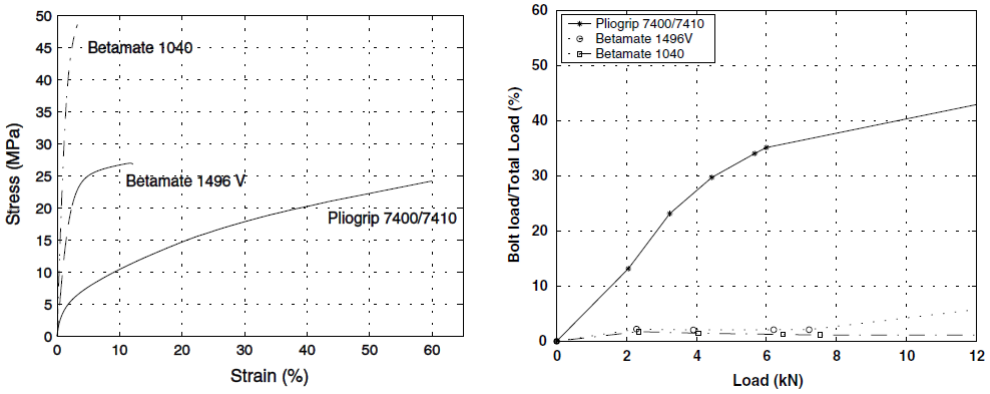

(a) Adhesives characterization (b) Adhesive modulus

Figure 6.7: Tensile stress-strain curves for those 3 adhesives under investigation and the effect of adhesive modulus on bolt load transfer; [21]

composite delaminations, which remained bonded to the aluminium adherend, and bearing failures of composite adherends. The strength results for each joint are presented on Table 6.1.

Table 6.1: Joint strength for each joint configuration according to the type of applied adhesive; [27]

	Joint Strength [MPa]		
Adhesive type	**Bonded**	**Bolted**	**Bonded-Bolted**
Film	453	162	440
Paste	67.1		192

It can be concluded that the film adhesive bond is stronger than the bolt role on the bonded-bolted joint. The joint strength for the simple bonded case is similar to the joint strength for the bonded-bolted case. The 3% difference between these results can be justified by the 3% reduction on bonded area for the hybrid, consequence of the hole

manufacture. The specimens with film adhesive reveals a non-increase on joint strength when a bolted connection is added since the film adhesive dominates the joint strength.

On the other hand, as the paste adhesive has lower shear strength, it represents the weaker part of the joint and when the bolted joint is added a significant improve on joint strength is noted as it could be observed with the raise on joint strength from 67.1 MPa to 192 MPa.

Concluding, the mixing of these two types of joints could be interesting if the mechanical fastening is stronger than the adhesive bonding. In this case, the bolt will act as a load carrying component after the failure of the adhesive. Inversely, if the adhesive bonding is stronger than the mechanical fastening then any or a very small joint strength improvement would be achieved.

Chan et Vedhagiri [26] performed an experimental and finite element analysis of composite bonded/bolted joints used in repairing. The aim of this study was the investigation of the stress distribution and load transfer of the bolts for 2 types of ply stacking sequence of laminate adherends. Namely bonded, bolted and bonded-bolted joints were tested recurring to samples as the one presented on Figure 6.8. The hole closer to the edge of applied load is named leading hole and the subsequent is named trailing hole.

Those authors concluded that for bonded joint the bending moment caused by the load eccentricity induces an addition of in-plane stresses and inter-laminar shear stresses on the overlap edge on the continuous part of the adherend.

For the bolted joint, the axial stress around the leading hole is higher than the stress around trailing hole and the load transfer ratio for each bolt is lay-up dependent although the variation is not too significant.

For the bonded-bolted joint, the bolts do not contribute to load carrying before adhesive failure, although their stiffness was responsible for bending moment decrease and consequently for reduction on axial stress. The results also showed that through an axial stress comparison between the 0° ply of bolted joint and bonded-bolted joint, the magni-

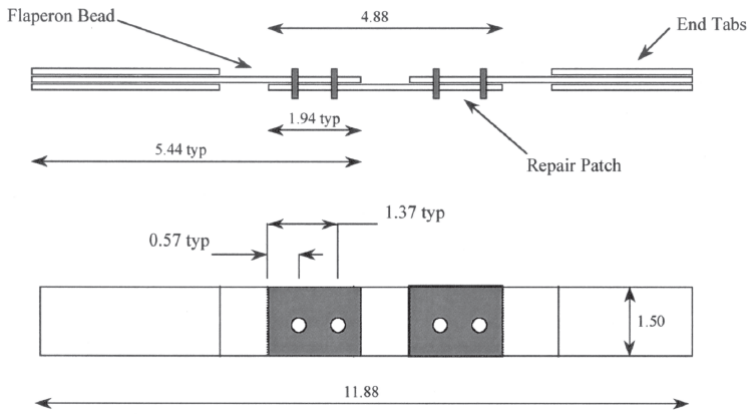

Figure 6.8: Joint geometry used by Chan et Vedhagiri [26] for the FEM analysis and experimental tests (the configuration of the bonded joint is similar to that one but without holes);

tude of axial stresses was lower in the latter case, where the compressive stresses on the bearing zone were small. These small values do not predict a laminate bearing failure.

Part II

METHODOLOGY, RESULTS AND DISCUSSION

Chapter 7

Numerical Models

The FE modelling on this work was performed according to two distinct levels of analysis and could be divided into two model categories. The overall joint design procedure suggested by Ireman [20] and illustrated on Figure 7.1 could be considered as the guideline for this work.

First of all, local models were developed and analysed (local stress analysis on Figure 7.1). After that, the fasteners used on those local models were spread along a structural application model. This last model category represents the load distribution analysis of Figure 7.1.

Local stress analysis is represented by the model of a composite single lap joint with adhesive bonding and fastened with a countersunk composite rivet. On a larger scale and representing the load distribution analysis a second model was built consisting on a wing box section with a rib-skin pair being adhesively bonded and fastened with the same countersunk composite rivet. Although the aim of the research for each model is considerably different, this guideline could be followed since it starts from a component that will be applied later on a larger scale.

All parts of both models were modelled using solid elements, since the transverse stresses are components of interest.

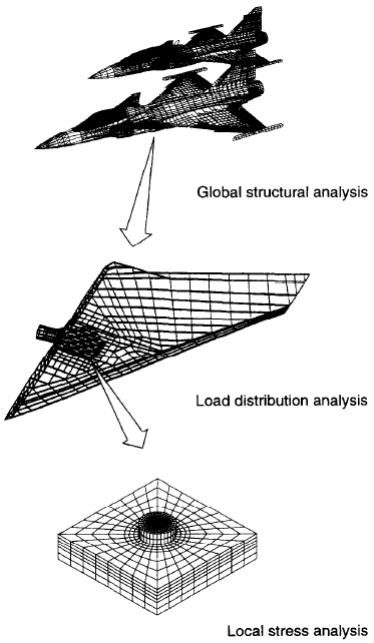

Figure 7.1: Design procedure; [20]

For modelling composite plates and the composite rivet with solid elements the *Composite lay-up* module of *Abaqus®* was used. This module allows the easy manipulation of stacking sequence, ply rotation angle, coordinate system, element relative thickness of each ply, integration points for each ply, assigned material for each ply and the region where each ply should be placed. The biggest difference of this technique comparatively to the traditional one of section and material orientation assignment is the ability to define all the required parameters on the same dialogue box for a specific part.

Solid composite layups are expected to have a single element through their thickness, and that single element contains multiple plies that are defined in the ply table. If the region where the solid composite layup is assigned contains multiple elements, each element will contain the plies defined in the ply table, and the analysis results will not be as expected. Therefore, each composite layup is assigned to cells with one element per thickness.

7.1 Analytical ABD Program

On this section is described the *Fortran* program used to calculate stresses and strains on local fibre directions for each ply of a composite laminate. This tool was provided by Dr. Guo and was helpful to validate the first FE models of composite laminates on *Abaqus ®*, specially the use of composite layup module which was a completely novelty for the author. The following sub-sections involve the description of the tasks performed by the code until the obtainance of individual stresses and strains components for each ply.

In general, that model is based on the classical lamination theory which says that,

$$\begin{Bmatrix} N \\ M \end{Bmatrix} = \begin{bmatrix} A & B \\ B & D \end{bmatrix} \begin{Bmatrix} \varepsilon^0 \\ k \end{Bmatrix} \tag{7.1}$$

[49]

where:

N is the tensor of the resultant in-plane force intensity (N/m);

M is the tensor of the resultant moment intensity (Nm/m);

A is the extensional stiffness matrix;

B is the membrane-bending coupling stiffness matrix;

D is the bending stiffness matrix;

ε^0 is the strain tensor of the reference plane;

k is the curvature tensor of the reference plane.

This program considers the laminated composite structure analysis procedure and some assumptions are described next:

- Small deformation of the plies;

- Linear elasticity theory - Hook's law is applied and modulus values are the same in tension and in compression;
- Plane stress is considered - each ply is considered to be thin-walled, therefore the analysis is performed in a 2D stress system;
- Macroscopic homogeneity - In a particular direction the properties are constant from point to point. Hence, an unidirectional lamina is orthotropic;
- For the laminate analysis it is considered thin and the bonding between plies is perfect.

The input needed for those calculations are:

- Number of laminate plies;
- In-plane young modulus for direction 1 and 2 - E_1 and E_2;
- In-plane shear modulus - G_{12};
- Poisson Ratio - υ_{12};
- Fibre orientation and thickness of each ply;
- Resultant in-plane force tensor N and the resultant moment intensity tensor M;
- Stress limits for fibre tension X_t, fibre compression X_c, matrix tension Y_t, matrix compression Y_c and shear strength S are also available for failure study.

That analytical program allows the attainment of local stresses and strains for both structure reference coordinate system and fibre direction axes.

The procedure to obtain local stresses on each ply starts on the stress analysis of the structure subjected to external loads, then on a laminate level, the force N and moment

M are worked out from the last averaged stresses and are solved in order to strains. From there, the local stress in fibre and matrix in each ply is calculated on a ply level.

The following sections describes the procedure to get the the main equation of classical lamination theory, described on equation 7.1. It is important to reinforce that the code of that program does those calculations on the opposite direction in order to get stress and strains at ply level.

7.1.1 Macromechanics of a FRP Ply

A specially orthotropic ply means that the ply axes (1,2) correspond to the reference axes of the structure (x, y) whereas a generally orthotropic ply means that the ply axes are aligned in different directions comparatively to the reference axes. Considering Hook's Law for a specially orthotropic ply the stress-strain relationship is given by [49],

$$\begin{Bmatrix} \sigma_1 \\ \sigma_2 \end{Bmatrix} = \begin{bmatrix} \frac{E_1}{1-\upsilon_{12}\upsilon_{21}} & \frac{\upsilon_{21}E_1}{1-\upsilon_{12}\upsilon_{21}} \\ \frac{\upsilon_{12}E_2}{1-\upsilon_{12}\upsilon_{21}} & \frac{E_2}{1-\upsilon_{12}\upsilon_{21}} \end{bmatrix} \begin{Bmatrix} \varepsilon_1 \\ \varepsilon_2 \end{Bmatrix} \tag{7.2}$$

$$\begin{Bmatrix} \sigma_1 \\ \sigma_2 \end{Bmatrix} = \begin{bmatrix} Q_{11} & Q_{12} \\ Q_{21} & Q_{22} \end{bmatrix} \begin{Bmatrix} \varepsilon_1 \\ \varepsilon_2 \end{Bmatrix} \tag{7.3}$$

$$\boldsymbol{\sigma} = \boldsymbol{Q}\ \boldsymbol{\varepsilon} \tag{7.4}$$

Where Q is the reduced stiffness matrix. If the ply is generally orthotropic and the stress and strain have to be presented on x, y axes, transformation matrices should be applied as follows [49],

$$\left\{\sigma_{x-y}\right\} = \left[T_\sigma\right]^{-1}\left[Q\right]\left\{\varepsilon_{1-2}\right\} = \left[T_\sigma\right]^{-1}\left[Q\right]\left[T_\varepsilon\right]\left\{\varepsilon_{x-y}\right\} = \left[\overline{Q}\right]\left\{\varepsilon_{x-y}\right\} \tag{7.5}$$

where $\left[\overline{Q}\right]$ is the transformed reduced stiffness matrix. According to that transformations and their possible manipulation, it is possible to obtain stress or strain in the desirable coordinate system.

When shear is applied that formulation takes the following form for a specially orthotropic ply [49],

$$\begin{Bmatrix}\sigma_1\\ \sigma_2\\ \sigma_{12}\end{Bmatrix} = \begin{bmatrix}Q_{11} & Q_{12} & Q_{13}\\ Q_{21} & Q_{22} & Q_{23}\\ Q_{31} & Q_{32} & Q_{33}\end{bmatrix}\begin{Bmatrix}\varepsilon_1\\ \varepsilon_2\\ \varepsilon_3\end{Bmatrix} \tag{7.6}$$

and the following form for a generally orthotropic ply,

$$\begin{Bmatrix}\sigma_1\\ \sigma_2\\ \sigma_{12}\end{Bmatrix} = \begin{bmatrix}\overline{Q_{11}} & \overline{Q_{12}} & \overline{Q_{13}}\\ \overline{Q_{21}} & \overline{Q_{22}} & \overline{Q_{23}}\\ \overline{Q_{31}} & \overline{Q_{32}} & \overline{Q_{33}}\end{bmatrix}\begin{Bmatrix}\varepsilon_1\\ \varepsilon_2\\ \varepsilon_3\end{Bmatrix} \tag{7.7}$$

7.1.2 Macromechanics of a Laminate

Moving to laminate level and considering a laminate with N plies, resultant forces and moment intensities for a certain p ply is [49],

$$(N_x)_p = \int_{z_{p-1}}^{z_p} \sigma_x\, dz; \qquad (N_y)_p = \int_{z_{p-1}}^{z_p} \sigma_y\, dz; \qquad (N_{xy})_p = \int_{z_{p-1}}^{z_p} \sigma_{xy}\, dz \tag{7.8}$$

$$(M_x)_p = -\int_{z_{p-1}}^{z_p} \sigma_x z\, dz; \qquad (M_y)_p = -\int_{z_{p-1}}^{z_p} \sigma_y z\, dz; \qquad (M_{xy})_p = -\int_{z_{p-1}}^{z_p} \sigma_{xy} z\, dz \tag{7.9}$$

The strain on each ply may vary from ply to ply depending upon z. Integrating σ from ply p to $p-1$ and substituting it in equation 7.5 , the tensor $\boldsymbol{N}$ is obtained for 1 ply and described as follows,

$$\begin{Bmatrix} N_x \\ N_y \\ N_{xy} \end{Bmatrix}_p = \int_{z_{p-1}}^{z_p} 1dz \cdot \begin{bmatrix} Q_{11} & Q_{12} & Q_{13} \\ Q_{21} & Q_{22} & Q_{23} \\ Q_{31} & Q_{32} & Q_{33} \end{bmatrix}_p \begin{Bmatrix} \varepsilon_x \\ \varepsilon_y \\ \varepsilon_{xy} \end{Bmatrix} \tag{7.10}$$

Some resultant forces can promote not only the strain of the reference plane but also the curvature of the reference plane. According to that, tensor $\boldsymbol{k}$ should be considered since,

$$\begin{Bmatrix} \varepsilon_x \\ \varepsilon_y \\ \varepsilon_{xy} \end{Bmatrix} = \begin{Bmatrix} \varepsilon_x^0 \\ \varepsilon_y^0 \\ \varepsilon_{xy}^0 \end{Bmatrix} - z \cdot \begin{Bmatrix} k_x \\ k_y \\ k_{xy} \end{Bmatrix} \tag{7.11}$$

Therefore, adding tensor N_p in all plies of the laminate from ply 1 to ply N and taken into account the contribution of tensor k, the total N of the laminate can be obtained as follows,

$$\begin{aligned} \begin{Bmatrix} N_x \\ N_y \\ N_{xy} \end{Bmatrix}_p &= \sum_{p=1}^{N} (z_p - z_{p-1}) \begin{bmatrix} Q_{11} & Q_{12} & Q_{13} \\ Q_{21} & Q_{22} & Q_{23} \\ Q_{31} & Q_{32} & Q_{33} \end{bmatrix}_p \begin{Bmatrix} \varepsilon_x^0 \\ \varepsilon_y^0 \\ \varepsilon_{xy}^0 \end{Bmatrix} \\ &+ \sum_{p=1}^{N} (-\frac{1}{2})(z_p^2 - z_{p-1}^2) \begin{bmatrix} Q_{11} & Q_{12} & Q_{13} \\ Q_{21} & Q_{22} & Q_{23} \\ Q_{31} & Q_{32} & Q_{33} \end{bmatrix}_p \begin{Bmatrix} k_x \\ k_y \\ k_{xy} \end{Bmatrix} \end{aligned} \tag{7.12}$$

The same procedure occurs for the sum of the moment intensity along the laminate,

$$\begin{Bmatrix} M_x \\ M_y \\ M_{xy} \end{Bmatrix}_p = \sum_{p=1}^{N} (z_p^2 - z_{p-1}^2) \begin{bmatrix} Q_{11} & Q_{12} & Q_{13} \\ Q_{21} & Q_{22} & Q_{23} \\ Q_{31} & Q_{32} & Q_{33} \end{bmatrix}_p \begin{Bmatrix} \varepsilon_x^0 \\ \varepsilon_y^0 \\ \varepsilon_{xy}^0 \end{Bmatrix} + \sum_{p=1}^{N} (\frac{1}{3})(z_p^3 - z_{p-1}^3) \begin{bmatrix} Q_{11} & Q_{12} & Q_{13} \\ Q_{21} & Q_{22} & Q_{23} \\ Q_{31} & Q_{32} & Q_{33} \end{bmatrix}_p \begin{Bmatrix} k_x \\ k_y \\ k_{xy} \end{Bmatrix} \tag{7.13}$$

Presenting equation 7.12 and 7.13 in a condensed form, the matrix A, B and D arises through,

$$\begin{Bmatrix} N_x \\ N_y \\ N_{xy} \end{Bmatrix} = \begin{bmatrix} A_{11} & A_{12} & A_{13} \\ A_{21} & A_{22} & A_{23} \\ A_{31} & A_{32} & A_{33} \end{bmatrix} \begin{Bmatrix} \varepsilon_x^0 \\ \varepsilon_y^0 \\ \varepsilon_{xy}^0 \end{Bmatrix} + \begin{bmatrix} B_{11} & B_{12} & B_{13} \\ B_{21} & B_{22} & B_{23} \\ B_{31} & B_{32} & B_{33} \end{bmatrix} \begin{Bmatrix} k_x \\ k_y \\ k_{xy} \end{Bmatrix} \tag{7.14}$$

$$\begin{Bmatrix} M_x \\ M_y \\ M_{xy} \end{Bmatrix} = \begin{bmatrix} B_{11} & B_{12} & B_{13} \\ B_{21} & B_{22} & B_{23} \\ B_{31} & B_{32} & B_{33} \end{bmatrix} \begin{Bmatrix} \varepsilon_x^0 \\ \varepsilon_y^0 \\ \varepsilon_{xy}^0 \end{Bmatrix} + \begin{bmatrix} D_{11} & D_{12} & D_{13} \\ D_{21} & D_{22} & D_{23} \\ D_{31} & D_{32} & D_{33} \end{bmatrix} \begin{Bmatrix} k_x \\ k_y \\ k_{xy} \end{Bmatrix} \tag{7.15}$$

And rearranging equations 7.14 and 7.15 in a matrix form,

$$\begin{Bmatrix} N_x \\ N_y \\ N_{xy} \\ M_x \\ M_y \\ M_{xy} \end{Bmatrix} = \begin{bmatrix} A_{11} & A_{12} & A_{13} & B_{11} & B_{12} & B_{13} \\ A_{21} & A_{22} & A_{23} & B_{21} & B_{22} & B_{23} \\ A_{31} & A_{32} & A_{33} & B_{31} & B_{32} & B_{33} \\ B_{11} & B_{12} & B_{13} & D_{11} & D_{12} & D_{13} \\ B_{21} & B_{22} & B_{23} & D_{21} & D_{22} & D_{23} \\ B_{31} & B_{32} & B_{33} & D_{31} & D_{32} & D_{33} \end{bmatrix} \begin{Bmatrix} \varepsilon_x^0 \\ \varepsilon_y^0 \\ \varepsilon_{xy}^0 \\ k_x \\ k_y \\ k_{xy} \end{Bmatrix} \tag{7.16}$$

Hence, through that process matrices A, B, and D are obtained and, considering all the input parameters, the tensor of extensional strain and curvature can be determined.

As it was discussed before, on analytical ABD program the procedure previously described is performed on the inverse direction, in order to determine the stresses on the reference axes for each ply. It goes from equation 7.16 towards equation 7.6 or 7.7 depending on which type of plies are being used. ABD program provides a lot of other information as the critical plies, the strains on each direction for each ply and even the equivalent elastic constants for the whole laminate.

That analysis is performed considering a infinitely long ply since the thickness of the plies is the only dimension taken into account. Somehow it is a dimensionless procedure and it could bring some issues as it is going to be presented further.

7.1.3 Normal Stress Validation

For validating the correct use of *Abaqus ®* composite lay-up module a thin 15 x 15 mm laminate plate made of 8 generally orthotropic composite plies was subjected to tension on both ends and tested on both FE software and Fortran code. However, the FE analysis does not allow the symmetrical request of a plate. Therefore, for the FE model a symmetry operation was performed. Hence, one end was subjected to a tension pressure of 10 MPa while the other end was pinned to simulate the symmetry condition. Validation was done recurring to the deformation values since they have a superior reliability comparing to

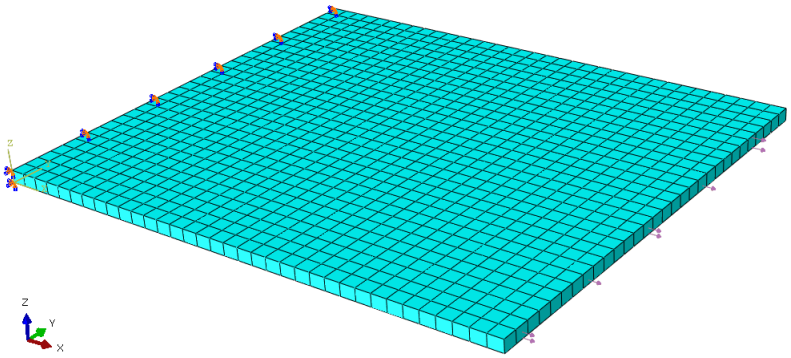

Figure 7.2: Composite laminated plate meshed on *Abaqus* ® for validation with the representation of the symmetry constraint on the left and the applied tension load on the right;

stress values. That reliability is due to the constant deformation of the laminate that generate the same theoretical deformation of each ply.

Since the thickness of each ply is 0.125 mm and the pressure applied is 10 MPa, N_x from equation 7.12 is equal to $N_x = 10 \times 10^6 \cdot 1 \times 10^{-3} = 10 \times 10^3\ N/m$, where 1×10^{-3} is the total thickness of the laminate ($8 \times 0.125 = 1$). Figure 7.2 illustrates the meshed plate on *Abaqus* ® GUI. The plate was modelled recurring to 3D stress elements, 8 node brick with reduced integration. Their designation in *Abaqus* ® is C3D8R. Orientation of each laminate's ply can be consulted on Table 7.1.

For the plate deformation analysis 5 rows of elements along the edges were removed in order to reduce the free-edge effect on those results. According to that, Table 7.1 gives the ε_x range for each ply tested with FEA software and the value for each ply obtained through the analytical ABD program. Those deformations are according to ply axes (1,2).

Regarding the deformation range obtained by FEA, top and bottom plies are the plies which deformation behaviour is closer to the analytical purpose. The author conclude that

Table 7.1: ε_x results on both *Abaqus* ® and ABD program for model validation;

Ply orientation	**ABD Program**	***Abaqus*** ® [range of values]
0 °	17.68 $\times 10^{-5}$	16.44 to 17.99 $\times 10^{-5}$
45 °	60.21 $\times 10^{-6}$	49.27 to 85.08 $\times 10^{-6}$
90 °	-56.34 $\times 10^{-6}$	-57.83 to -26.01 $\times 10^{-6}$
-45 °	60.21 $\times 10^{-6}$	49.28 to 84.52 $\times 10^{-6}$
-45 °	60.21 $\times 10^{-6}$	49.28 to 84.23 $\times 10^{-6}$
90 °	-56.34 $\times 10^{-6}$	-57.84 to 27.30 $\times 10^{-6}$
45 °	60.21 $\times 10^{-6}$	49.27 to 83.66 $\times 10^{-6}$
0 °	17.68 $\times 10^{-6}$	16.56 to 18.00 $\times 10^{-5}$

the interactivity between multi-oriented plies could lead to some deviations on expected deformations. However, since deviations are not significant and the analytical values are between the FE ranges those results were considered acceptable and consequently validated.

7.1.4 Bending Validation

For this validation procedure a 15 x 15 mm laminate subjected to bending moment in one end was used. It started from an attempt to simplify the assumption of the analytical analysis, which considers a dimensionless laminate subjected to pure bending.

The laminate was modelled with 2 plies of 1 mm thickness each oriented at 0 ° with a bending moment of 0.225 Nm applied on the right end through a force of 15 N equally distributed by 2 nodes (7.5 N). The moment intensity from equation 7.12 is on this case $M_x = \frac{0.225Nm}{0.015m} = 15\ \frac{Nm}{m}$ where 0.015 m is the width of the plate. Some points of the plate were constrained in order to ensure symmetry without compromise free deformation. Table 7.2 presents the boundary conditions of the laminate for each point. Those points

Table 7.2: Applied constraints to certain points in order to ensure symmetry of the plate;

Point	**Displacement Constraints**
P1	$x, y, z = 0$
P2	$x, y = 0$
P3, P4	$y = 0$
P5	$x, z = 0$
P6	$x = 0$

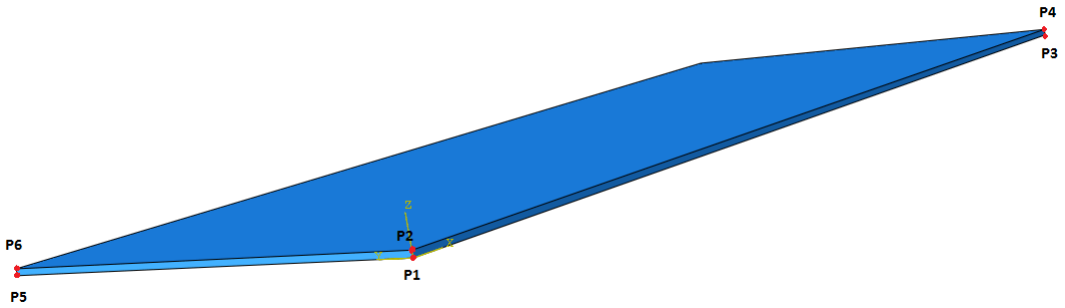

Figure 7.3: Illustration of thin laminate used for bending validation and illustration of constrained points;

can be observed on Figure 7.3. That mesh was done recurring to 3D stress 8 node brick elements with incompatible modes, since it is the recommended formulation by *Abaqus®* [45] for bending problems.

The results from *Abaqus®* showed good agreement for stress and strain in x direction as illustrated on Table 7.3, although the correspondent values on y direction were too high in comparison with the analytical ones. This comparison can also be observed on Table 7.3. According to the theory, σ_y should be 0 MPa, however the stress obtained by FEA for this direction is approximately 29 MPa. Also ε_y presents a significant difference between both methods.

Table 7.3: Collected results of ply 1 for comparison between FEA and analytical program for bending validation;

Variable	**ABD Program** [MPa]	***Abaqus*** ® [MPa]
σ_x	1125	1125
σ_y	0	28.77
ε_x	7.759×10^{-3}	7.697×10^{-3}
ε_y	-2.2483×10^{-3}	9.454×10^{-5}

This scatter occurs due to a phenomena of increased shear stresses along the width dimension and is not taken into consideration by the theoretical approach since this one uses a dimensionless analysis. As the side faces on zx plane are not y constrained, $\tau_{zx} = 0$. This value causes an unbalanced shear state stress on the xy in-plane. The shear imbalance generated on lamina's in-plane induces a growing shear force along y-direction in order to balance the misalignment in shear forces.

The high results of σ_y stresses are due to the development of those shear forces. Y-direction is coincident with the width dimension of the laminate. Figure 7.4 shows an elementary representation, with two elements - one from each ply - picked from the superior left corner of the laminate and cut in half. The blue edge where $\tau_{zx} = 0$ and the consequent linear increase of shear forces in y-direction is drawn. The external stresses applied on the diagram (σ_c and σ_t) are equivalent to the effect of the bending moment.

In order to get a full 3D elements balance of shear forces, the increase of shear stresses on the bottom ply will be in the opposite direction, like presented and obtained with FEA.

Since the analytical program deals with an infinitesimal laminate, this effect which is particularly related to the width dimension does not occur. Afterwards, the model can be validated because x stresses and strains from FEA are in good agreement with the ABD

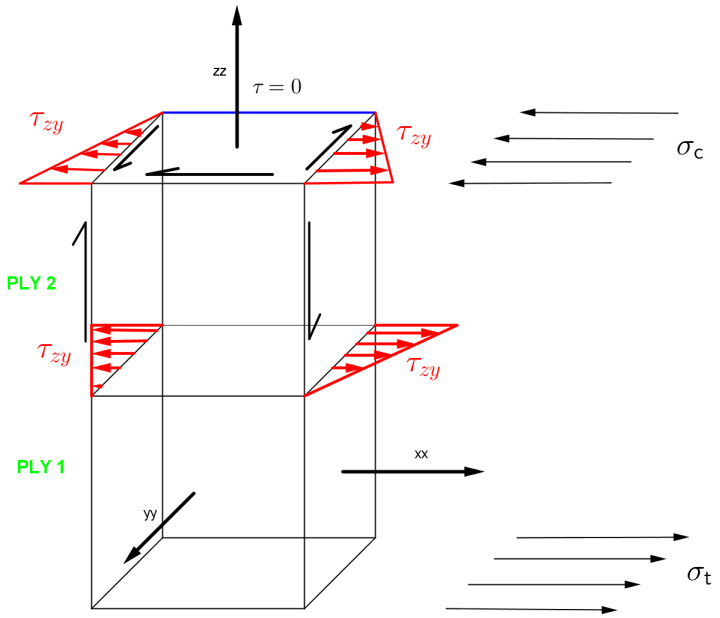

Figure 7.4: Schematic illustration of shear growth event;

code. After this conclusion about shear growth phenomena, y stresses and strains have to be considered and critically accepted.

During this validation, the same analysis was done using shell elements, to exclude the possibility of some error when using solid elements, but it gave exactly the same results. Hence, this phenomena is the most plausible reason for the high values of y stresses.

7.1.5 Cylindrical validation

Since the rivet would have a cylindrical shank made of composite laminæ, another validation was performed recurring to some approximations. The cylinder is assumed to be a flat plate made by its respective composite laminate that was rolled up until the connection of both ends. The laminate is composed by 4 plies on a symmetric disposal with a total thickness of 1 mm. Those orientations are pointed out on Table 7.4. The length of the plate is 35 mm and the width is $2\pi r$ where $r = 3mm$. Thus, a long cylinder is obtained with a tension load applied on the right extremity and a pinned constraint

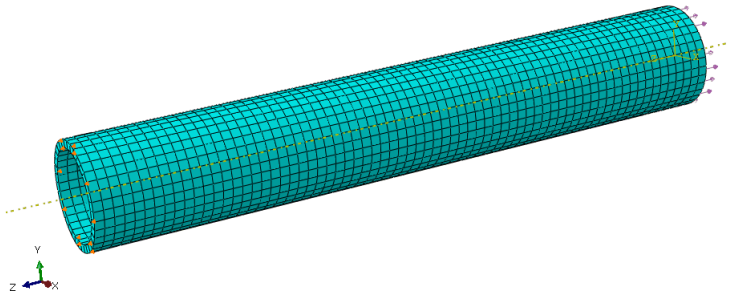

Figure 7.5: Composite laminated cylinder meshed on *Abaqus* ® for validation. Representation of pinned constraint on the left and the applied pressure load on the right;

applied on the left end. Although the cylinder concept was being modelled on FE software, a flat plate characterization was being introduced on ABD program.

According to FEA results the rolling of the laminate does not promote too much differences than a flat plate on tension. The leverage on that procedure is based on the ability to validate a different method to assign layup orientations. In that case the orientation of each ply varies spatially along the surface of the geometry since the external surface of the cylinder will be the reference surface for the normal direction of the ply axes. This method for defining variable layup orientations is known as *discrete field* and will be described further on section 7.2.1.

Figure 7.5 illustrates the meshed cylinder with applied load and constraints whereas Table 7.4 shows the conclusive comparison between strains and stresses found on each ply according to each method.

Analysing Table 7.4, although the values from both methods are not truly coincident, they are in acceptable agreement which allows the validation for that cylinder model. As it was previously discussed it is possible to model a cylinder starting from a flat plate rolled along its weak axis. The input data of ABD program was based on a tensioned flat plate while the input data of the FE software was based on a tensioned cylinder with the

Table 7.4: ε_x results on both *Abaqus* ® and ABD program for model validation;

Ply orientation	**ABD Program**	***Abaqus*** **®** [range of values]
0 °	12.43 $\times 10^{-5}$	12.08 to 12.38 $\times 10^{-5}$
45 °	77.83 $\times 10^{-7}$	65.81 to 74.99 $\times 10^{-7}$
45 °	77.83 $\times 10^{-7}$	77.97 to 81.94 $\times 10^{-7}$
0 °	12.43 $\times 10^{-5}$	12.46 to 12.58 $\times 10^{-5}$

same dimensions of that flat laminated plate.

7.2 Single Lap Joints

For this investigation 4 models of single-lap joints were developed. A single lap adhesively bonded joint, a single lap adhesively bonded joint with a countersunk hole, a single lap joint adhesively bonded and riveted with a countersunk composite rivet and a single lap joint adhesively bonded and bolted with a countersunk titanium rivet. Although the main focus of this research is the stress analysis of the bonded-bolted single lap joints, the construction of those two bonded models are only for a brief comparison purpose.

Therefore, for the bonded-bolted single lap joint models two fastening variants were studied. The aim of the first part of this research is to compare the behaviour of a composite single lap joint when the fastener is a titanium rivet or a laminated composite rivet. Hence, two models were developed where only the fasteners were replaced from one model to another.

7.2.1 Geometry

Figure 7.6 illustrates the geometry of the model of the single-lap joint with all the dimensions in *mm*. It consists of two composite plates with a countersunk hole bonded

together by an adhesive layer. Within the countersunk hole, a countersunk rivet is bonded by an adhesive film of 0.1 mm thickness. For the composite rivet model, in the core of the rivet an equivalent isotropic composite rod is placed. The titanium rivet is completely homogeneous and made by an isotropic material. Both rivets have the same geometry and dimensions.

The first concern of this model was the modelling of the countersunk composite rivet. The proposed geometry in this work is based on rolling a composite laminate. A specific stacking sequence is rolled up through the weakest axis and should be continuous along the countersunk head. Thus, the laminate rolled on the shank of the rivet should follow the shape of a countersunk head with no gaps or discontinuities among the shape's change.

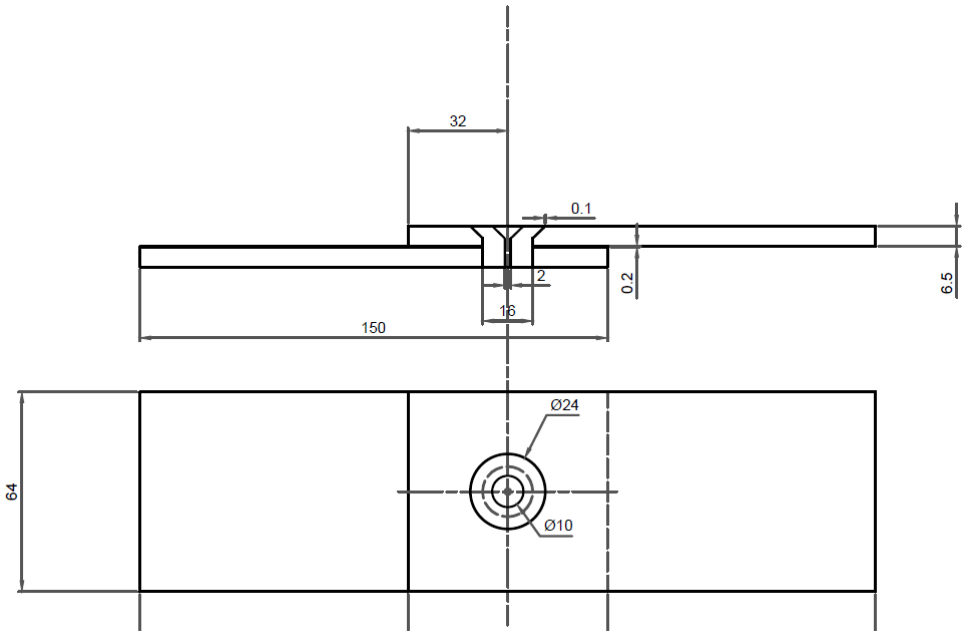

Figure 7.6: Single Lap Joint geometry and dimensions;

The intended rolling procedure should be aided with a manufacturing tool that will stay within the core after its manufacture and will be part of the rivet structure. Therefore, the isotropic equivalent composite material was chosen in order to ensure enough

stiffness for the rolling method, enough thermal conductivity during the curing process and material homogeneity to avoid galvanic corrosion, for example. That filling material sticks inside the rivet and originates a composite rod which will represent an important component for the stress analysis on further sections.

The dimension of the rivet and the thickness of the plates were the first assigned features on the joint design. According to the provided wing geometry (discussed further on section 7.3), the thickness of the skin is approximately 6,5 mm. Thus, the adherends of single lap joints should have that thickness.

Regarding the composite rivet, at the first stage it was projected according to the design rules of a metallic rivet since there are no design procedures in literature for composite rivets. Therefore, for a metallic rivet and following the recommendations of [5] its diameter should be at least 2.5 to 3 times the thickness of the thicker sheet. Hence, the diameter can be expressed as,

$$d = 2.5 \times t \tag{7.17}$$

$$d = 2.5 \times 6.5 \tag{7.18}$$

$$d = 16.25mm \tag{7.19}$$

where d is the diameter of the rivet and t is the thickness of the thicker plate.

Upon looking to some industry rivets catalogues is possible to conclude that the diameter of the manufactured rivets closest to 16.25 mm is 16 mm. However, the author

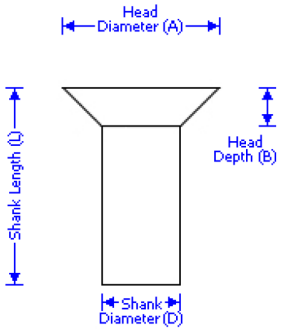

Figure 7.7: Nomenclature of rivet dimensions;

considered the countersunk head depth for this rivet too large and has reduced this dimension to half. The Sapphire company manufactures this rivet with 8 mm head depth while the author adopted a countersunk head depth of 4 mm. The reason for that is the ability of high head depths to pull-through and the requirement to avoid the knife edge effect addressed on chapter 3. According to Niu [6], the thickness of the countersunk plate should be equal to at least 1.5 times the depth of the countersunk head. This assumption was taken and the countersunk head of the fastener respects this condition ($t = 6.5mm = 1.625 \times 4mm$).

The countersunk head angle chosen was 90° since it is a medium value between the available ones: 60°, 90° and 120°. Figure 7.7 and Table 7.5 illustrates the chosen dimensions for the rivet and the Sapphire Company Catalogue [50] is available on Appendix A.

The rivet geometry is presented on Figure 7.8 a) and has all the partitions illustrated. This part was divided into 2 separately sub-parts: the bottom shank of the rivet and the countersunk head. Afterwards both sub-parts were bonded together recurring to the tie constraint option from *Abaqus®*. Either the shank or the countersunk head are internally divided into 7 rings also stacked together with tie constraints. To each pair of rings four composite plies were attached with the aid of composite layup module obtaining a total laminate composed by $7 \times 4 = 28$ plies. Figure 7.8 b) shows some random individual rings

Table 7.5: Rivet dimensions according the nomenclature of Figure 7.7;

Dimension	**Value [mm]**
D	16
A	24
B	4
L	13.2

for each sub-part of the rivet.

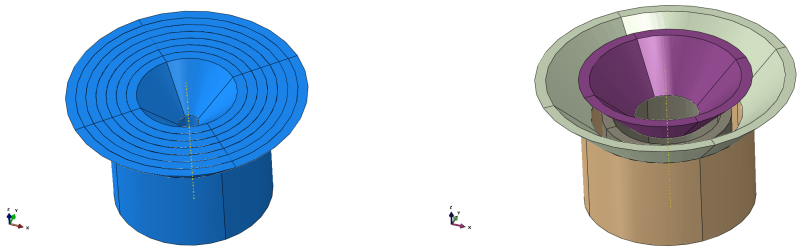

(a) Rivet geometry (b) Construction rings of the rivet

Figure 7.8: Modelled geometry of the rivet and some of the stacked rings to obtain the full geometry;

It is important to note that each of these partitions represents one element per thickness and holds four plies of composite lamina. The layup orientation is defined with the discrete field option on the composite lay-up module. The discrete field is used when the normal axis varies spatially across the layup as with curved surfaces, for example, and can be associated with specified elements or nodes. [45] The orientation on this case is defined through a normal axis and a primary axis. The normal axis is calculated upon picking an external surface and it means the z direction of the stacking sequence or the out-of-plane direction of the laminate. The surface picking operation is demonstrated on Figure 7.9. The primary axis allows the software to know from which direction should

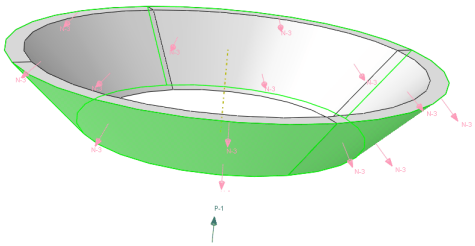

Figure 7.9: Normal and primary axis assignment;

start the ply angle orientation. The software determines the correct orientation of the fibres along the curved surfaces with the normal direction of the surface and the primary axis. For the cylinder shank layup orientation the procedure is the same as the previous one.

After the fulfilment of the composite layup editor and assigning the right layup orientations for each ply, the aspect of the composite rivet is illustrated on Figure 7.10. This figure has stress distributions because was collected after an analysis. On this figure, the first ply of each row of elements is presented. For each ply presented, 3 more plies are hidden next to it. Also the continuity of each ply through the head and bottom cylinder is notable and this illustration reminds how an experimental rivet should be manufactured.

The rod that fills the core of the rivet is made of an equivalent isotropic composite material and its shape is illustrated on Figure 7.11. This is a component of interest since the efficiency of the composite rivet would be measured further away with the aid of this rod. As it is illustrated on Figure 7.6, the lower diameter is 2 mm and the upper diameter is 10 mm.

The adherends are made of composite laminates with a thickness of 6.5 mm, a length of 150 mm and a width of 64 mm. Although the minimum values of w/d and e/d needed to achieve full strength are dependent upon the lay-up used [17], the dimensions of these plates was chosen according the recommended literature values to avoid net-section, shear-out and/or cleavage failure. Nassar and Yang [2] and Aktas and Dirikolu [51] for pinned

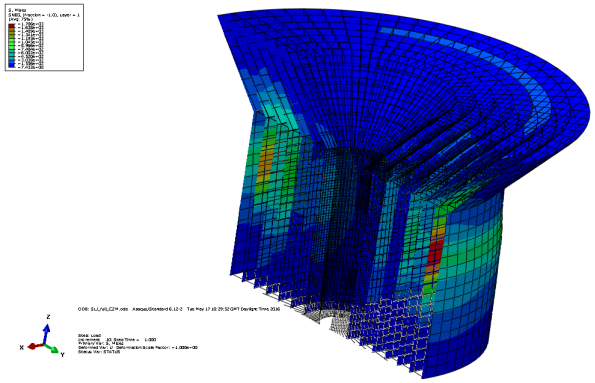

Figure 7.10: Model of the composite rivet (cut view);

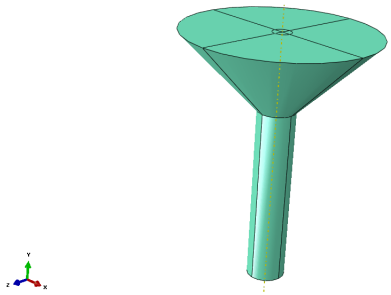

Figure 7.11: Shape of isotropic rod;

joints assumes that the ratio w/d should be higher than 4 while Yoo et al. [52] obtained bearing failure for a w/d ratio better than 3. Therefore for this joint the chosen w/d ratio was 4 giving a width value of 64 mm. For the hole to edge distance (dimension e on figure 4.3 a)) Aktas and Dirikolu [51] obtained dominant bearing failure from $e/d \geqslant 4$. However, it is important to note that those recommended values were obtained with mechanical fastening of composite joints whereas in this case it is a bonded-bolted joint composed by mechanical fastening and adhesive bonding. For that reason, the hole to edge distance was reduced to half of the recommended values since this joint is already oversized. The author believes that in this case an hole to edge distance of 32 mm is enough to avoid shear-out or cleavage failure.

The adhesive layer placed between the adherends has a thickness of 0.2 mm and was chosen according the recommended range of experimental results summarized in [3]. The increase of adhesive thickness induces a decrease on lap joint strength. The experimentally optimum range is between 0.1 - 0.2 mm. [3]

This layer of adhesive was modelled with a Cohesive Zone Model where the traction-separation law and the damage evolution criteria are similar to the ones used on [38] and [42] and will be demonstrated further.

7.2.2 Materials

The composite prepreg from the adherends and from the rivet is exactly the same and was taken from [53]. The material is a MTM46/HTS carbon fibre prepreg reinforced by an epoxy matrix resin and its in-plane mechanical properties are presented on Table 7.6.

As this investigation is performed under 3D stress analysis some properties were approximated considering the previous table like $G_{13} = G_{23} = G_{12} = 3.95$ GPa and $Z_t = Y_t = 33.9$ MPa. Also the Poisson's Ratio was considered the same for the 3 directions.

Tables 7.7 and 7.8 present the stacking sequence both for composite rivet and for composite adherends, respectively. Hart Smith [17] concluded that the highest shear-out

Table 7.6: MTM46/HTS carbon fibre and epoxy prepreg mechanical properties;

E_1 [GPa]	128.3
E_2 [GPa]	9
G_{12} [GPa]	3.95
$\upsilon_1 2$	13.2
X_t [MPa]	2278
X_c [MPa]	1352
Y_t [MPa]	33.9
Y_c [MPa]	210
S [MPa]	98.1

and bearing strengths were achieved for quasi-isotropic laminates and for that reason the stacking sequences adopted on this investigation follows this literature trend to use quasi-isotropic laminates. It should be noted that the first ply of the composite rivet is located at the outside surface and the first plies of the adherends are located at the top surfaces.

The material of the rod is an equivalent composite material for a laminate with more than 50 % of 0° plies and obtained recurring to the ABD program. The equivalent properties for this isotropic material are presented on Table 7.9.

The adhesive layer was modelled with a ductile adhesive named SikaForce 7888 used in previous investigations by Neto [38] and Campilho et al.[54] and manufactured by *Sika®*. As it was presented before, the adhesive layer was modelled recurring to a Cohesive Zone Model for further strength prediction. This numerical technique is considered a powerful tool for strength prediction of bonded joints, particularly in the cases where the ductility plays an important role on failure mechanisms. Therefore, this method uses a traction-separation law composed by a linear elastic evolution until damage initiation. Damage initiation is determined by stress criteria and is followed by an estimation of the

Table 7.7: Composite adherend's stacking sequence;

Ply	**Angle**
1	0°
2	0°
3	0°
4	0°
5	45°
6	45°
7	45°
8	90°
9	90°
10	90°
11	−45°
12	−45°
13	−45°
14	−45°
15	−45°
16	−45°
17	90°
18	90°
19	90°
20	45°
21	45°
22	45°
23	0°
24	0°
25	0°
26	0°

Table 7.8: Composite rivet's stacking sequence;

Ply	**Angle**
1	0°
2	0°
3	0°
4	0°
5	45°
6	45°
7	45°
8	45°
9	90°
10	90°
11	90°
12	90°
13	−45°
14	−45°
15	−45°
16	−45°
17	0°
18	0°
19	0°
20	0°
21	45°
22	45°
23	45°
24	45°
25	−45°
26	−45°
27	−45°
28	−45°

Table 7.9: Equivalent isotropic composite material of the rod;

Property	
E [GPa]	67
G [GPa]	25.6
υ	0.31

Table 7.10: Properties of SikaForce 7888 for CZM modelling on *Abaqus®*;

Property	
E [GPa]	1.89
G [GPa]	0.727
t_n^0 [MPa]	28.60
t_s^0 [MPa]	20.00
G_n^C [N/mm]	0.7023
G_s^C [N/mm]	8.72

crack propagation recurring to energetic data. [54] On this case, energetic data are the fracture toughness of SikaForce 7888 for the 3 fracture modes. This kind of data needs a full characterisation of the adhesive through Double Cantilever Beam (DCB) and End Notch Failure (ENF) tests. This tests are beyond the scope of this investigation, thus the properties required for the simulation were collected from [38] and presented on Table 7.10.

On this investigation, a continuum-based approach was used where the cohesive elements were used to model the finite solid thickness of the layer rather than an infinitesimal interface. The linear elastic evolution is defined by a relationship between the elastic constitutive matrix, the strains and stresses in shear and in tension. Usually, an approxima-

tion could be made for 2D models of thin adhesive layers considering $K_{nn} = E$, $K_{ss} = G$ and $K_{ns} = 0$. On this work a 3D model is being used and another approximation has to be made, considering $K_{tt} = G$ and $K_{nt} = K_{st} = 0$. Therefore, the elastic constitutive response will be described as,

$$\mathbf{t} = \begin{Bmatrix} t_n \\ t_s \\ t_t \end{Bmatrix} = \begin{bmatrix} 1.89 & 0 & 0 \\ 0 & 0.727 & 0 \\ 0 & 0 & 0.727 \end{bmatrix} \begin{Bmatrix} \varepsilon_n \\ \varepsilon_s \\ \varepsilon_t \end{Bmatrix} = \mathbf{K}\boldsymbol{\varepsilon} \tag{7.20}$$

where each parameter was already defined on equation 5.1 from chapter 5.

The selected damage initiation criterion was the quadratic nominal stress criterion available on *Abaqus®*, previously used in [38] for 2D models that combine tension and shear and described as,

$$\left\{ \frac{\langle t_n \rangle}{t_n^0} \right\}^2 + \left\{ \frac{t_s}{t_s^0} \right\}^2 + \left\{ \frac{t_t}{t_t^0} \right\}^2 = 1 \tag{7.21}$$

The $\langle\rangle$ brackets are known as *Macauly Brackets* and they mean that a purely compressive stress state does not induce damage. After damage initiation the linear softening evolution of the stiffness degradation is governed by a linear power law combining the required energies for failure in pure modes,

$$\frac{G_n}{G_n^C} + \frac{G_s}{G_s^C} + \frac{G_t}{G_t^C} = 1 \tag{7.22}$$

7.2.3 Loads and Interactions

As it was described before, the adhesive layer was modelled with a finite thickness and cohesive elements were assigned to that region. Therefore, the continuum mechanics approach considers a perfect bond between the adhesive and the adherends. Naturally, on this investigation no account for adhesion properties of the bonding interface were taken. Therefore, a tie constraint from *Abaqus®* was applied between the bottom surface of the upper composite plate and the top surface of the adhesive layer. Also the top surface of the lower composite plate and the bottom surface of the adhesive layer were similarly tied. Those surfaces are illustrated on Figure 7.12. This constraint allows to fuse together two regions even though the surface meshes of each region are dissimilar. [45]

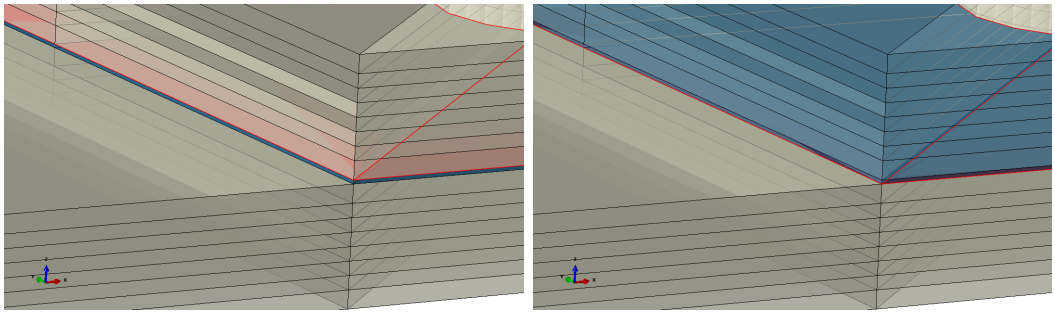

(a) Adhesive top surface (b) Adhesive bottom surface

Figure 7.12: Tie constraints surfaces between the adhesive layer and both adherends;

For most FE models, the use of a displacement control analysis reduces the solution convergence issues. Hence, on the right end section of the upper composite plate a displacement of 1,5 mm was applied on x direction, as shown on Figure 7.13. On the remaining directions, y and z the motion were constrained to provide a straight displacement of the upper plate through the x direction.

The left end section of the lower plate was pinned. That means the motion of this section was constrained in all directions. As the nodes of 3D brick elements do not have rotational degrees of freedom, for a fully constrained node the pinning procedure is

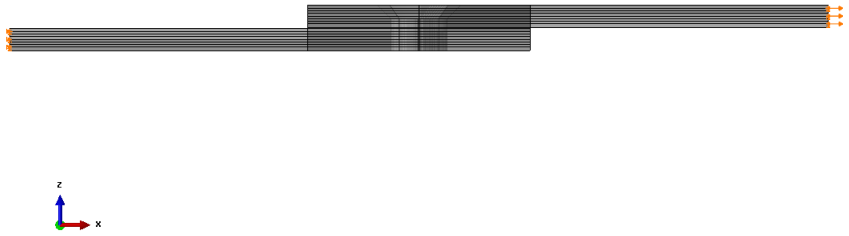

Figure 7.13: Boundary conditions of the model. At the left end section the pinned constraint and at the right end section the applied displacement of 1,5 mm on x direction and the constraints on the y and z direction;

enough, where all the translational degrees of freedom are reduced to zero. On the other hand, for the fully displacement constraint of 3D shell nodes the *Abaqus* ® encastre option is suitable since the nodes of those elements have active rotational degrees of freedom.

7.2.4 Mesh

The meshing procedure was performed with 3D brick elements for almost all of the components of the joint, excepting the adhesive layer which was modelled with cohesive elements and the isotropic rod. The 3D stress element used is an 8 node-brick with linear geometric order and reduced integration with hourglass control. The designation in *Abaqus*® is C3D8R. The cohesive element used for the adhesive layer is an 8 node with linear geometric order and in *Abaqus*® its designation is COH3D8. The other exception is the isotropic rod which was modelled with 3D tetrahedron stress elements with linear geometric order only for the attempt of saving computational efforts. *Abaqus*® designation is C3D4.

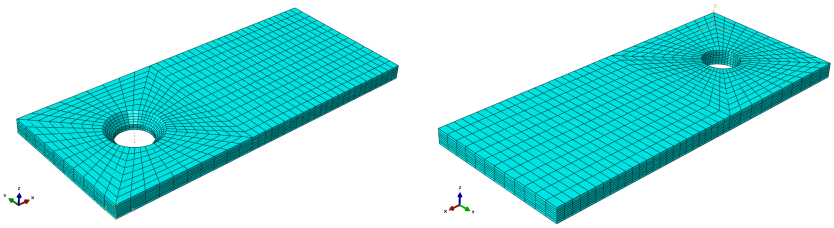

(a) Lower composite plate (b) Upper composite plate

Figure 7.14: Mesh features of the composite adherends;

The composite plates were mainly partitioned into 2 regions, the square, corresponding to the overlap area, and the remaining rectangle of the plates. The overlap area and the hole have a finer mesh with their partitions being made according some tips from [20] and [55]. The region away from the bolt hole has a coarser mesh since the most important region for analysis is located around the bolt hole. Figure 7.14 illustrates this mesh division and the difference on mesh refinement. This procedure is identical to the one followed in [20].

For meshing the composite rivet, one element per ring's thickness must be achieved, otherwise the composite layup will be duplicated if, for example, two elements are placed within the ring's thickness. Each element has a thickness of 1 mm and the mesh continuity between the head and the shank is guaranteed. The mesh stack orientation is an important step of modelling composites layups and in this case the stack orientation was assigned from the outboard of the rivet towards the centre of the rod. Therefore, the first ply of the rivet will be located at the rivet's surface and the last ply will be pasted to the rod.

One element per thickness was assigned to the adhesive layer and the highest mesh refinement was used for this component. Also the adhesive film that surrounds the rivet has one element per thickness since they are very thin layers of material. Figure 7.15 exemplifies the assigned meshes for those two components;

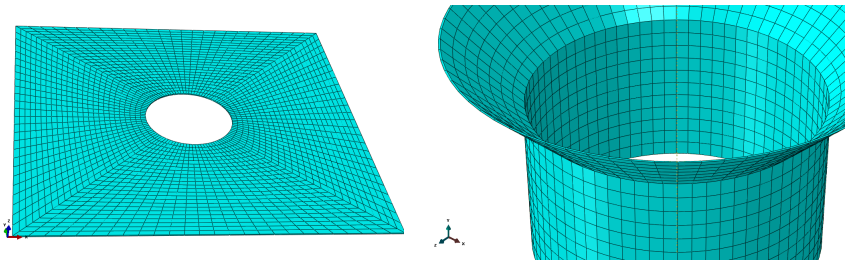

(a) Adhesive lap (b) Adhesive film

Figure 7.15: Mesh features of both adhesive layers;

7.3 Wing Box Section

The load distribution analysis illustrated on figure 7.1 was performed recurring to a joint of a wing box model. The principal joint of this structure is secured by a bonded-bolted joint. The design of the composite rivet produced before was tested on a structural joint together with an adhesively bond. However, comparatively to real wing boxes joints, the wing box joint model has suffered some approximations and/or simplifications to make the analysis feasible. Contrarily to the single lap joint model, this new model performs a large scale analysis where the interaction between rivets and the sharing of carried load is possible.

The modelling of the wing box joint was performed only with a row of fasteners to avoid stress interaction between fasteners disposed on a different level. When the bypass load reaches the second row of fasteners, the load carrying ability of the second group of fasteners would be immediately influenced by the stress level already taken by the first row. Also the pitch distance, the alignment of the fasteners and this kind of geometrical parameters could affect the analysis of the stress distribution.

Therefore, only one row of fasteners is adopted in order to simplify the problem.

For this analysis the behaviour of each rivet and load carrying ability of each rivet is studied according different levels of damage through the adhesive layer. The procedure is divided into 4 models. The difference between those models remains on the inducted

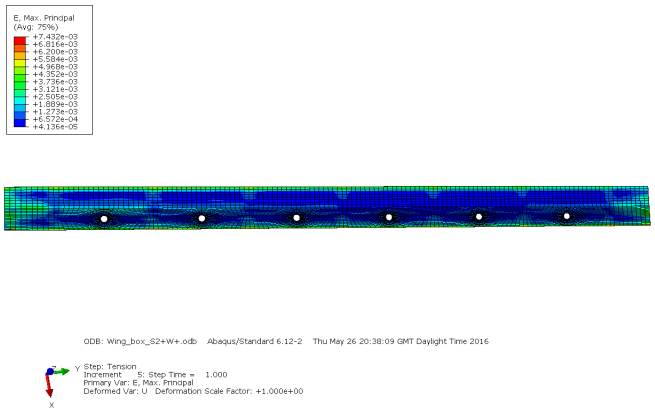

Figure 7.16: Adhesive layer with no damage; No damage model;

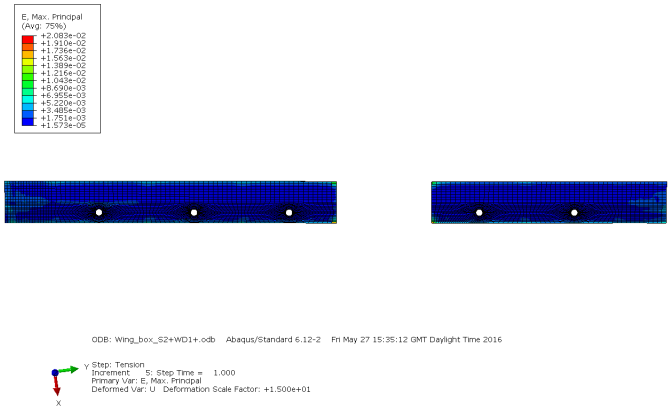

Figure 7.17: Adhesive layer with one level of damage;

damage of the adhesive layer. For simulating the damage of the adhesive layer some bonded areas were manually removed. This increased adhesive removal is illustrated on Figures 7.16, 7.17, 7.18 and 7.19.

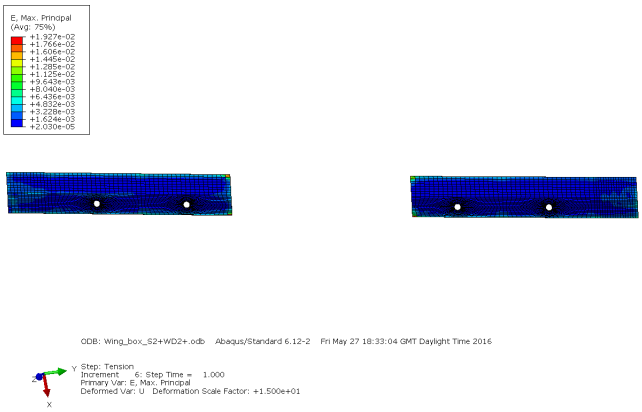

Figure 7.18: Adhesive layer with two levels of damage;

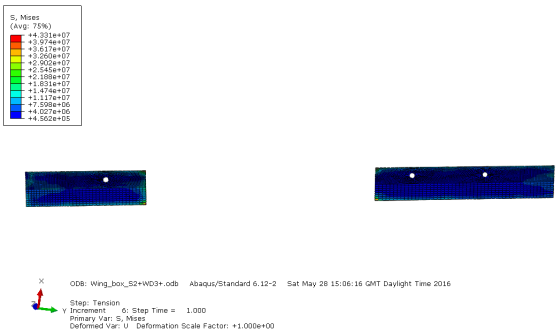

Figure 7.19: Adhesive layer with three levels of damage;

It is important to note the dissimilar way of rivet's fixture used on both cases. For single lap joint models, the rivet was bonded to the countersunk hole with a ductile adhesive whereas on this case all the rivets are fixed due to an individual bottom washer.

7.3.1 Geometry

For this procedure, a section of a wing box joint was considered and composed by 2 skins, a single I-beam rib, 14 stiffeners with a T-shape , an adhesive layer, 6 composite rivets and 6 washers. The dimensions of this structure were provided by Prof. Guo and they refer to a common commercial aircraft wing box. The geometries of these individual

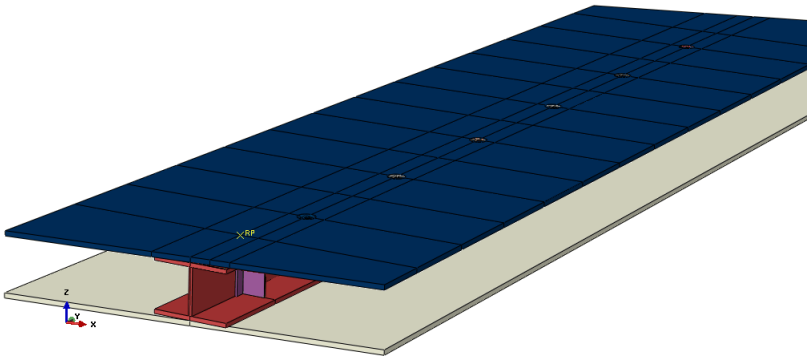

Figure 7.20: Assembly of the wing box section;

components are presented on Appendix B and Figure 7.20 illustrates the assembly of those parts.

The top skin of that structure has 6 drilled countersunk holes to hold the 6 composite rivets. Also the adhesive layer and the rib have those 6 holes but they are not countersunk holes since the heads of the rivets are housed within the top skin. Therefore, on those structures, only clearance holes were made with exact diameter of the shank of each rivet. The holes have the same dimensions than the rivet in order to ensure a perfect fit of the parts. Figure 7.21 illustrates a drilled hole where it is possible to see the top skin, the adhesive layer and the upper cap of the rib. Those rivets were placed only in one half of the adhesive width and along its length.

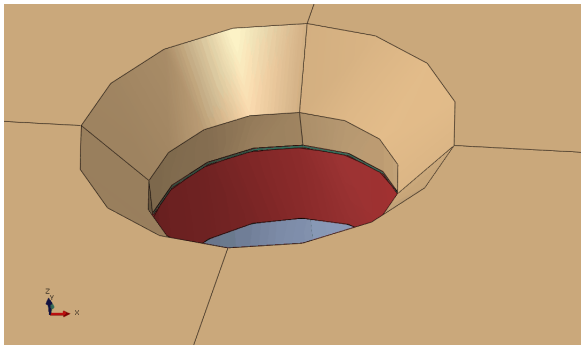

Figure 7.21: Example of a drilled hole into the structure for housing the countersunk composite rivet;

7.3.2 Materials

The material of the skins, stiffeners and the rib is aluminium since it is one of the most common used materials for this type of structures. The adhesive layer is made of ductile SikaForce 7888 and was modelled as an isotropic material. Table 7.11 and 7.12 show the material properties for the aluminium used on the metallic structures and on the adhesive layer, respectively.

The washer located on the bottom of each composite rivet to fix it to the structure is made of an equivalent composite material and its properties are previously presented on Table 7.9. The material and the laminated stacking sequence of the composite rivets are the same used on the previously local analysis. Those features can be consulted on Figures 7.7 and 7.8. Also the isotropic rod placed on the interior of the composite rivet has the same equivalent composite material as the washer, as previously used on the local

Table 7.11: Mechanical properties of aluminium;

E [GPa]	72
υ	0.27

Table 7.12: Mechanical properties of SikaForce 7888;

E [GPa]	1.89
υ	0.33

analysis with the single lap joint.

7.3.3 Loads and Interactions

The bottom skin of the structure was perfectly connected to the rib's lower surface through a tie constraint from *Abaqus ®*. The 14 stiffeners were also periodically tied to the web of the rib along the right side and the left side of it. Each pair of stiffeners on opposite sides are perfectly aligned with each other. Also the modelling of the adhesive layer is done according to the continuum mechanics approach since it considers a perfect bond between the adherends and the adhesive surfaces. Those bondings were modelled through the tie constraint option from *Abaqus ®*. The upper face of the adhesive layer was bonded to the lower surface of the top skin whereas the lower face of the adhesive layer was bonded to the upper surface of the rib.

The contact between the composite rivets and their respective holes was modelled according to a surface-to-surface contact which is based on a master-slave concept. A master surface is chosen as well as a slave surface. On this case, as the author did not know the scale of surface sliding, the finite sliding formulation was chosen. With this formulation, the possible contact between master and slave nodes is defined at the beginning of the analysis and continuously redefined along the analysis. [45] This formulation ensure a solution convergence either for small sliding or significant sliding. On this case the picked master surface was the hole surface plus the adhesive hole surface and the slave surface was the exterior surface of the rivet.

Also the contact between the washer and the lower face of the upper cap of the rib was modelled recurring to a surface-to-surface contact and the same formulation as the previous one was followed. As suggested by [45], the slave surfaces have finer meshes than the master surfaces.

The considered friction coefficient between the aluminium-composite contacting surfaces was 0.2. Blom et al [56] measured friction coefficients from the fracture surface

of ENF composite specimens where the composite plies had different interfaces. The values varied between 0.2 and 0.37 and Ireman [20] considered that the coefficient for aluminium-composite pair would be of the same order as in the fracture surface of 0 °-90 ° plies. The author considers that the coefficient for rivet-hole pair would be slightly lower, comparatively to the contact friction of the washer-rib pair, since the hole would be drilled and machined. However, for a simplifying purpose and as performed on [20] and [23], the friction coefficient of all contact surfaces was assumed to be 0.2.

Regarding the load applied to the wing box and considering the typical wing air loads exposed on chapter 2, a negative pressure was applied to the upper surface of the top skin. The top surface of the heads of the rivets were also affected by this load.

The procedure for designing an aircraft's wing box is based on the application of three stages of load. Only if the structure stands all the levels of load without fail it can be considered able to fly. For a common commercial aircraft, the typical wing load is - 7320 Pa. Therefore, based on that request three stages of load are developed from this value:

- S0 = Typical wing load;
- S1 = 2.5 × S0;
- S2 = 2.5 × 1.5 × S1.

Table 7.13: Load stages for a common commercial aircraft wing;

Stage	**Pressure [Pa]**
S0	-7320
S1	-18300
S2	-27450

All those load stages were tested through all models. However none of it was enough to overtake the stress limits of any material and therefore only the models with the S2 load

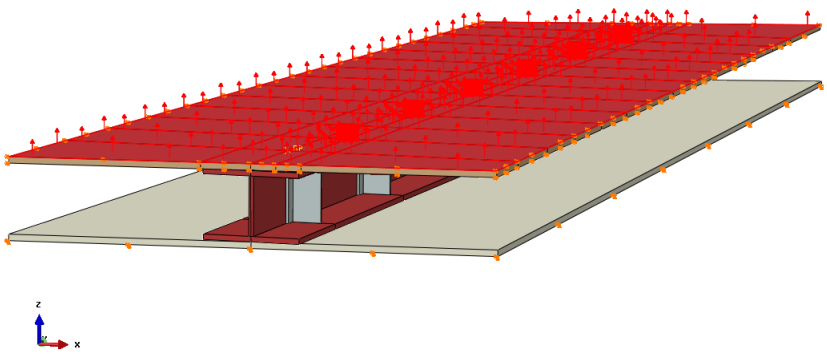

Figure 7.22: Illustration of the S2 load application region;

will be subject of analysis to avoid extensive overlap data. Hence, the stress investigation performed on chapter 8 is only based on the models with -27450 Pa applied to the top skin. The application of this load is schematically illustrated on Figure 7.22.

Boundary conditions of the wing box models were applied on the lower perimeter edges of the bottom skin and on the lateral faces of the top skin. The lower edges of the bottom skin are pinned and in those the displacements on x, y and z direction are reduced to zero. That constraint ensures the fixture of the bottom skin edges and consequently the fixture of the model. Regarding the top skin, the movement of its lateral faces are constrained through x and y directions. This last constraint was applied in order to restrict the pulling displacement of the top skin along the vertical direction. Nevertheless, although the skin will move vertically that negative pressure will promote a mixed state of pulling with bending as it could be found further on chapter 8.

7.3.4 Mesh

All parts where meshed recurring to 3D brick elements. The 3D stress element used is a 8 node-brick with linear geometric order and reduced integration with hourglass control.

In *Abaqus ®* its designation is C3D8R. The regions of the top skin and the adhesive layer closest to the rivet holes were modelled with a finer mesh than the remaining regions. Around the holes the mesh is more refined and a gradual increase of elements is obtained. Those refinements are illustrated on Figure 7.23. Since the bottom skin does not have any interest on stress analysis it has a coarser mesh and this assumption was taken for all the remaining parts that do not have an essential role on the aim of stress analysis.

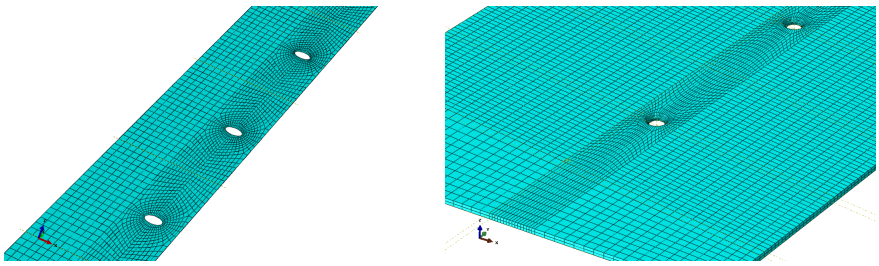

(a) Adhesive mesh (b) Top skin mesh

Figure 7.23: Mesh refinement for the adhesive layer and top skin structure;

Chapter 8

Results and stress analysis

8.1 Single-Lap Joint - Bonded-Bolted Joint

In order to simplify the language along this chapter the mentioning of bonded-bolted models would be replaced by CRM and TRM. CRM means Composite Rivet Model and refers to the model of the bonded single-lap joint fastened with a composite rivet whereas the TRM means Titanium Rivet Model and refers to the model of the bonded single-lap joint fastened with a titanium rivet. Also the names of the bonded models will be replaced by SLJ for the Single Lap Joint bonded model and SLJ+H for the Single Lap Joint bonded model with the fastener hole.

8.1.1 Load vs Displacement

Figure 8.1 illustrates the $P - \delta$ curves for all developed models - CRM, TRM, SLJ and SLJ+H. It is important to note that for all models the failure occurs for different loads. With bonded joints, the failure is traceable when a convergence issue appears after reaching the maximum load. For bonded-bolted joints, the failure/damage is investigated by the continuum mechanics approach through the strength of the composite plates and both results are limited to the point where the first overtaken stress emerges. From that

all the following results are removed and the start of failure/damage is considered to begin at that point. The damage development is not modelled, therefore any kind of delamination or damage effects within the composite plates are not subject of analysis on this work.

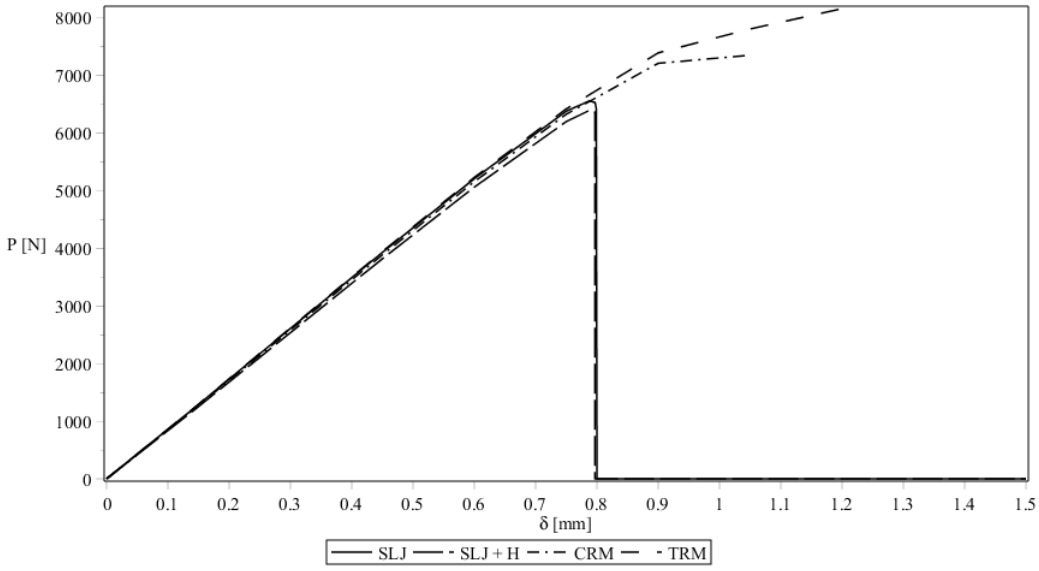

Figure 8.1: Load vs displacement curves for all models;

The shape of the CZM P vs δ curve for the SLJ model seems to be similar to the shape of the curve obtained by Campilho [54]. For both bonded joints, a linear elastic evolution is followed until the adhesive failure at the maximum load. Observing the analogous curve of the SLJ+H, there is some decrease of the load carrying ability corroborated by a small gap regarding the SLJ curve and possibly justified by the lower bonded area of the SLJ+H, since this model has a hole with the fastener diameter.

For bonded-bolted joints, the first response step follows the same linear trend of the adhesively bonded joints and the limits of those joints are pushed forward until a point where a significant change of slope occurs. From there, the carried load by the bonded-bolted joints still follow a linear evolution until a value where the stress limits of the composites plates are overwhelmed. At this point the analysis should stop.

As it can be seen, the TRM has the ability to carry more load than the CRM and moreover the failure of the TRM occurs for a later step than the failure of CRM.

8.1.2 Failure Step

The single-lap joints modelled on this work does not take into consideration composite progressive damage modelling or any kind of failure criteria implemented on the FE Analysis. However, an evaluation of the results should be performed in order to eventually detect some overtaken stresses. This analysis is based on continuum mechanics approach regarding the stress limits for each ply of the composite plates, presented on Table 7.6 from chapter 7.

8.1.2.1 Bearing Failure

Composite adherends of the single-lap joint models would be the first structures to fail. It would occur after some significant level of damage within the adhesive, and the first component of stress to overtake the stress limit is the stress on x direction. Despite the location of failure initiation be the same for both models, for the composite rivet model the failure may occur earlier than for the titanium rivet model. For the composite rivet model the failure is predicted for an applied load of 7352 N, corresponding to an applied displacement of 1.05 mm whereas for the titanium rivet model the predicted failure might happen for 8161 N, corresponding to 1.2 mm of applied displacement. Therefore, the bottom plate may fracture by tension on the region close to the beginning of the hole on the top side. The shape of the local stress distribution illustrated on Figure 8.2 suggests a bearing failure on that region, probably due to the bending displacement of the rivet and the flexibility of the overlap zone. The maximum values for each level of displacement are presented on Table 8.1 accompanied by the stress limit of the composite lamina on x direction.

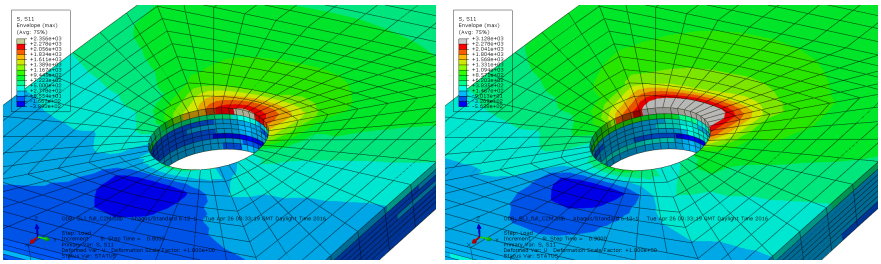

(a) CRM - 1.05 mm displacement (b) CRM - 1.2 mm displacement

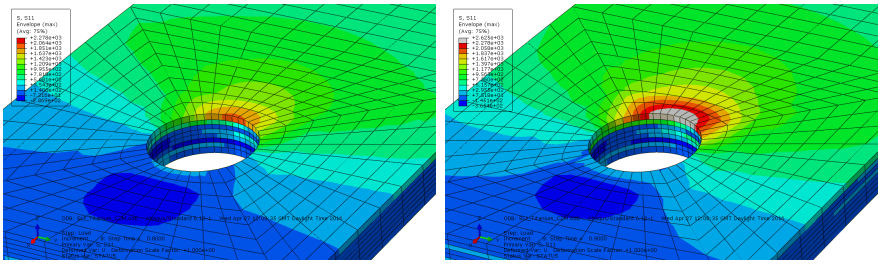

(c) TRM - 1.05 mm displacement (d) TRM - 1.2 mm displacement

Figure 8.2: σ_x distribution for different levels of displacement and for each model; Illustration of local overtaken stresses (gray regions) for x direction.

Table 8.1: Maximum σ_x for each level of displacement presented on Figure 8.2;

	σ_x [Mpa]	
	d = 1.05 mm	**d = 1.2 mm**
CRM	a) 2356	b) 3128
TRM	c) 1927	d) 2625
X_t	2278	

The analysis of these figures allows the conclusion of an earlier failure by bearing mode for the CRM.

The investigation on maximum stresses of the two bonded-bolted joints reveals that the analysis should end for different levels of load. When the author refers 'failure initiation'

it means that one of the composite stress limits was reached. The further behaviour of progressive damage and spread of delaminations throughout the plate is not considered on this work. For that case, *Abaqus ®* have a module of damage for fiber-reinforced composites based on Hashin criteria which could be used. However this module is only available for shell elements. [45]

8.1.2.2 Transverse Failure

The region of the model with the highest σ_z is located on the hole shank of the composite bottom plate, coincident with the region of maximum σ_x analysed before. This region could be checked on Figure 8.5, where a contour plot is visible through the composite bottom plate of both models. Although the values of σ_z on that region were above the stress limit, $Z_t = 33.9MPa$, failure cannot be considered, since the stress difference between consecutive plies on the bottom plate is very small. The required condition for the start of delamination is a stress difference between consecutive plies higher than the Z_t and an illustrative example is presented on Figure 8.3. For these analyses, the stresses on the composite plate of both models are illustrated on Figure 8.4 and no delamination should start. On Figure 8.6, the stress distribution along the hole deepness is plotted for both models and the discontinuity along the curves illustrates the shift from a ply to another. The path for this representation starts on the maximum σ_z on the top ply and goes straightforward until the last ply on the bottom. As it could be seen, the stress is higher on the top plies and it decreases until the less stressed plies on the bottom. A comparison between the effect of each type of rivet on σ_z through the plot from Figure 8.6 is dangerous to perform since the plotted values correspond to the carried loads at each failure step and as it was already discussed the titanium rivet model would fail for higher level of displacements. Nevertheless, for the same displacement the level of σ_z is higher for the composite rivet model.

Another critical location where delamination could eventually start is around the over-

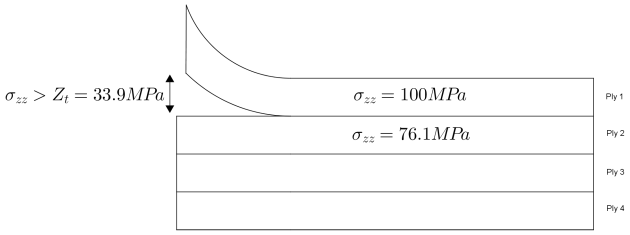

Figure 8.3: Required condition for delamination initiation;

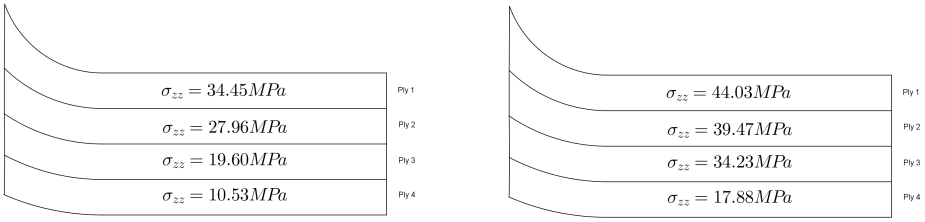

(a) CRM (b) TRM

Figure 8.4: σ_z along the most stressed plies of the composite bottom plate for each model;

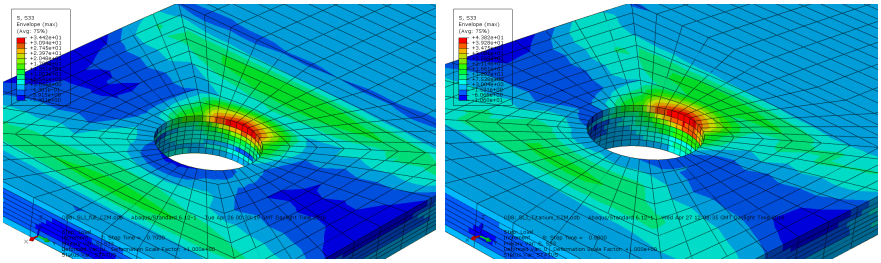

(a) Composite Rivet Model (b) Titanium Rivet Model

Figure 8.5: σ_z along the most stressed plies of the composite bottom plate for each model;

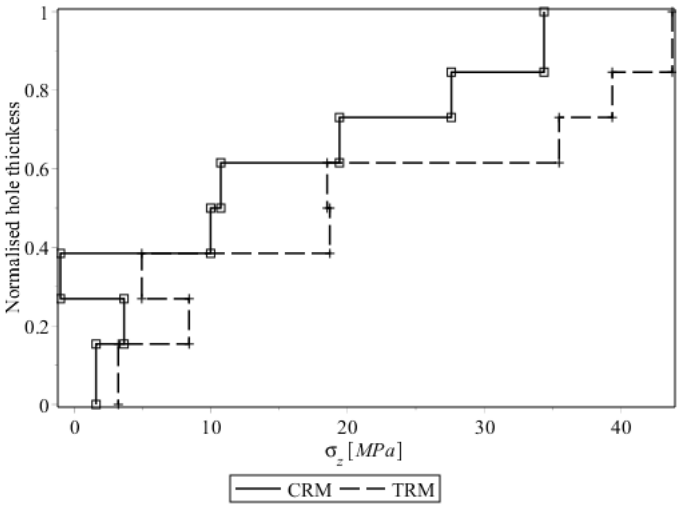

Figure 8.6: σ_z along the composite bottom plate of both models;

lap edges of bonded area due to the characteristic peeling stress of adhesively bonded joints. As the adhesive would be progressively damaged, the overlap length would progressively decrease and the maximum peel stresses would follow that trend. Therefore, as the composite bottom plate is the critical component on that joint, an analysis of the σ_z along the x direction of the plate was performed. This analysis only take into consideration the first ply because since it shares mutually the contact with the adhesive layer it would be the ply with the highest peel stresses. The chosen path is illustrated on Figure 8.7 and the σ_z distribution for different levels of applied displacement and for each model is shown on Figure 8.8 and 8.9. The displacement of 1.05 mm corresponds to the failure of the CRM and the displacement of 1.2 mm corresponds to the failure of the TRM.

The gap between the 110 mm and the 126 mm of the plate length represents the location of the hole and no stresses should be measured for that portion. An identical analysis could be made for the composite top plate, however the level of stresses are lower than the bottom case and for that reason the top σ_z distribution is not presented. The results show a gradual displacement of the peak stresses following the evolution of the adhesive damage: from the outside of the bonded area to the centre location where the

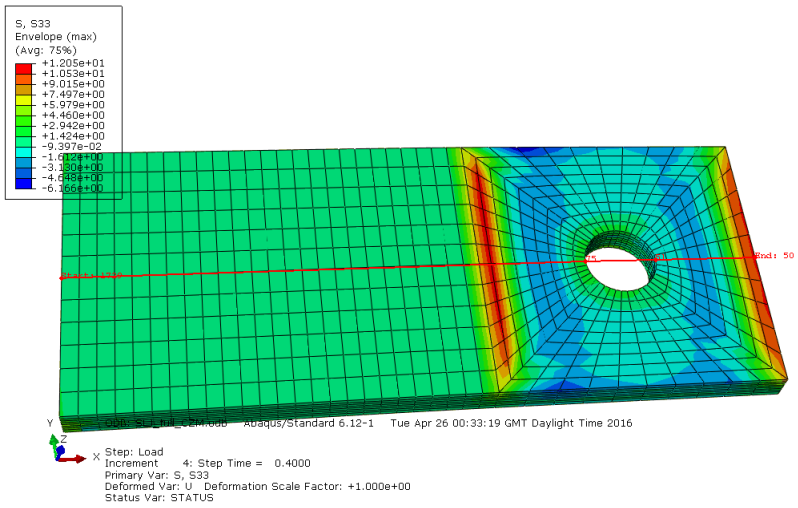

Figure 8.7: Adopted path within the first ply of the composite plate to obtain the peel stresses;

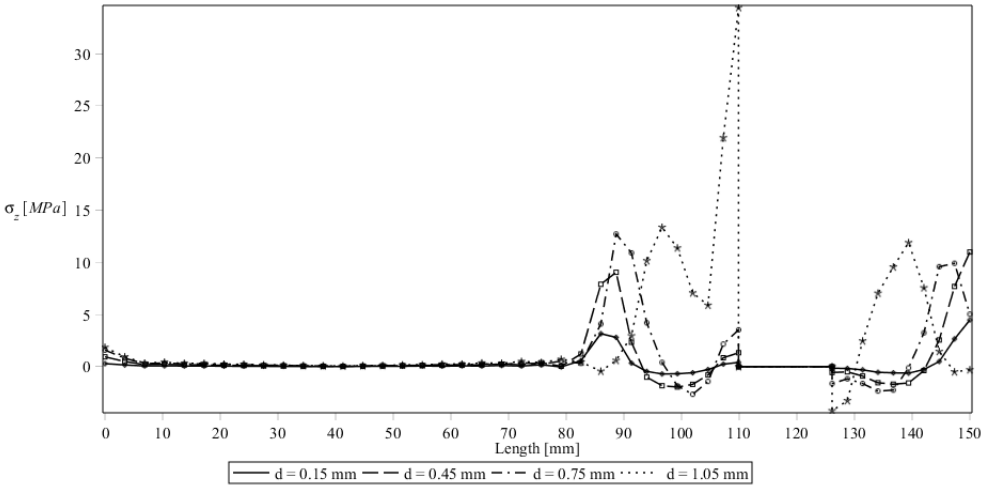

Figure 8.8: σ_z within the first ply of the composite bottom plate according to different levels of applied displacement - CRM;

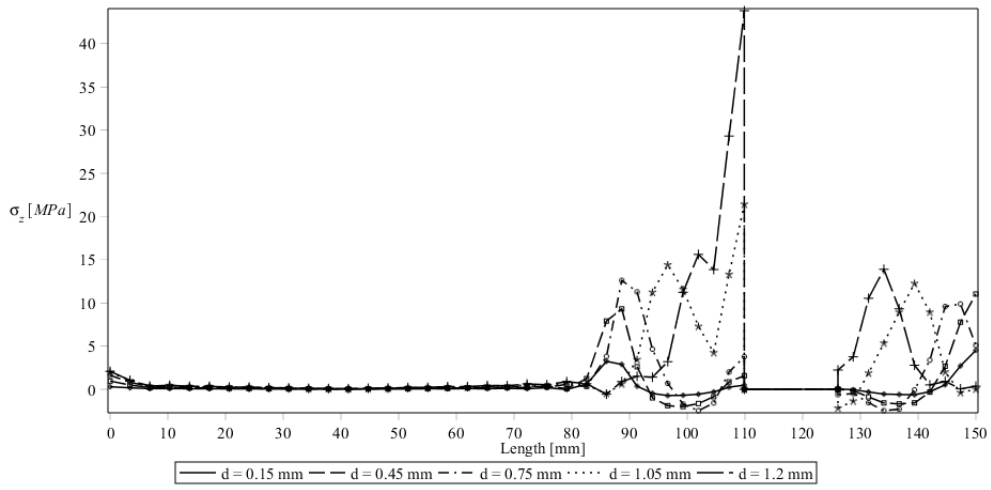

Figure 8.9: σ_z within the first ply of the composite bottom plate according to different levels of applied displacement - TRM;

rivet is placed. As it could be concluded regarding the previous plot, the levels of σ_z until the bearing failure are not enough to induce damage and start any kind of delamination. The maximum stresses are coincident with the maximum stresses for the hole thickness analysis (presented before) and located at the first ply of the plate. These peak stresses would occur for each step of failure for each model as it was expected. As it was already justified and illustrated on Figure 8.3, at this point no damage for that levels of σ_z is induced. Therefore, the stresses throughout the composite plates are not considered as potential factors of failure initiation.

8.1.3 Rivet Efficiency

The following values of stresses were obtained according to an envelope calculation. The stresses on *Composite Layups* of *Abaqus®* are calculated for each section point through the thickness of each element. With standard approach and for each ply, the field outputs are available for the bottom, top and middle section points and, as expected, this values are slightly different. Another way to analyse stresses on composite plies is requesting

an envelope for the whole lay-up. This option is widely used to investigate the critical plies of a structure [45]. On this case, the obtained stresses for each ply are subjected to some sort of criteria. The stresses are presented according to a criteria (maximum value, minimum value and maximum absolute value) within the available integration points on each ply. For this case, the used criteria was the maximum value and therefore the values presented on next tables are the maximum ones, considering the 3 integrations points for each ply.

The purpose of this analysis is based on the percentage of load transfer through each fastener. The analysis was carried picking the minimum σ_x both on composite rivet and on isotropic rod installed within the core of the rivet. These minimum stresses were obtained for each level of adhesive damage and for both CRM and TRM models. The knowledge of the amount of load that reaches the interior rod allows to understand the ability of each rivet to carry and redistribute the load. It is important to note the randomly location of the minimum σ_x during the analysis, since the increase of adhesive damage induces a random variation for the location where the minimum stress is present. However, both sides of rivet compression, illustrated on Figure 8.10, are usually the location for those compressive peak stresses. Table 8.2 and 8.3 demonstrate the minimum values of σ_x and maximum τ_{xz} according to the respective level of adhesive damage for each model.

That stress investigation consider only the minimum σ_x, since the regions in tension on Figure 8.10 should be neglected. The analysis is restricted to compressive stresses along the rivets surface. The reason for that remains on the adhesive film that bonds the rivet to the countersunk hole. As the adhesive has a low strength in tension, when the composite plate starts its displacement this adhesive would fail on an early stage, releasing the contact surface with the rivet. However, this adhesive damage evolution and failure was not numerically modelled. Those high tensile stresses seen on Figure 8.10 are the result of assumed permanent bonding of the adhesive film during the request. Therefore, those regions in real life should have very low levels of stress due to the disbond event.

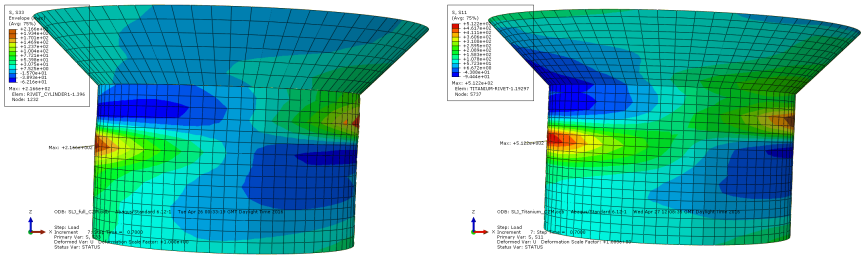

(a) CRM (b) TRM

Figure 8.10: σ_x distribution along the thickness of the rivets for both models;

Consequently, they are neglected on the following stress analysis. For that reason, only the minimum σ_x were collected since the compressive stresses are the relevant stresses for this analysis.

According to the last consideration, the maximum stresses carried by the rivets are compressive stresses, correctly illustrated on figure 8.10 through those blue contour regions. Hence, that consideration changes some content of the stress distribution but does not alter the purpose of this comparison.

After approximately 95 % of adhesive damage the composite bottom plate from CRM fails by bearing failure because $\sigma_x = 2356MPa > X_t = 2278MPa$.

After approximately 95 % of adhesive damage the composite bottom plate from TRM fails by bearing failure because $\sigma_x = 2625MPa > X_t = 2278MPa$.

The evolution of normal stresses occurs for the, approximately, same location on both models as illustrated on Figure 8.10. That figure represents the xz plane with the x direction pointing to the right. The displacement is applied on x direction through the composite top plate with the countersunk hole. The shift between tension and compression is roughly marked by the position of the adhesive layer since the composite plates load the rivets on opposite directions.

As the adhesive damage during the analysis is different for CRM and TRM, the minimum σ_x and the maximum σ_{xz} for both models is plotted in function of applied displace-

Table 8.2: Minimum σ_x and maximum τ_{xz} during the analysis along the rivet and the rod of CRM;

	Min. σ_x [Mpa]		Max. τ_{xz} [Mpa]	
Adhesive Damage	**Rivet**	**Rod**	**Rivet**	**Rod**
No Damage	-4.30	-0.86	7.011	1.878
Starting Damage	-8.70	-1.72	14.36	3.832
15 %	-13.16	-2.58	21.76	5.832
30 %	-17.59	-3.46	28.89	7.871
50 %	-21.84	-4.42	35.03	9.974
85 %	-26.02	-6.22	66.71	12.89
95 %	-62.16	-16.86	177.2	20.15

Table 8.3: Minimum σ_x and maximum τ_{xz} during the analysis along the rivet and the rod of TRM;

	Min. σ_x [Mpa]		Max. τ_{xz} [Mpa]	
Adhesive Damage	**Rivet**	**Rod**	**Rivet**	**Rod**
No Damage	2.95	1.58	7.428	1.556
Starting Damage	5.8	-0.96	15.03	3.195
15 %	7.93	-1.26	23.2	4.985
30 %	8.22	-1.79	32.84	7.114
50 %	3.387	-2.35	46.49	10.14
80 %	-16.71	-5.86	77.01	16.27
90 %	-94.4	-19.78	207.7	35.85
95 %	-238.6	-65.89	350.5	56.69

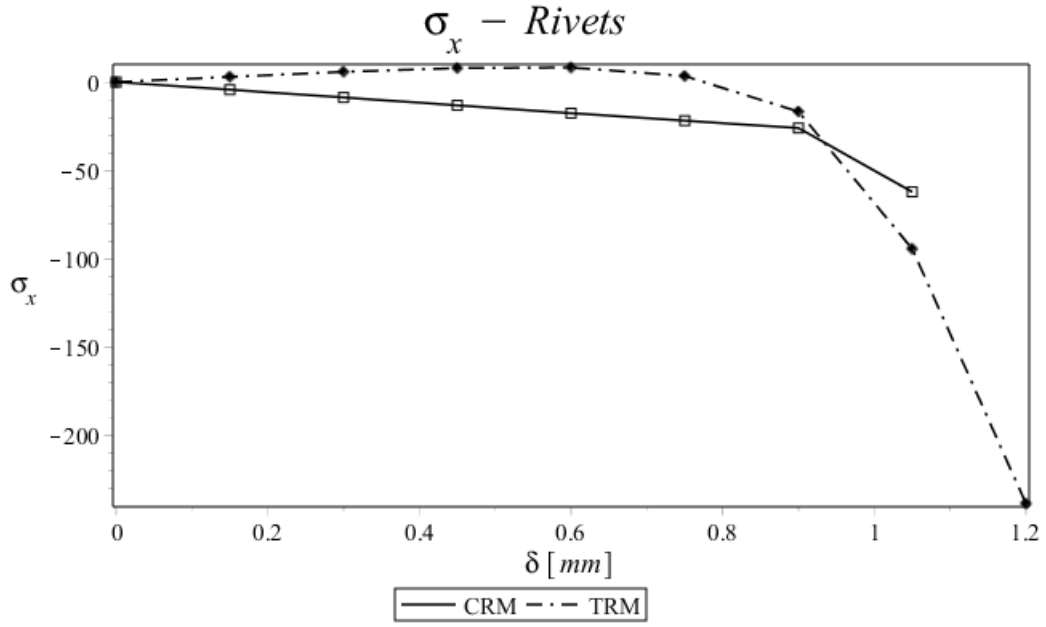

Figure 8.11: Maximum σ_x on both rivets in function of applied displacement;

ment, which represents the constant parameter for both models.

Around $\delta = 0.9$ mm from plots of Figure 8.11 to 8.14 a drastically increase in the slope of the curves is noticeable. This increase is coincident with the slope drop on the $P - \delta$ curves of bonded-bolted joints from Figure 8.1. Both models are subjected to this suddenly increase of stress and the author believes that at this point a severe adhesive damage occurs for both models. This high level of damage would transfer the role of carrying stresses to the remaining structure of the joint and specially to the respective rivets. The shear curves have an higher raise on slope than the normal curves. This fact corroborates the hypothesis of the adhesive weakening since it is the main component of the joint carrying the applied shear stresses. If the adhesive is significantly weakened then the shear stresses must be carried by other components as the rivets.

Beyond that general conception of adhesive damage, the level of induced damage is an important aspect to investigate. The higher titanium G value could be responsible for

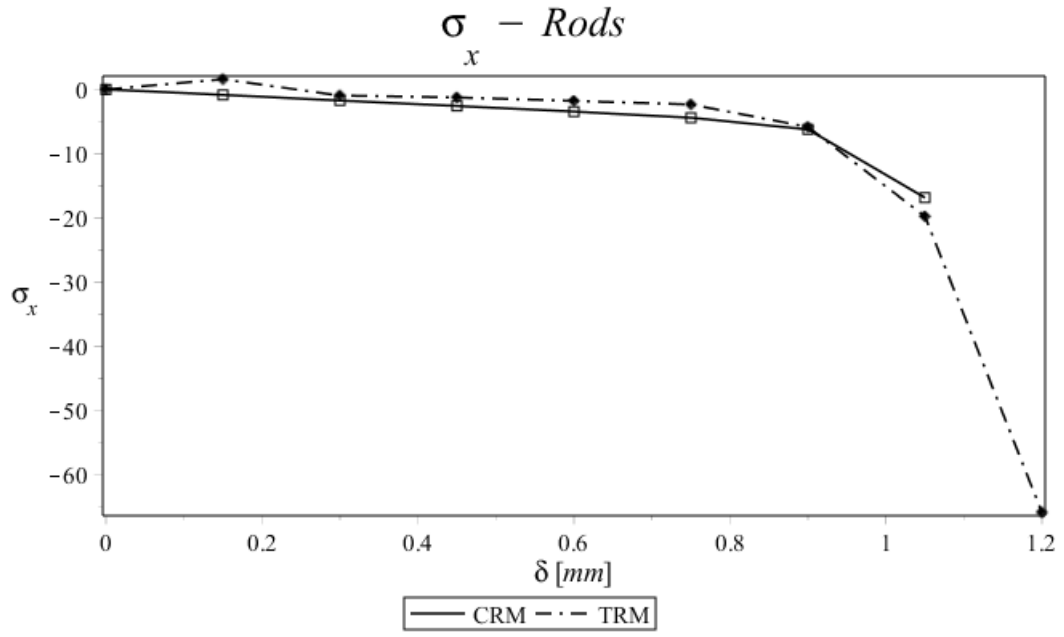

Figure 8.12: Maximum σ_x on both isotropic rods in function of applied displacement;

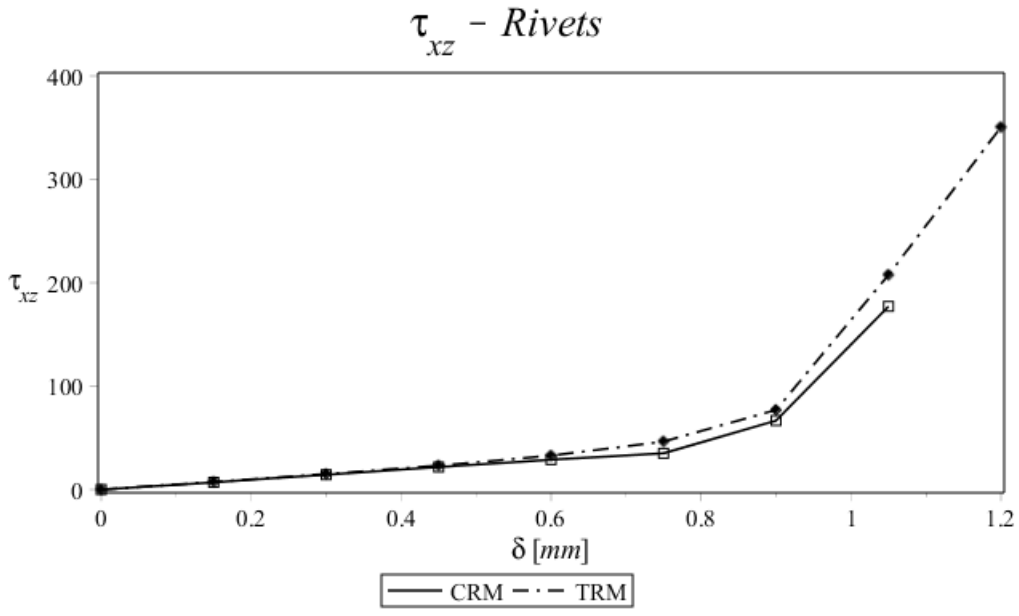

Figure 8.13: Maximum τ_{xz} on both rivets in function of applied displacement;

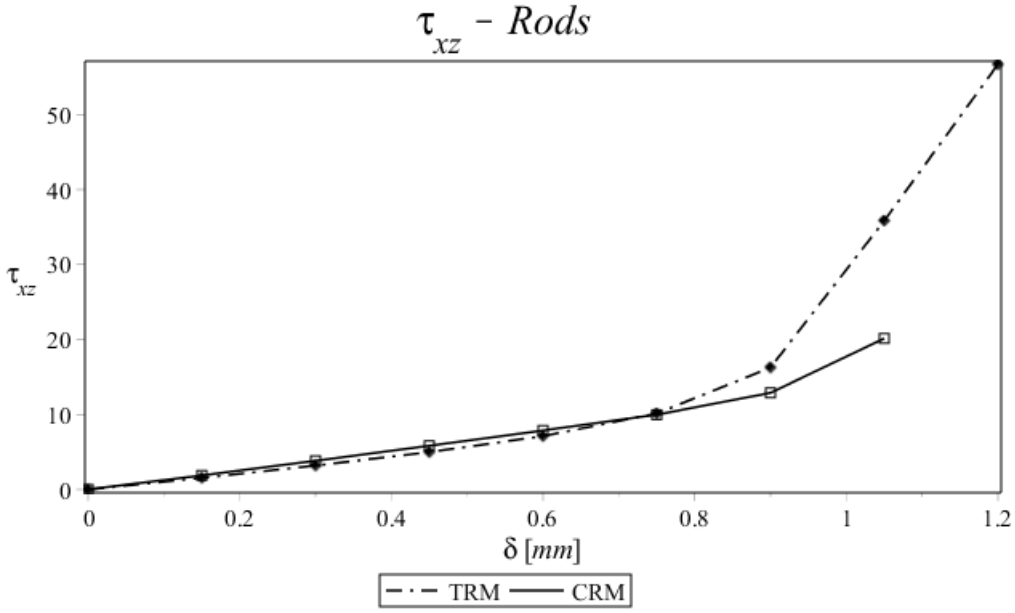

Figure 8.14: Maximum τ_{xz} on both isotropic rods in function of applied displacement;

the induction of less damage through the adhesive. On the other hand, as the composite has a low G_{xz} the adhesive layer will be subjected to more shear stresses producing an higher level of adhesive damage. Indeed, the high level of damage in the adhesive leads to a shift of stresses from the overlap to the remaining joint structure, which promotes a premature bearing failure on the hole edge of the composite bottom plate.

Comparing the maximum carried stress by each type of rivet for the last common point a comparison could be made. From this comparison the stress reduction performed by each rivet between the surface and the interior rod allows to obtain the efficiency of each solution as it is shown on table.

The levels of both type of stresses (normal and shear) within the titanium rivet are higher in comparison with the composite rivet. Analysing those stresses individually and considering a percentage of reduction between the stresses at the surface and at the rod, for normal stresses the titanium rivet still have leverage, carrying more 6.2 % of stresses than the CRM. On the other hand, in terms of shear stresses and although the level of

Table 8.4: σ_x reduction between the rivets surface and the interior rods;

	Min. σ_x [Mpa]	
	Composite Rivet	**Titanium Rivet**
Rivet	-62.16	-94.4
Rod	-16.86	-19.78
Reduction	72.9 %	79.0 %
	-6.2 % carried stresses	

Table 8.5: τ_{xz} reduction between the rivets surface and the interior rods;

	Max. τ_{xz} [Mpa]	
	Composite Rivet	**Titanium Rivet**
Rivet	177.2	207.7
Rod	20.15	35.85
Reduction	88.6 %	82.7 %
	+ 5.9 % carried stresses	

titanium is higher, the composite rivet is able to withstand +5.9 % of shear stresses.

Titanium rivet is subjected to higher values of stresses. One possible justification could be based on the higher E and G values of this material comparatively to the equivalent E_z and G_{xz} of the composite. Higher elasticity constants could lead to higher levels of withstand stresses. Nevertheless, one interesting result regards the ability of the composite rivet to withstand more specific stresses. According to the shear stress available at the rivet surface for $\delta = 1.05mm$, the composite rivet is able to redistribute more load through its plies than the titanium rivet through its homogeneous material. The author believes this phenomena does not happen for the normal stresses because the gap between E of the titanium and the equivalent E_z of the laminates is too high.

8.1.4 Adhesive Shear Stresses

The use of cohesive elements and a CZM to model the linear elastic response, the damage criteria and the damage evolution within an adhesive layer would directly affect the shear stress distribution along the analysis. The overlap edges of an adhesive single-lap joint are usually subjected to higher shear stresses according to the continuum mechanics approach. However, when damage is initiated and starts to increase, those peak stresses moves progressively from the overlap edges to the centre of the joint until final failure. This event is understandable since damage initiation occurs for the region with higher shear and peel stresses. Upon this initiation, the region is subjected to properties decreasing, and the next region would reach the required stress condition for damage initiation and so on, inducing the maximum shear stresses to travel along the overlap length towards the centre. When the fracture criteria is obtained, some elements starts to fail and no stresses are carried by this elements, reducing the overlap area and redistributing the stress along the remaining adhesive. This behaviour is corroborated by figure 8.15 for SLJ.

Appendixes C and D contain the shear stress evolution along the adhesive layer of various models. Also the distribution of the quadratic stress criterion is illustrated to

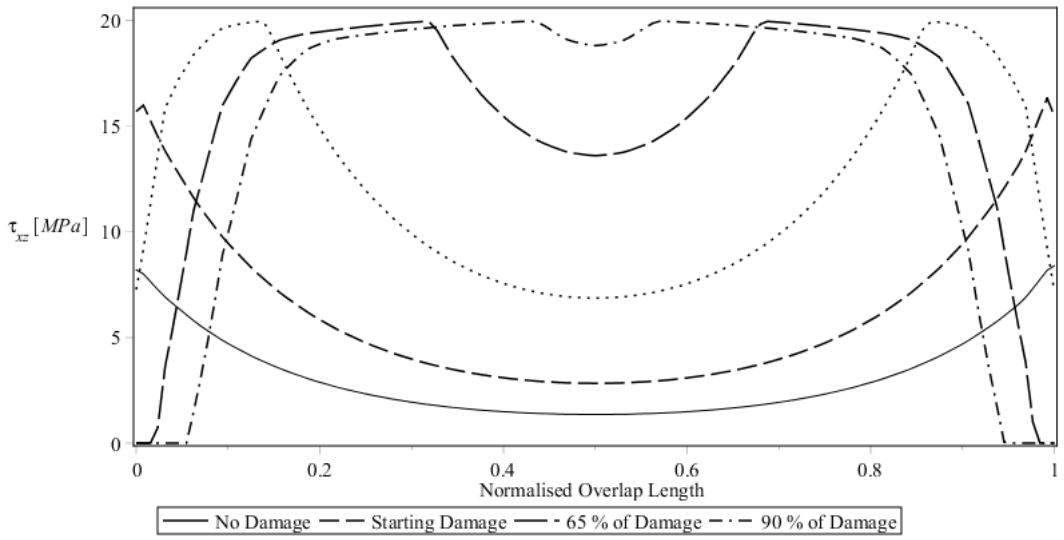

Figure 8.15: Adhesive τ_{xz} distribution for SLJ for different levels of adhesive damage;

verify the regions where the damage is being initiated.

The changing on shape of shear stress distributions is a result of the increasing of damage and failure initiation near the overlap edges. As it can be seen, before complete failure most of the stresses are being carried carried by the adhesive core.

In the case of joints with mechanical fastening, some of this stress level is transmitted and withstand by the rivet whereas the peak stresses are completely shifted from the initial overlap edges to the hole edges at the final step of the analysis. This facts are supported by the data of Figures 8.16 and 8.17. Those trends suggests that, for a certain damage level, the shear stress on the adhesive swaps to the rivet shank and keeps increasing until the failure of the adhesive. Consulting Figure 8.11 and Figure 8.1, this swap between carrying components is occurring when the applied displacement is around 0.9 mm. It is important to note that in Figure 8.16 and 8.17, for the normalised overlap length values of approximately 37 to 63 %, there is the location of the fastener hole. For that reason, between this range the curves should not be considered.

Figure 8.18 and 8.19 illustrate the shear stress development through the mid-section

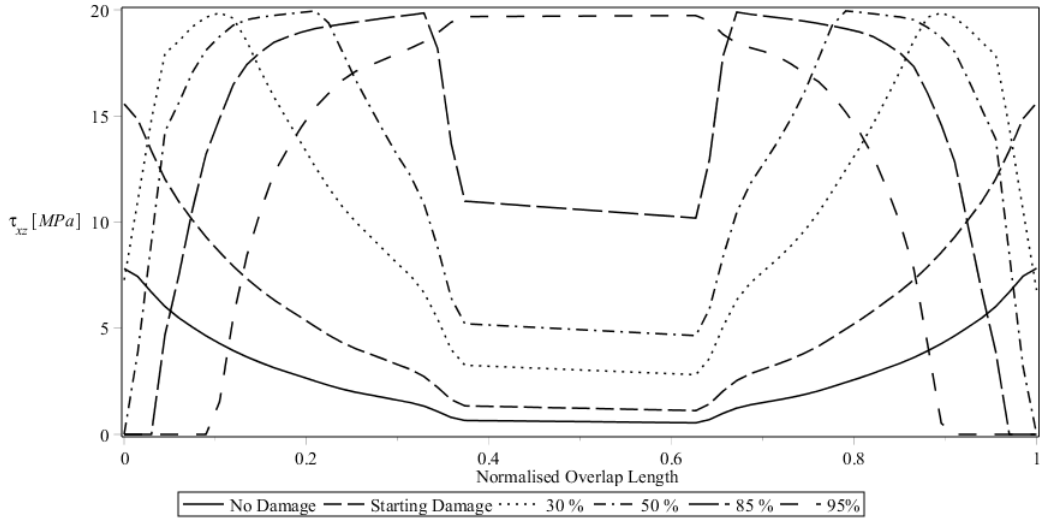

Figure 8.16: Adhesive τ_{xz} distribution for CRM for different levels of adhesive damage;

of both fastened joint models and the movement of the peak stress within it. This event is illustrated according to 3 steps of the analysis and for CRM and TRM model. Those regions are the basis of curves from Figure 8.16 and 8.17, respectively, since the adopted path is located along the mid-section of the adhesive lap.

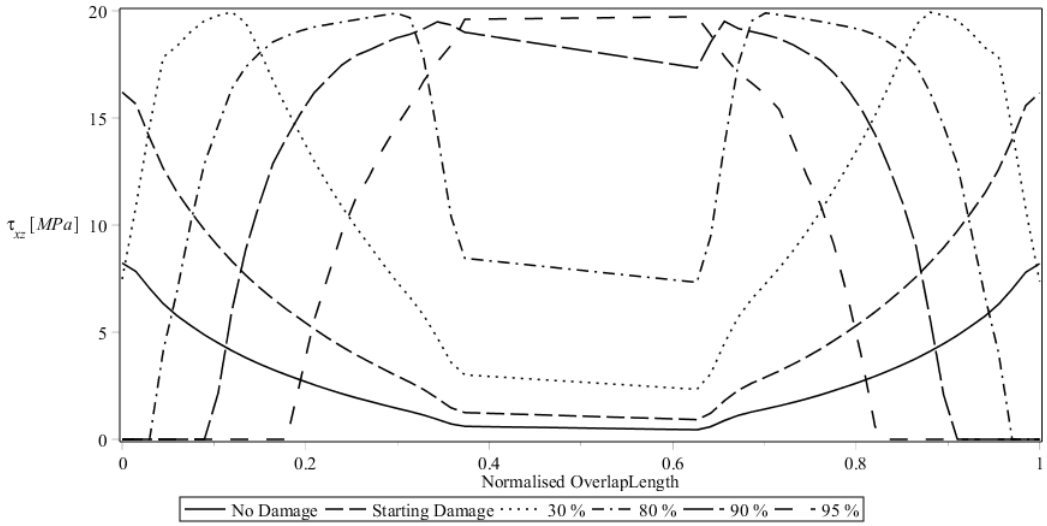

Figure 8.17: Adhesive τ_{xz} distribution for TRM for different levels of adhesive damage;

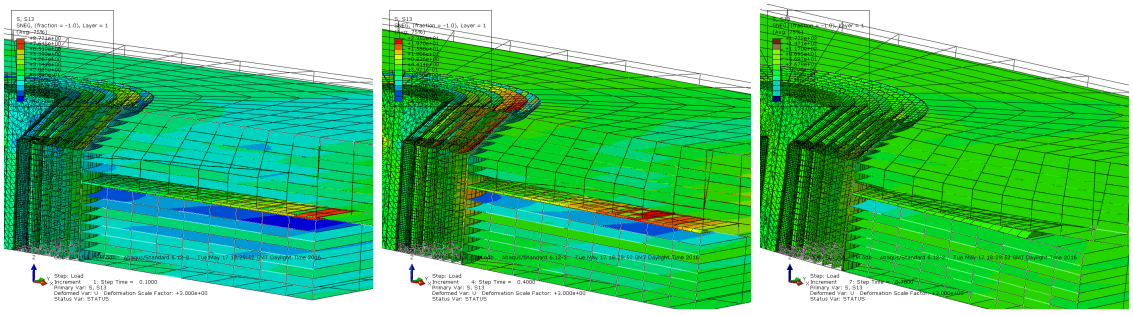

(a) 0.15 mm (b) 0.6 mm (c) 1.05 mm

Figure 8.18: Shear stress transmission of adhesive overlap from CRM for different analysis steps;

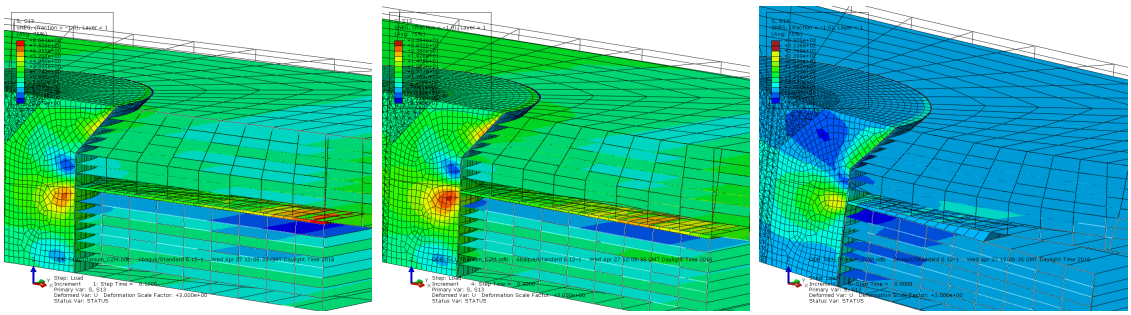

(a) 0.15 mm (b) 0.6 mm (c) 1.2 mm

Figure 8.19: Shear stress transmission of adhesive overlap from TRM for different analysis steps;

8.1.5 Conclusions

- The change of slope for both P vs δ curves around 0.9 mm of displacement illustrates the severe damage through the adhesive bonding. Thenceforth, the load starts to be carried by the mechanical fastening while the adhesive layer is been consecutively damaged and losing the ability to carry load, consequence of the continuum decreased properties. This trend keeps going until the expected failure of the joint takes place. As it could be seen, for bonded-bolted models the mechanical fastening pushes forward the failure state of the adhesive layer for higher displacements comparatively to the failure step visible on the P vs δ curves of the SLJ and the SLJ+H.

- As different materials are applied within the rivet, the level of induced damage on the adhesive is different for both cases. Therefore, for each model the scale of adhesive damage would be different since for a certain level of applied displacement the induced damage through both models is slightly different. Thus, the titanium rivet is responsible for withstanding a higher level of stress, corroborated by the load-displacement curve of Figure 8.1. The author believes that discrepancy could be justified by the higher shear modulus of the titanium comparatively to the usually

low shear modulus of the composites on the z direction.

- The bonding layer is more requested with the composite rivet and the damage is more pronounced. Indeed, the earlier failure by the CRM could be justified by the consequence of the higher shear modulus of the titanium rivet. According to that, the damage in the adhesive is lower for the TRM which allows the model to carry more load. As in the CRM the adhesive is considerably more damaged, the carried load will be lower and failure would be premature comparatively to the TRM. This is the major conclusion for the difference on the failure state between the models and could be conferred on Figure 8.2.

- Among CRM and TRM, the analysis should end for different levels of load. When the author refers 'failure initiation' it means that one of the composite stress limits was reached. The further behaviour of progressive damage and spread of delaminations throughout the plate is not considered on this work. For that case, *Abaqus ®* have a module of damage for fibre-reinforced composites based on *Hashin* criteria which could be used. However this module is only available for shell elements [45].

- Finally, the composite rivet seems to generate a smooth transition on carried load when the adhesive is severely damaged. The TRM has an identical transition although it is for higher load levels. Therefore, composite rivet is able to operate almost on the similar conditions of a joint with a titanium rivet. Even if this will be denied for safety questions, the use of a composite rivet for joint repair remains a viable option.

8.2 Wing Box Section

In order to simplify the language along this chapter the mentioning of Wing Box Section models would be replaced by WBM and WBDM. WBM means Wing Box Model

and refers to the model of the wing box section with the intact adhesive layer whereas the WBDM means Wing Box Damaged Model and refers to the model of the wing box section with damaged adhesive layer. The number after that name could be I, II and III according to the designation of the adhesive damage level.

The stress analysis were divided into two main regions: the rivets located along the joint and the adhesive layer that bonds the top skin to the rib. As the applied load of all models is a pulling pressure across the top skin, the analysis was based on pulling stresses. Also the shear stresses developed along the adhesive layer were studied. The analysis was performed for all the models addressed on chapter 7 and a respective comparison was accomplished between them to understand the role of composite rivets on the behaviour of a wing box when the adhesive damage occurs. Reminding all the models developed for this analysis and those respective levels of adhesive damage:

- WBM - No damage model;
- WBM I - Damage 1 model;
- WBM II - Damage 2 model;
- WBM III - Damage 3 model.

First of all, Figures 8.21, 8.22, 8.23 and 8.24 present an enlarged view of the structures where the adhesive disbond is placed. As it was expected, the structure behaviour is different for each case. The displacement scale factor is exaggerated to allow a good perception of the structure deformation.

Observing figure 8.20, the pulling pressure combined with the x and y constraints on the edges of the top skin result on a vertical displacement of the structure with the bending of the upper skin since the negative pressure is pushing it up while the rib stiffness produces a resistance force on the opposite direction. This event generates a combined stress state of pulling and bending.

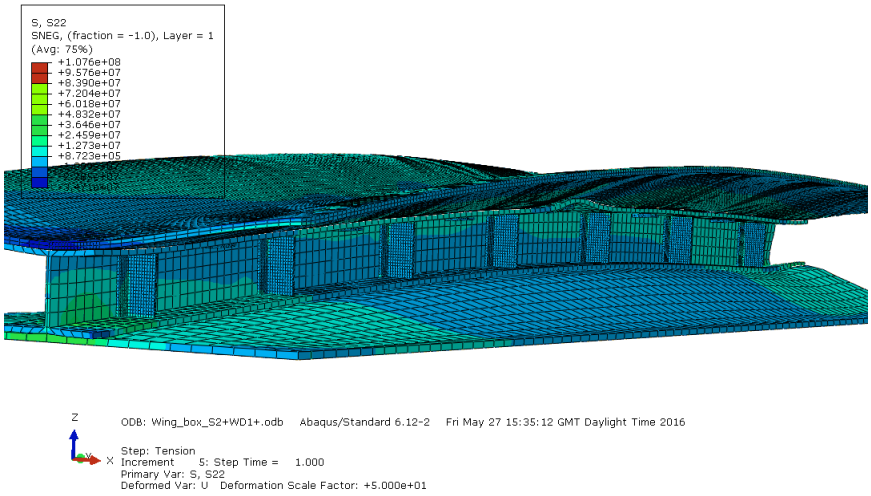

Figure 8.20: Overall structure behaviour;

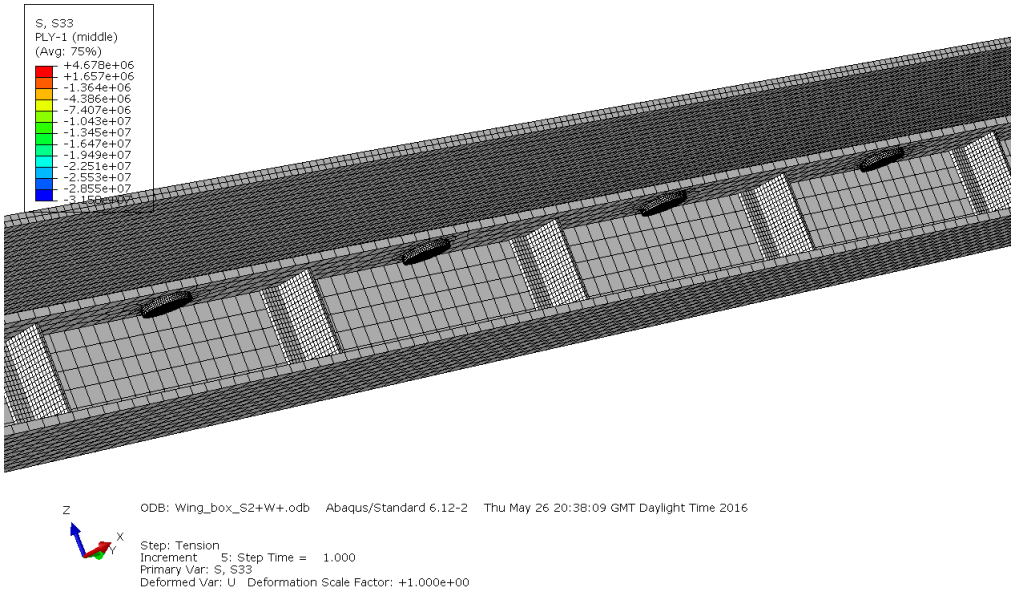

Figure 8.21: Structure behaviour for WBM;

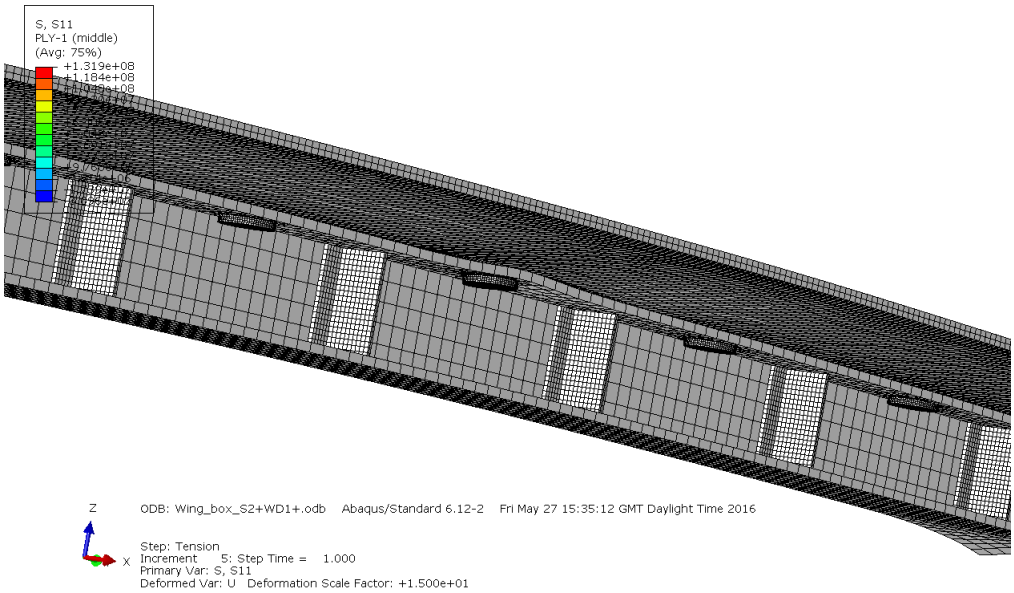

Figure 8.22: Structure behaviour for WBDM I;

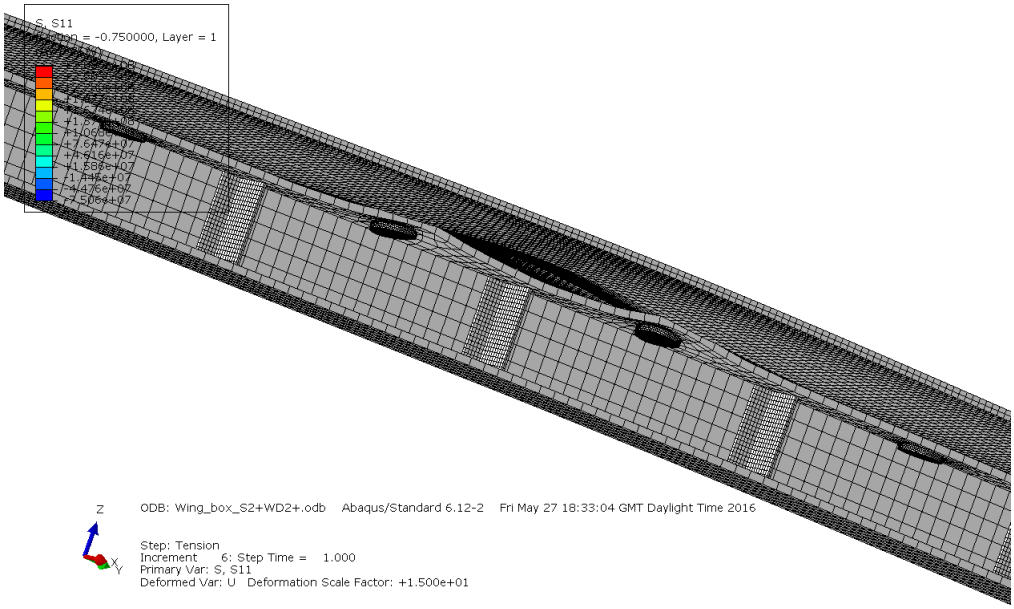

Figure 8.23: Structure behaviour for WBDM II;

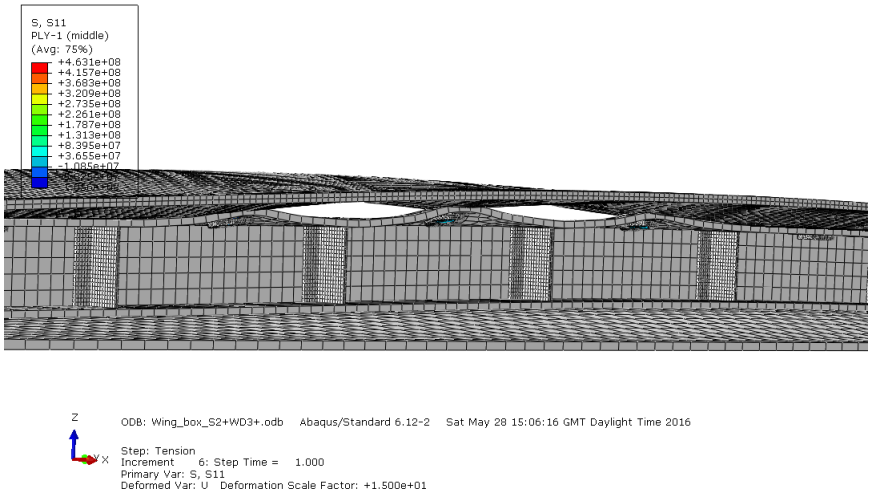

Figure 8.24: Structure behaviour for WBDM III;

8.2.1 Rivets

8.2.1.1 Pulling Stress

According to Figure 8.26, it is possible to understand the resulting pulling stress distribution within a rivet located at a damaged zone. The stress distribution of a rivet placed in a damaged region is completely different from the stress distribution of a rivet placed along the remaining adhesive layer (see Appendix E). Also the displacement of a rivet placed on those locations is considerably higher than the rivets placed along the adhesive layer.

The pulling of the top skin induces some bending that also causes the bending of the upper cap of the rib (Figure 8.25). The washer located at the bottom of the rivet aids this bending event since it forces the upper cap of the rib to push it against the lower surface of the top skin. On the damaged regions this bending of the rib causes as well the bending of the rivets (Figure 8.26). The quilled shape of the rivet's head presented on Figure 8.26 could be a consequence of the negative pressure acting on its top surface. Another likely reason could be the compressive load acting on its head by its hole surface.

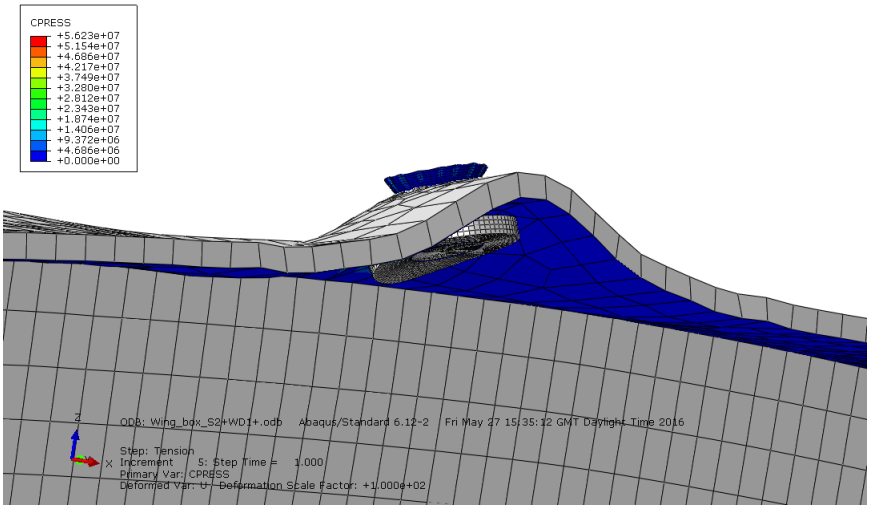

Figure 8.25: Deformation of the I-beam rib and the washer on a damaged region;

It is important to note that this shape is only visible for large deformations scale factors.

The analysis through this section and the stresses along the composite rivets were not obtained according an envelope calculation but with the middle section point of each ply. In this case, the effect of the pulling displacement of the structural components on the stress distribution of the composite rivet is a subject of interest and, therefore, the stresses were analysed on a ply-by-ply mode and displayed for the middle section point of the exterior first ply. That ply corresponds to the external surface of the rivet.

Therefore, the pulling stresses were picked for the first composite ply of each rivet and for the surface of each interior rod. The rivets were numbered to simplify the post-processing analysis. The rivets order is illustrated on Figure 8.27 and Tables 8.6, 8.7, 8.8 and 8.9 present the maximum tensile and compressive pulling stresses obtained on rivets and rod surfaces.

Table 8.10 illustrates the maximum pulling stress evolution for the rivets located close to the damage area limits. Those rivets could be also called as safe rivets since they are the first ones located after the damaged region in which the bonded-bolted joint is still intact.

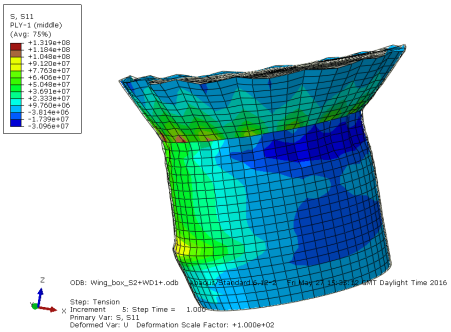

Figure 8.26: Pulling stress distribution of a rivet located on the damaged region. The deformation scale factor is very high;

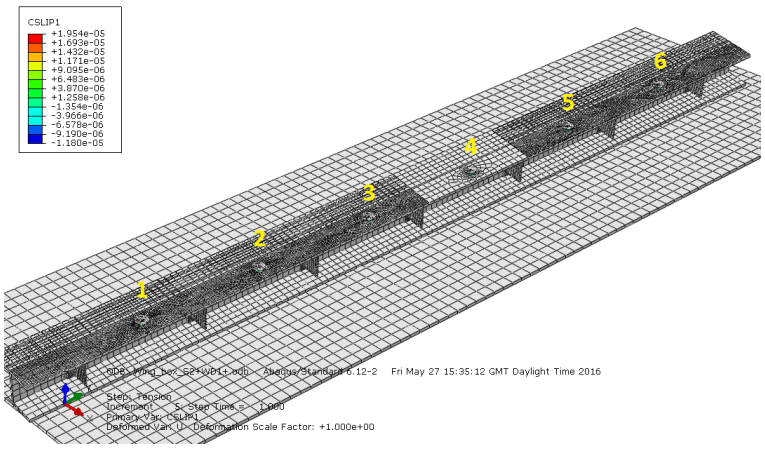

Figure 8.27: Illustration of rivets numbering. This example belongs to the WBDM I model;

Table 8.6: Maximum tensile and compressive pulling stresses acting on rivets and rods surfaces of WBM;

	NO DAMAGE - WBM [MPa]					
Rivet	***1***	***2***	***3***	***4***	***5***	***6***
Max. Rivet Surf.	123.9	120.6	119.7	119.4	120.9	120.1
Max. Rod Surf.	7.9	7.3	7.0	7.0	7.0	7.2
Min. Rivet Surf.	-16.0	-11.9	-10.8	-9.53	-10.1	-11.2
Min.Rod Surf	-0.26	-0.24	-0.23	-0.24	-0.24	-0.26

Table 8.7: Maximum tensile and compressive pulling stresses acting on rivets and rods surfaces of WBM I;

	DAMAGE 1 - WBDM I [MPa]					
Rivet	***1***	***2***	***3***	***4***	***5***	***6***
Max. Rivet Surf.	122.7	121.0	120.6	131.9	121.8	120.8
Max. Rod Surf.	8.0	7.3	7.0	6.6	6.9	7.1
Min. Rivet Surf.	-14.1	-11.9	-10.9	-31.0	-10.8	-12.1
Min.Rod Surf	-0.26	-0.24	-0.24	-2.1	-0.25	-0.27

Table 8.8: Maximum tensile and compressive pulling stresses acting on rivets and rods surfaces of WBM II;

	DAMAGE 2 - WBDM II [MPa]					
Rivet	***1***	***2***	***3***	***4***	***5***	***6***
Max. Rivet Surf.	123.3	123.2	270.9	288.6	122.9	121.3
Max. Rod Surf.	7.9	7.4	9.7	10.11	7.0	7.2
Min. Rivet Surf.	-14.0	-12.2	-72.0	-75.0	-10.0	-11.3
Min.Rod Surf	-0.26	-0.24	-8.3	-8.6	-0.25	-0.27

Table 8.9: Maximum tensile and compressive pulling stresses acting on rivets and rods surfaces of WBM III;

	DAMAGE 3 - WBDM III [MPa]					
Rivet	***1***	***2***	***3***	***4***	***5***	***6***
Max. Rivet Surf.	126.0	273.1	463.1	284.2	123.5	121.8
Max. Rod Surf.	8.1	9.6	14.5	10.2	7.0	7.3
Min. Rivet Surf.	-14.8	-69.2	-105.6	-73.7	-9.7	-11.5
Min.Rod Surf	-0.29	-8.3	-16.2	-8.4	-0.25	-0.28

Table 8.10: Maximum tensile pulling stresses acting on the surface of the rivets located closest to the edges of the damaged area (safe rivets);

	MAX. PULLING STRESS ON RIVET'S SURFACE [MPa]				
Rivet	***1***	***2***	***3***	***4***	***5***
WBM	123.9	120.6	119.7	119.4	120.9
WBDM I			120.6	DAMAGE	121.8
WBDM II		123.2	DAMAGE	DAMAGE	122.9
WBDM III	126.0	DAMAGE	DAMAGE	DAMAGE	123.5

Comparatively to the pulling values of WBM, all the remaining models have a small increase on their pulling stress of safe rivets. This comparison should be made between the first rivets after the damage on all damage models and the equivalent rivet on WBM case. For example the maximum pulling stress of rivet 2 on WBDM II should be compared to the maximum pulling stress of rivet 2 on WBM. After reading Table 8.10, it is clear that those rivets are contributing to withstand the increase on pulling level induced by the increase of adhesive damage. Although each rivet's stress gap is small it keeps giving a reasonable trend: as the damage increases the more requested rivets are.

The plots from Figures 8.28 to 8.31 illustrate the variation of the maximum tensile and compressive pulling stresses on the rivets and rods surface for each level of damage. The general trend of these results reveals that the highest absolute stresses are located on the rivets where the surrounding areas do not have adhesive bonding. Also the highest stress increases as the damage level increases. Those plots are the graphical representation of Tables 8.6, 8.7, 8.8 and 8.9.

Analysing those 4 plots, the increase of stress on the rivets placed along the damaged areas is noticeable. Peak stresses are highest for the rivets located at the centre of the

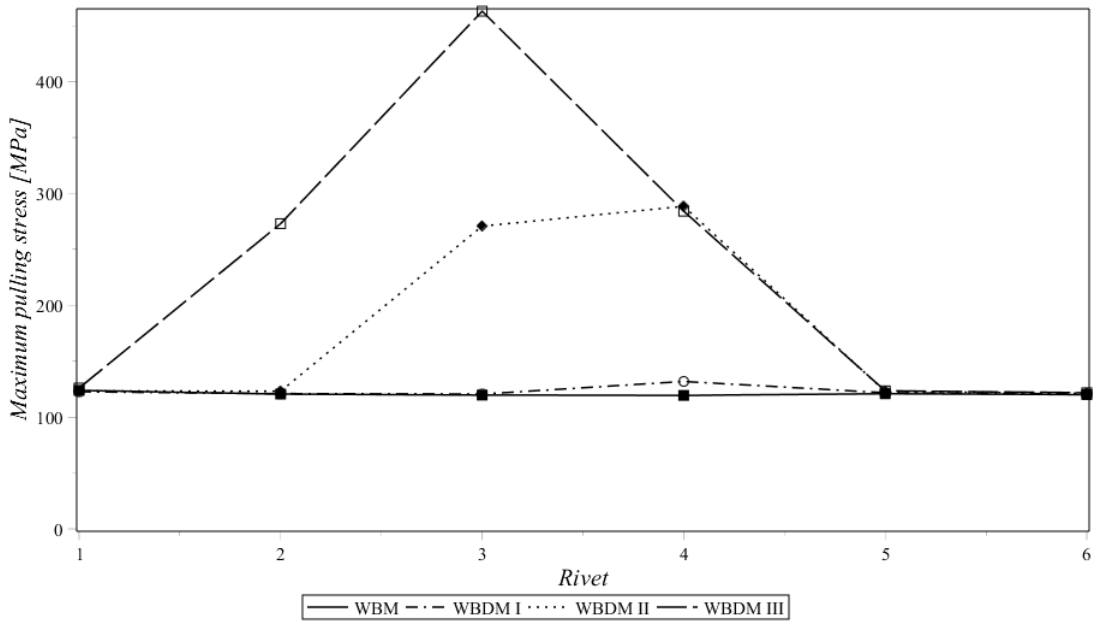

Figure 8.28: Maximum tensile pulling stress on rivets surface for each level of adhesive damage;

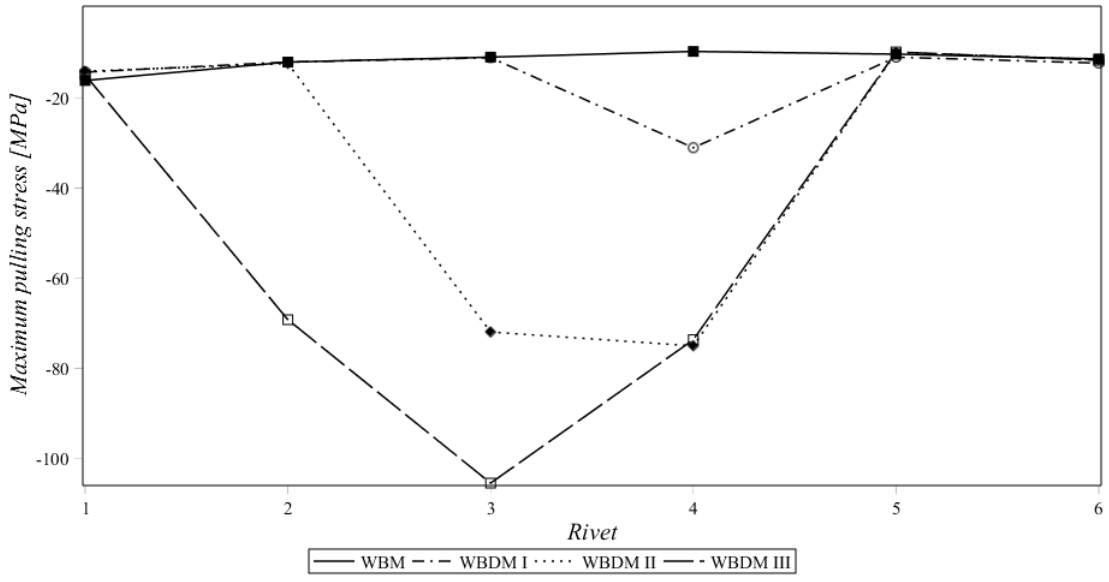

Figure 8.29: Maximum compressive pulling stress on rivets surface for each level of adhesive damage;

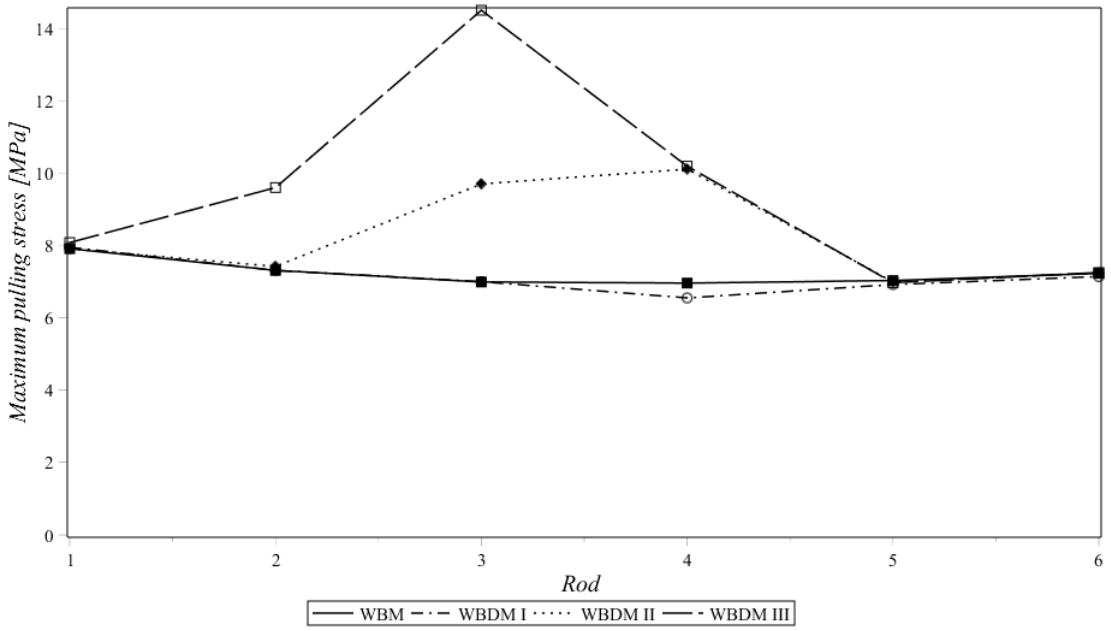

Figure 8.30: Maximum tensile pulling stress on rods surface for each level of adhesive damage;

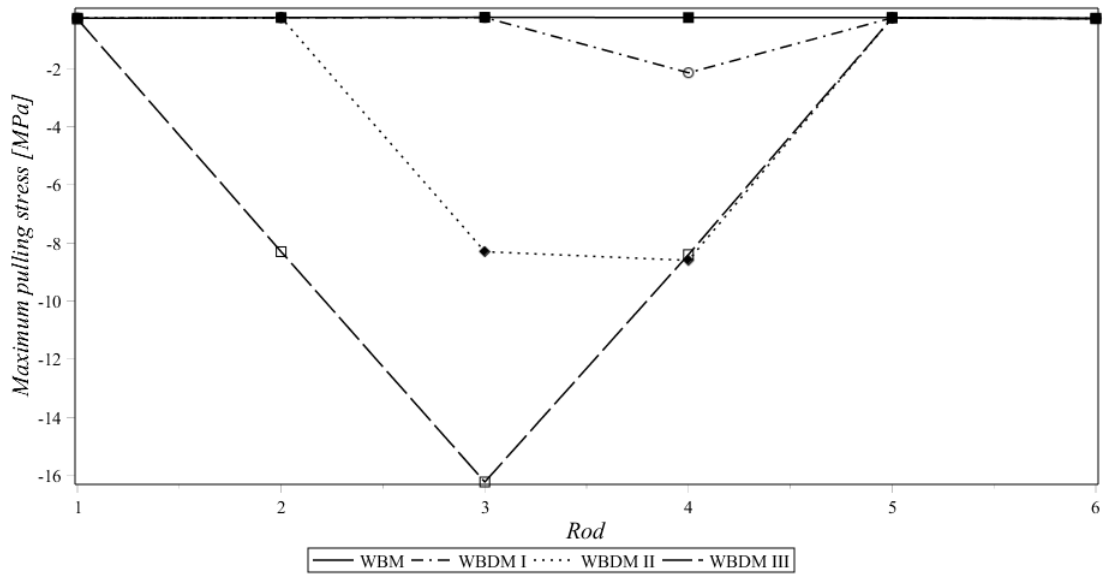

Figure 8.31: Maximum compressive pulling stress on rods surface for each level of adhesive damage;

disbonded zones and lower at the safe regions, where the bonded-bolted joint is still intact.

Hence, the conclusion is that rivets located on regions where the adhesive fails will be essential for withstanding pulling stress comparatively to adhesively bonded joints. The amount of stress to which those rivets are subjected is extremely higher than the level of tension for what an adhesive could bear. According to these results a wing box joint with only adhesive bonding will not be able to withstand this kind of pulling stresses. For this application, the use of rivets in order to ensure damage tolerance and prevent the failure of the wing box is vital.

On the other hand the rivets placed nearly to the damage limits, also known as the beginning of safe region are also of major importance. With the increase of damage, the maximum pulling stress of those rivets are increasing comparatively to the non-damaged case. This raise allows to conclude that when the adhesive damage starts the rivets close to the damage limits will be able to carry some of the stress and probably hold on the damage propagation.

The illustrations available on Appendix E show the stress distribution on each rivet's and rod's surface for each level of damage. The normal direction to the sheet plane is the axial direction of the I-beam rib, therefore the bending of the top skin occurs mainly on the right side of each rivet representation.

8.2.2 Adhesive Layer

8.2.2.1 Pulling Stress

The pulling stress distribution of the adhesive layer also varies according to the induced level of damage. The adopted path to collect the stress distribution is presented on Figure 8.32. The plots from Figure 8.33 to 8.36 illustrate the pulling stress distribution for each damage level.

The periodic drops along the pulling stress distribution means that a rivet is placed on this location whereas the peaks for each level means that the limits of the disbond

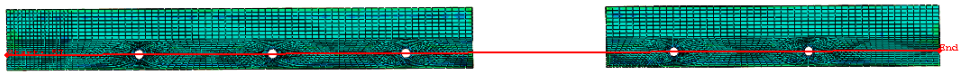

Figure 8.32: Adopted path to collect the pulling stresses along the adhesive layers for each damage level;

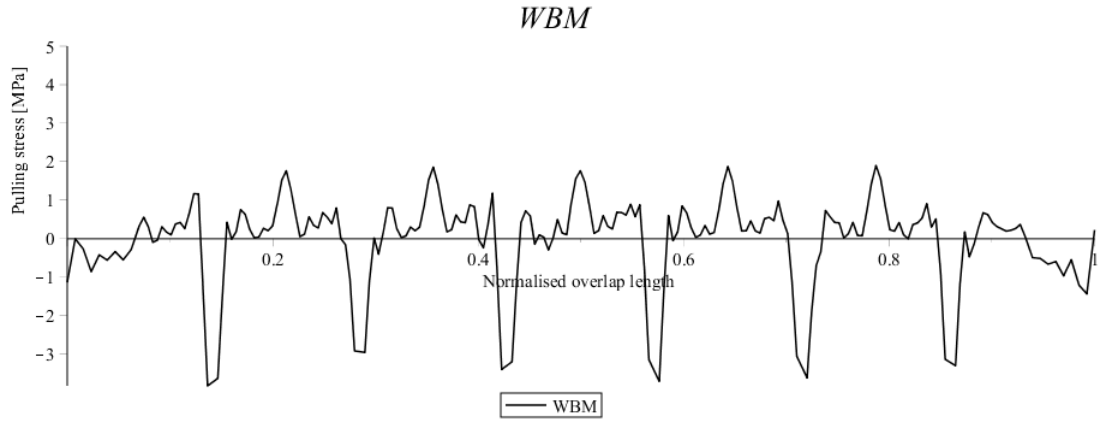

Figure 8.33: Adhesive pulling stress distribution;

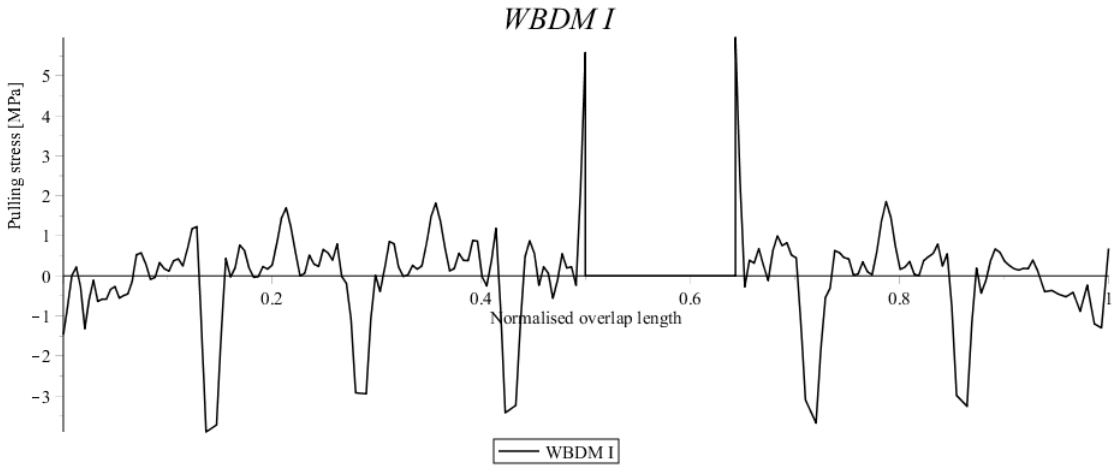

Figure 8.34: Adhesive pulling stress distribution for damage level 1;

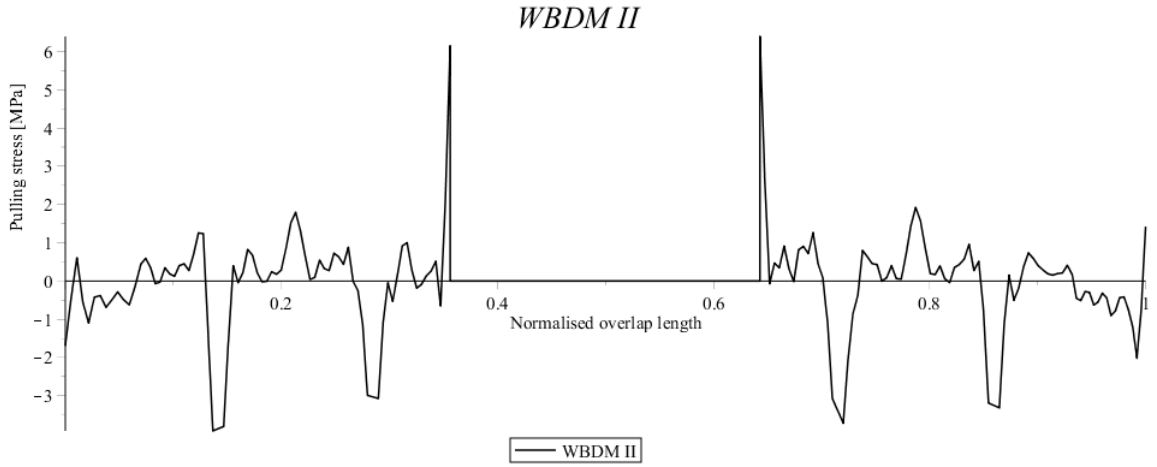

Figure 8.35: Adhesive pulling stress distribution for damage level 2;

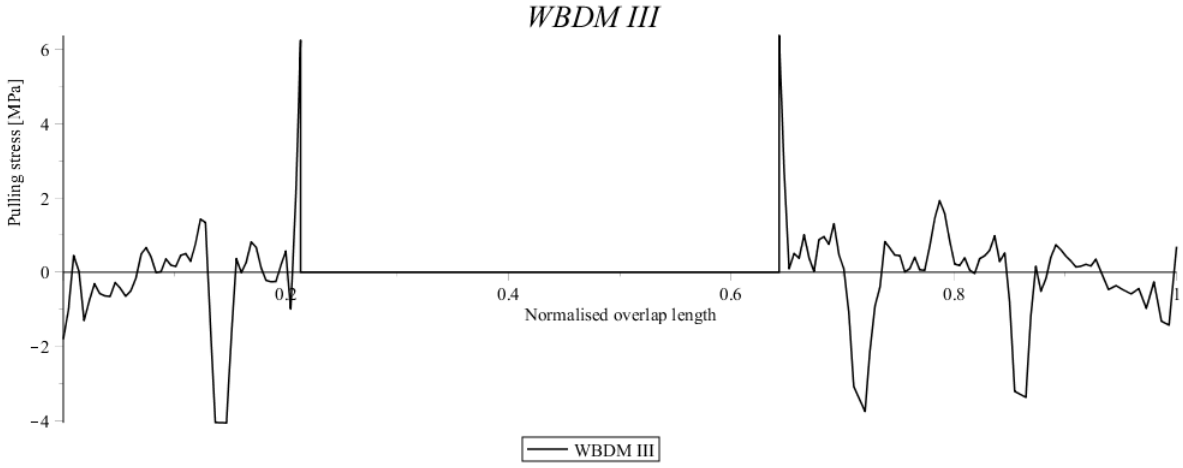

Figure 8.36: Adhesive pulling stress distribution for damage level 3;

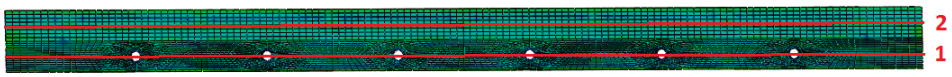

Figure 8.37: Adopted paths to collect the pulling stresses along the adhesive layer;

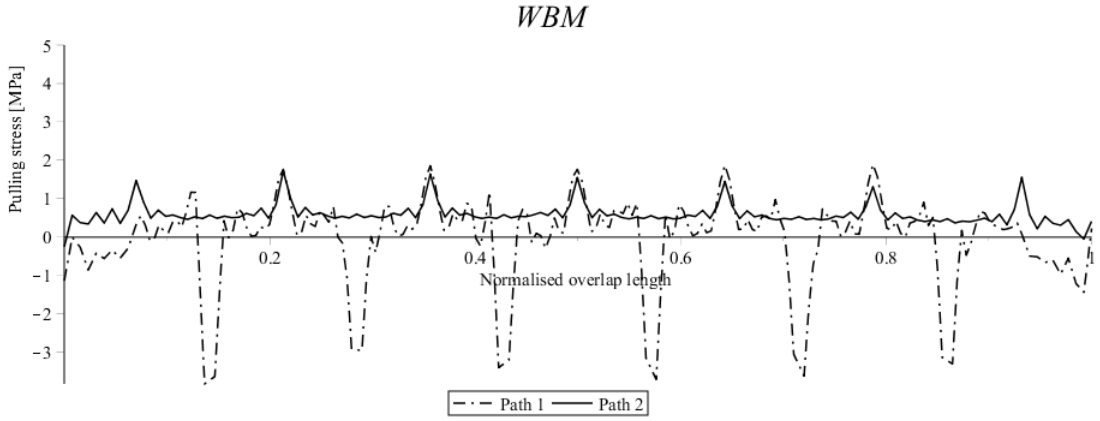

Figure 8.38: Adhesive pulling stress distribution of WBM for both paths presented on Figure 8.37;

region is placed on these locations.

In that case, the adhesive stress distribution along the row of fasteners is a primarily subject of analysis. Nevertheless, the symmetrical location along the adhesive layer is also a component of interest even if there are no fasteners. Both adopted paths are presented on Figure 8.37 and were done in order to analyse the stress development either along the axis of the rivets or on the side without rivets.

This investigation was performed for only two of the models since the stress patterns are identical for all the damaged ones. The conclusions drawn from that analysis can be extrapolated for the remaining models and an extensive presentation of data is avoided.

First, analysing both curves from Figure 8.38 it is noticeable that they have approximately the same peak stresses location between rivet holes.

For curve 1, the abrupt stress drops suggest the location of each rivet along the layer

and as it is possible to visualize, around those rivets the adhesive is subjected to high levels of compression comparatively to the level of tension. This compression occurs probably because of the adhesive smashing, caused by the interaction between the upper rib surface and the lower skin surface when the structure is subjected to pulling. The author believes that the washer on the bottom of the rivet plays an important role on this phenomena since it stuck the rib against the skin lower surface.

For curve 2, the stress distribution is almost constant for the analogous rivet region of curve 1 and the peak stresses are slightly lower than the peak stresses of the curve 1. Apparently the regions between rivets are the most requested regions along the adhesive layer since they are the locations with no additional support, contrarily to the rivets area where most part of the stress is carried by the fastener. Furthermore, although the rivets are responsible for carrying additional load, between them they produce the opposite effect and induce an increase of load comparatively to the stress distribution of path 2. This is corroborated by the higher peaks of curve 1.

Figure 8.39 also verifies this event but, in this case, the higher peaks are also located at the boundaries of the damaged area. The plot is analogous to the plot from Figure 8.38 with the stress distribution of the adhesive layer from WBDM II model. Each path has the same meaning and location of the ones presented on Figure 8.37.

The plot of Figure 8.41 illustrates the development of the transverse pulling stress around the region of rivet 1 according to damage propagation. The adopted path is exhibited on Figure 8.40.

The region on the plot between approximately 65 % and 85 % of the transverse overlap length reveals the location of rivet 1.

The main conclusion is that the stress distribution on that region is not subjected to a significant variation when the level of damage is increased. However, as the level of damage increases a slight rise of pulling stress in the overlap edges is noticed. The reduction of the bonding area, consequence of the damage, could be the reason for that

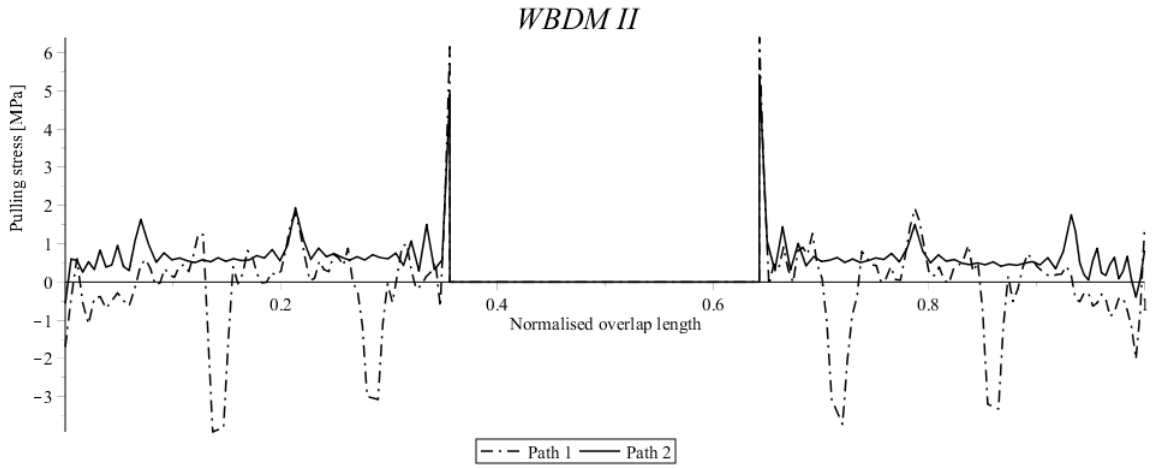

Figure 8.39: Adhesive pulling stress distribution of WBDM II for both paths presented on Figure 8.37;

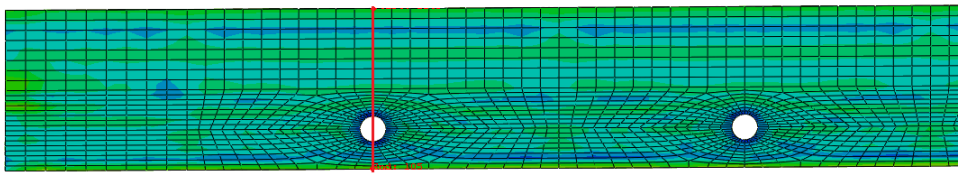

Figure 8.40: Adopted path crossing rivet 1 to collect the transverse pulling stresses according each damage level;

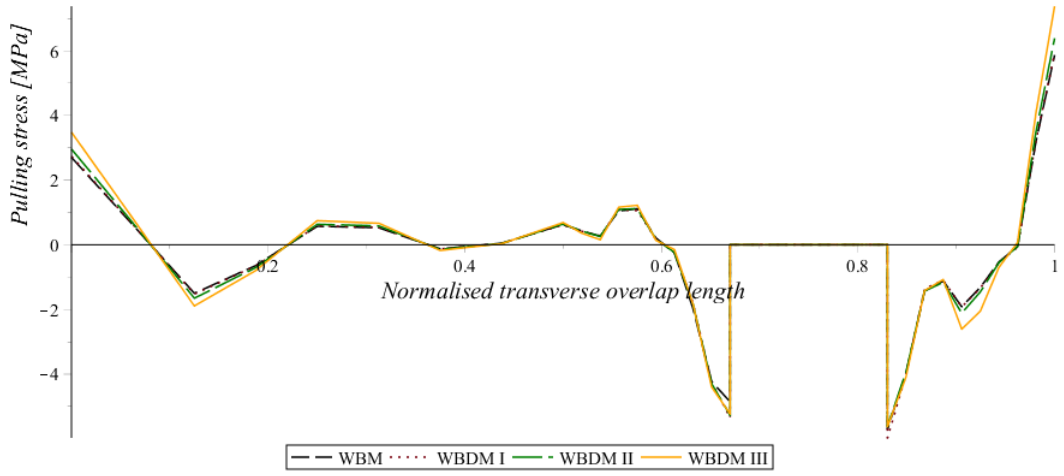

Figure 8.41: Adhesive transverse pulling stress distribution of all models for the path presented on Figure 8.40;

light stress intensification.

Another conclusion is that the transverse overlap edges represent critical load regions since the maximum pulling stresses are developed along this lines. However, the maximum pulling stresses are far away from the adhesive ultimate tension stress.

To understand the effect of damage on stress distribution along the length of the adhesive layer and the possible contribution of the rivets for that stress level, two different paths were adopted to pick the transverse stress distribution on two different zones of the adhesive layer. The chosen models were the WBM and WBDM II. That choice is based only in a trend's illustration purpose since all models revealed the same stress patterns for that two regions with minor differences on stress levels. A small increase on the highest stresses was noticed for both models as the damage level increases. The picking lines are illustrated on Figure 8.42 and from right to left, the paths are 1 and 2 respectively, were path number 1 on WBDM II is coincident with the edge where the damage begins.

Again, the highest drop on paths number 2 illustrate the position of the rivet hole, approximately between 65 % and 85 % of the transverse overlap length.

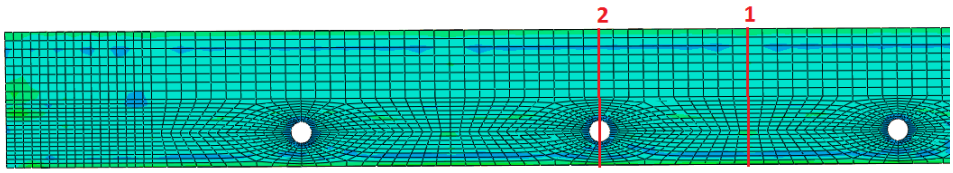

Figure 8.42: Adopted paths to collect the transverse pulling stresses;

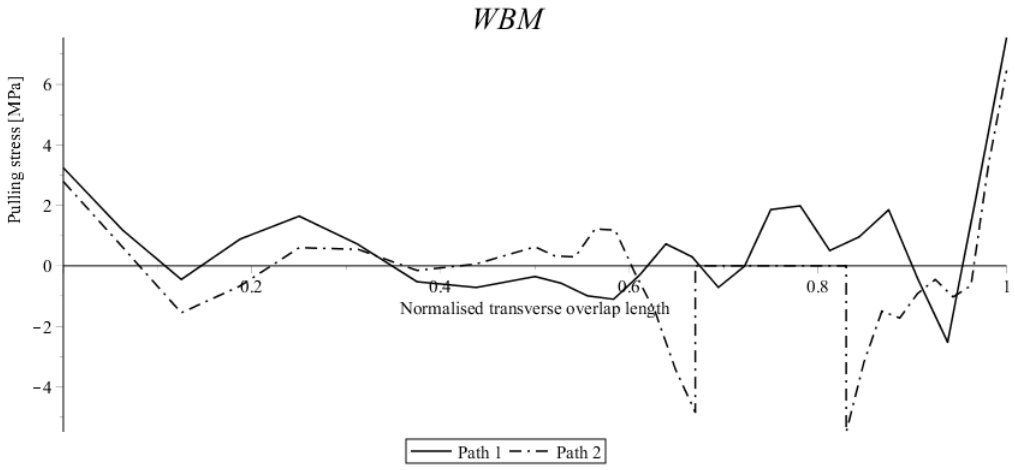

Figure 8.43: Adhesive transverse pulling stress distribution of WBM for both paths presented on Figure 8.42;

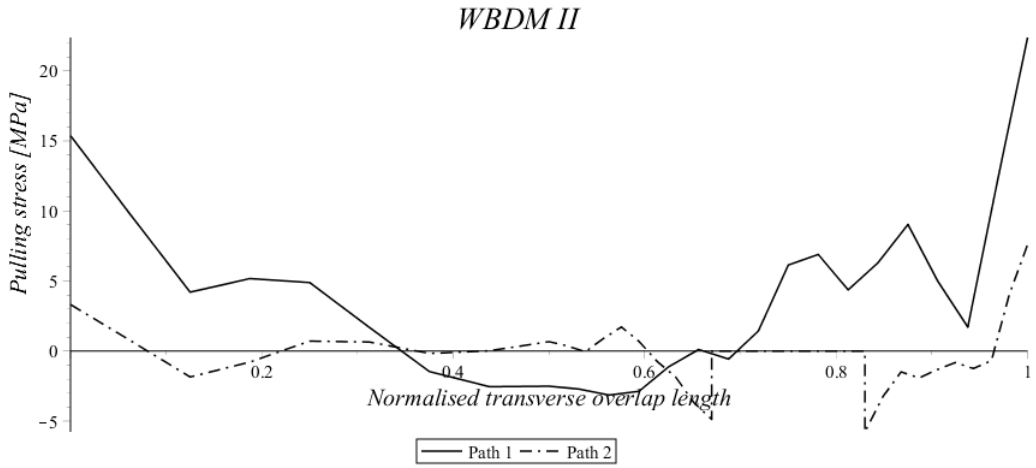

Figure 8.44: Adhesive transverse pulling stress distribution of WBDM II for both paths presented on Figure 8.42;

Analysing both plots from Figures 8.43 and 8.44, the stresses along the path number 2, where the rivet is placed, presents a significant decrease on stress level and a more uniform distribution, which can be in part due to the contribution of the rivet to carry some load.

However, for the damaged model a more pronounced reduction is evident which suggests that the adhesive damage promotes an increase on pulling stresses at its boundaries. According to that, the surrounding rivets would be responsible to carry more load than the rivets on the WBM.

Relating all the damaged models, the pulling stress pattern along the length of the adhesive layer seems to hold the highest stress level on the boundaries of the damage area and it progressively decreases as it goes towards the longitudinal edges of the adhesive layer.

Regarding the curve 2 from the WBDM II that region has the highest pulling stresses located on transverse overlap edges and the maximum stress is slightly below the adhesive ultimate tension stress (28.60 MPa). Therefore, the failure of the adhesive layer is more

predictable to start at this overlap edge, where the pulling stress is 22.4 MPa, representing a potential critical point of failure initiation.

Although the latter analysis and the respective draw of conclusions, the levels of stress on that case for both paths number 2 are very low, almost around zero. Hence, the impact of these stress levels on the structure behaviour and on main conclusions is not as significant as it could be.

It demonstrates another reason for the importance of fasteners application on a wing box joint. The pulling stress is mainly supported by the rivets instead of the adhesive layer. Therefore, the level of stress on that adhesive layer is not too significant for structure analysis.

8.2.2.2 Shear Stress

The adhesive shear stress distribution for each damaged model (Figure 8.45, 8.46, 8.47 and 8.48) was obtained according to the same path of pulling stress distributions and schematically illustrated previously on Figure 8.32.

On the opposite to pulling, shear stress levels increase around the fasteners holes and decreases along the spaces in between. The overlap edges are the regions with highest values of shear stresses. Also as the damage level increases, a slight shear stress increase occurs on those overlap boundaries.

Contrarily to pulling stress distribution, there is no peak stress at the limits of damaged area.

The comparison made for pulling stresses according to two parallel longitudinal paths (Figure 8.38 and 8.39) through the adhesive layer was also performed for the shear stress distribution. Both paths previously adopted are the same for this investigation and are illustrated on Figure 8.37. Thus, Figure 8.49 and 8.50 show the shear stress distribution along both parallel paths for WBM and WBDM II.

The peak of shear stresses occurs in two distinct ways: For path 1, besides the highest

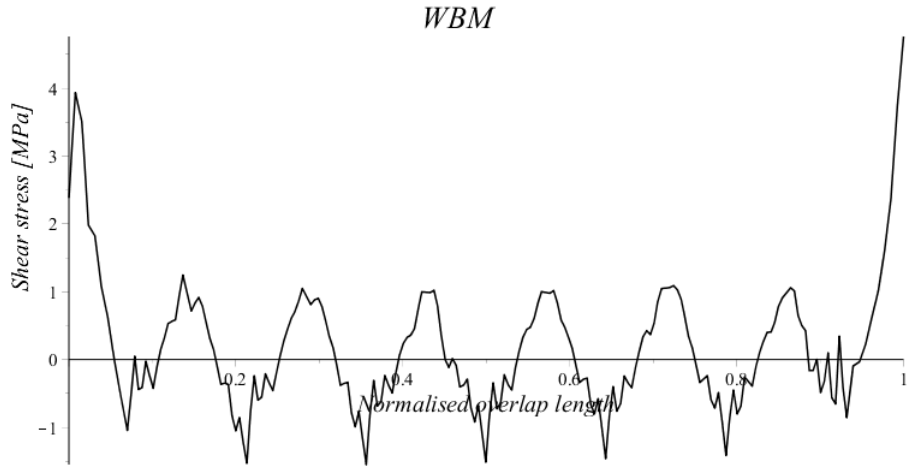

Figure 8.45: Adhesive shear stress distribution;

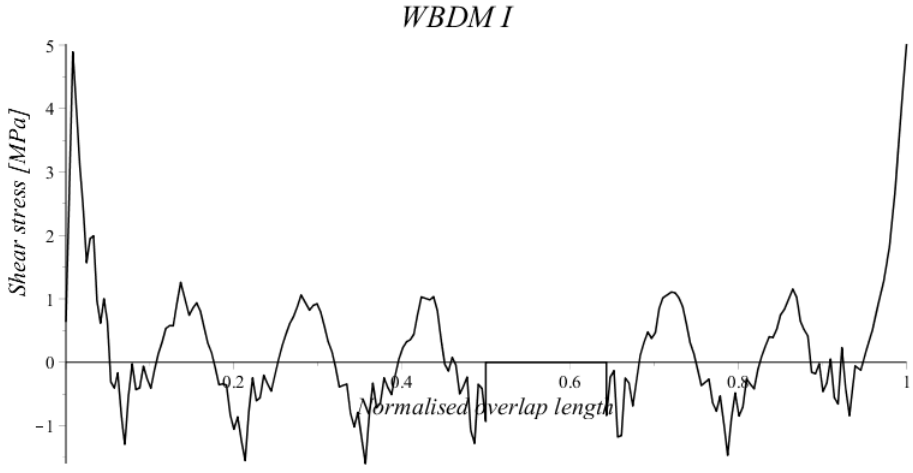

Figure 8.46: Adhesive shear stress distribution for damage level 1;

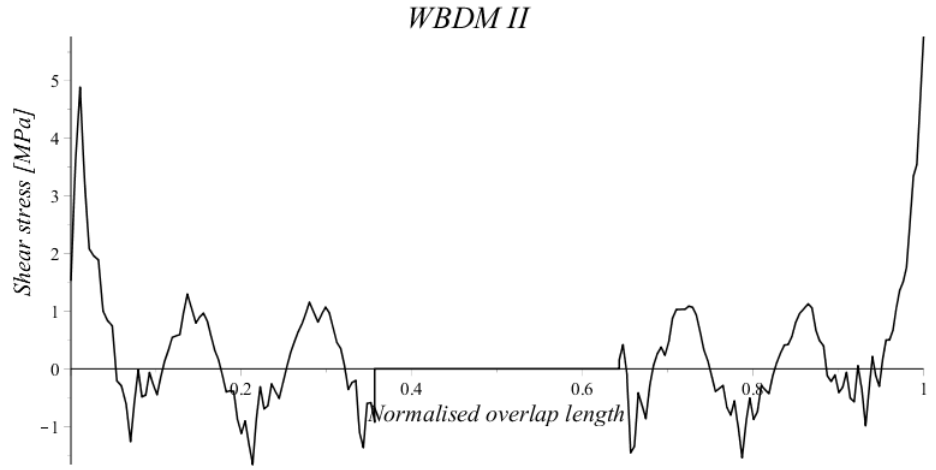

Figure 8.47: Adhesive shear stress distribution for damage level 2;

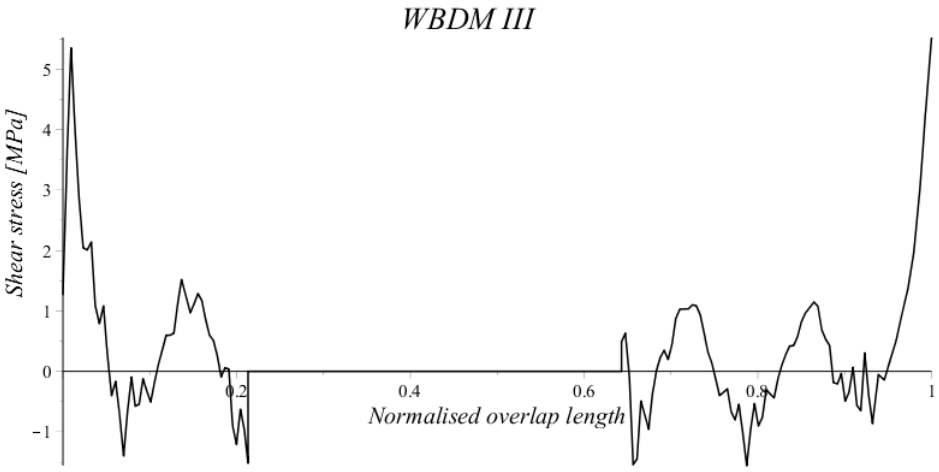

Figure 8.48: Adhesive shear stress distribution for damage level 3;

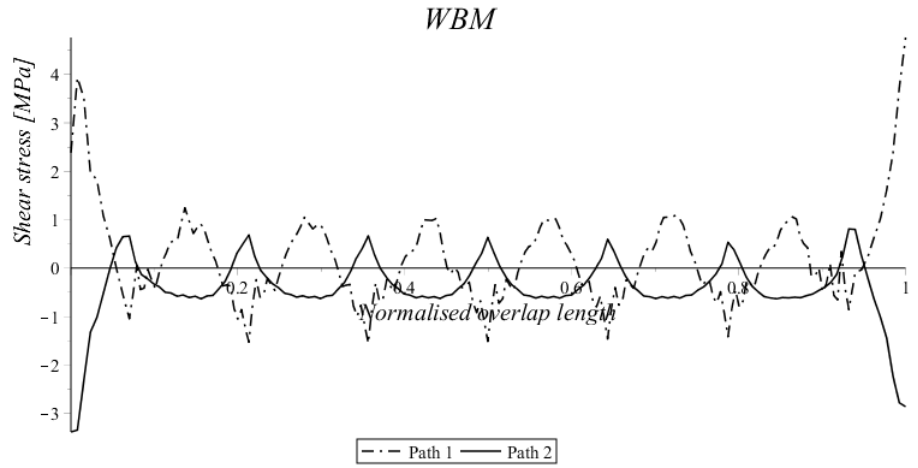

Figure 8.49: Adhesive shear stress distribution of WBDM for both paths presented on Figure 8.37;

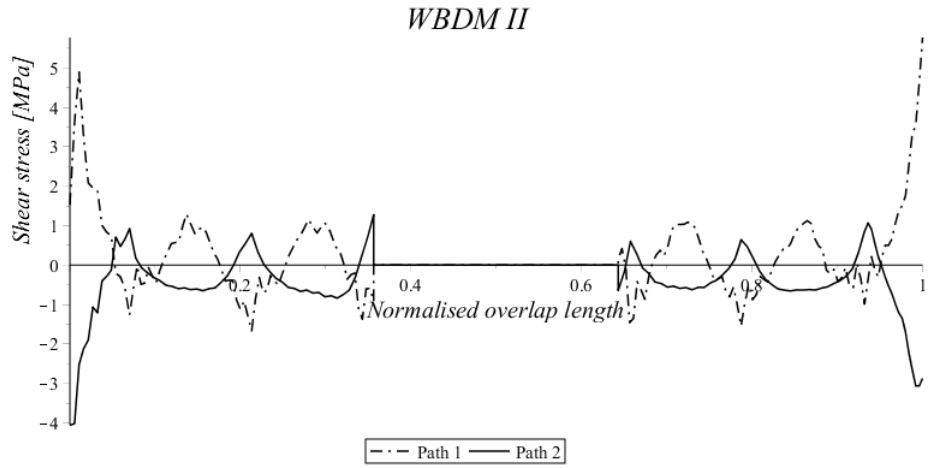

Figure 8.50: Adhesive shear stress distribution of WBDM II for both paths presented on Figure 8.37;

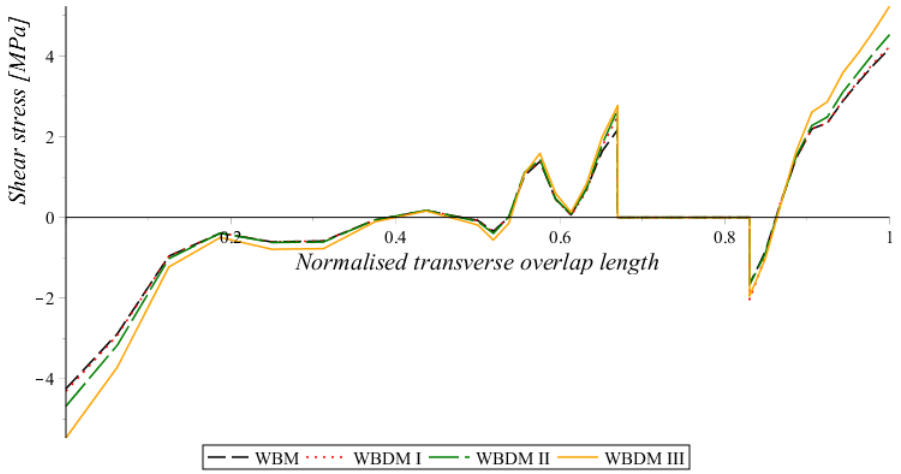

Figure 8.51: Adhesive shear pulling stress distribution of all models for the path presented on Figure 8.40;

stresses at the overlap edges, the peaks are located around the rivets holes while for path 2 the peaks occurs between rivets.

The peaks of path 1 could be justified by the bending of the areas surrounding the rivets, which cause positive shear stresses, while the opposite bending of the structure between the rivets cause negative shear stresses. For path 2, the regions of lower shear stress are located behind the rivets which suggests the ability of the rivets to reduce the stress level on that surrounding area.

As it was previously discussed, the limits of the damaged area are not inducing peaks of shear stress as it occurs for pulling stresses.

The comparison made for the evolution of pulling stress distributions around the position of rivet 1 according to the increase of damage (Figure 8.41) was also performed for shear stress distributions. The path previously adopted is the same for this investigation and is illustrated on Figure 8.40. Thus, Figure 8.51 shows the shear stress distribution along that transverse path for all models.

Analysing the plot from figure 8.51 the variation of the shear stresses distribution

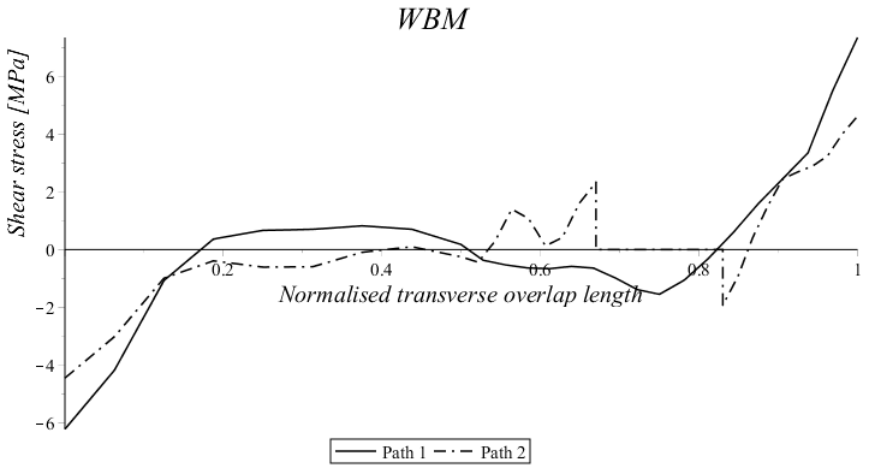

Figure 8.52: Adhesive transverse shear stress distribution of WBM for both paths presented on Figure 8.42;

on that location of the adhesive layer does not varies significantly with the increase of damage. The maximum stresses are located at the transverse overlap edges but far away from the ultimate shear stress. Comparatively to the pulling stress distribution, on this case the maximum shear stresses varies more between each other than the maximum pulling stresses of Figure 8.41.

The comparison made for pulling stresses according two parallel transverse paths (Figure 8.43 and 8.44) through the adhesive layer was also performed for the shear stress distribution. Both paths previously adopted are the same for this investigation and are illustrated on Figure 8.42. Thus, Figure 8.52 and 8.53 show the shear stress distribution for WBM and WBDM II along those two paths.

Analysing the curves from both plots, the edges are holding the highest shear stresses and they vary from a compressive stress state at the beginning of the path to a tensile stress state at the end of the path.

It is notorious the ability of the rivet to lower the shear stresses on the edges of path 2. The region between rivets illustrated by path 1 holds higher levels of shear stress

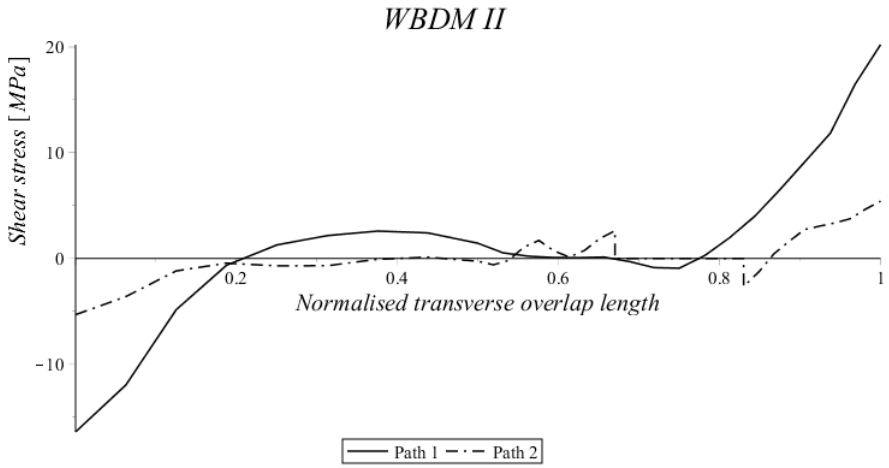

Figure 8.53: Adhesive transverse shear stress distribution of WBDM II for both paths presented on Figure 8.42;

since that region does not have as much support as the region where the rivet is placed. This trend occurs for all models. The transverse shear stress distributions have their peaks at the maximum distance between rivet holes and they decrease as the distribution moves towards the rivet hole. However, when the path 1 is coincident with a boundary of damaged region, (for example the case of WBDM II) the peak of shear stress is upgraded to a new maximum level. Hence, the limit of a damaged region increases the peak of transverse shear stress comparatively to a continuous adhesive layer. This conclusion can be drawn through the comparison of both plots.

This positive level of shear stress occurring on the adhesive edge of WBDM II should be treated carefully, since it is slightly above the ultimate shear stress of the adhesive. This point represents the failure initiation of the adhesive layer and in real service application the adhesive on this area could be already damaged or some crack propagation could be initiated. Almost the same conclusions of pulling stress analysis could be made since the rivets are able to reduce the stress level either for shear or pulling request.

8.2.3 Conclusions

- The composite rivets are able to reduce pulling and shear stresses along their transverse surrounding regions;
- The boundaries of damage on adhesive layer are locations that promote the increase of shear and pulling stresses;
  - As the damage level increases the level of stress on that boundaries also increase;
- The highest stresses were found on rivets surfaces, specially on those rivets located on disbonded areas;
- The application of that rivets is crucial on a wing box joint since the major part of stresses are carried by them, leaving the adhesive layer with a residual stress level;
- The evolution of stress on adhesive layer around rivet 1, and according to the increase of damage, has no significant change on pulling stress. For shear stress the change is not truly relevant but is higher comparatively to pulling.
- The increase of carried stress by the safe rivets when the damage increases could predict a damage tolerance effect, specially when the disbond limit is coincident with the position of those rivets. The author believes that those rivets could hold on the damage propagation of the adhesive at some stage.

Conclusions and Future work

8.3 Conclusions

According to the first category of models and considering a numerical point of view, the application of the new design of a composite rivet seems to be viable relatively to the other joining techniques. The bonded-bolted model with the titanium rivet can hold higher levels of stress while the analogous model with the composite rivet demonstrates a reasonably identical trend, lowered probably due to the lower material equivalents modulus.

For a single lap bonded-bolted joint subjected to shear, the load carrying is dominated by the adhesive layer. The role of the fastener is small until the adhesive failure but pushes that failure to higher levels. During that event, the composite fastener ensures a smooth step on carried load avoiding undesirable sudden drops. This feature is vital to provide a gentle transition between adhesive failure and fastening activity. Thenceforward, the composite fastener is responsible to take the remaining load up to final failure of the structure.

According to the second category of models and considering a numerical point of view, the level of pulling stress found along the rivets are significantly higher than the level of pulling stress found along the adhesive layer. This fact warns for the dependency of the rivets by a wing box section subjected to pulling. The load carrying on this case is dominated by the rivets. Those composite fasteners are capable to withstand three levels

of adhesive damage and three levels of pulling load. The author believes that the rivets placed close to the damage limits are able to improve damage tolerance and avoid damage propagation.

Besides that, composite rivets have the ability to lower the surrounding shear and pulling stresses within the adhesive layer.

8.4 Future work

This thesis presented a numerical study of a new concept on composite fastening, however, there are still developments to be made in order to enhance and corroborate the results and procedures adopted here.

- One of the first improvements to be applied is related to the experimental validation of the numerical research through the manufacturing of a composite joint fastened with a composite rivet. That rivet should be made recurring to a tool which allows the rolling of a laminate. Also the 3 remaining composite joints of models category 1 should be manufactured and tested;

- Titanium rivet could be modelled with a damage criteria as the ones available in *Abaqus ®* for ductile metals [45];

- The adhesive layer in the overlaps of models from category 1 could be modelled with different types of adhesive in order to understand the effects on joint behaviour for different ranges of adhesive properties.

- Standard *Hashin* damage modelling could possibly be applied on composite adherends if 3D solid elements were not being used. If the whole analysis is replaced by 2D or shell elements, *Abaqus ®* would allow the modelling of composite damage. Another option is based on using *Abaqus ®* user subroutines to programming a composite damage model for 3D elements.

- The adhesive film that surrounds the rivets of the bonded-bolted single lap joints and ensures the connection between fastener and plate hole could be modelled with cohesive elements and characterized by a cohesive zone model or modelled with a cohesive surface behaviour. Both techniques are available in *Abaqus ®* and permit the modelling of the adhesive damage and consequently adhesive failure during the analysis;

- The materials of the skins and ribs from the models of category 2 could be replaced by composite materials; Also the washers on each rivet could be replaced by an adhesive film like on the models of category 1 and taking into account damage propagation;

- The damage flaws on adhesive layer of models from category 2 could have lower gaps between consecutive damage levels. The difference between lengths of damage should be lower in order to get the limit of damaged area coincident with the axis of one of the rivets;

- The fastening of this new concept is a challenging engineering problem since the old techniques and tools to clinch and squeeze metallic rivets could induce some severe damage on the composite fastener. For that reason, the bonding of the fastener or a co-curing procedure could be a feasible method to apply those fasteners though a large amount of investigation through numerical studies and experimental test is needed;

- Although a specific countersunk rivet modelled by a rolled composite laminate was studied, other types of rivet heads and manufacture procedures could be investigated;

- On a future experimental work the core of the composite rivet would have a specific region to incorporate some load cell or a transducer. The aim of this application is

to create a real time monitoring system within the rivet structure.

Bibliography

[1] Johan Ekh. *Multi-fastener single-lap joints in composite structures.* PhD thesis, Royal Institute of Technology, SE-100 44 Stockholm, Sweden, 2006.

[2] Nassar Sayed A. and Yang Xianjie. *Fastening and Joining of Composite Materials*, pages 5–23. Springer New York, New York, NY, 2013.

[3] L.F.M. da Silva and R.D.S.G. Campilho. 2 - design of adhesively-bonded composite joints. In A.P. Vassilopoulos, editor, *Fatigue and Fracture of Adhesively-Bonded Composite Joints*, pages 43 – 71. Woodhead Publishing, 2015.

[4] Farid Gamdani, Rachid Boukhili, and Aurelian Vadean. Tensile strength of open-hole, pin-loaded and multi-bolted single-lap joints in woven composite plates. *Materials and Design*, 88:702 – 712, 2015.

[5] Federal Aviation Administration (Faa). *Aviation Maintenance Technician Handbook-Airframe.* FAA Handbooks Series. Aviation Supplies & Academics, 2012.

[6] C. Niu and M.C.Y. Niu. *Airframe Structural Design: Practical Design Information and Data on Aircraft Structures.* Airframe book series. Conmilit Press Limited, 1999.

[7] J.F. Douglas. *Fluid Mechanics.* Pearson/Prentice Hall, 2005.

[8] B.R. Munson, D.F. Young, T.H. Okiishi, and W.W. Huebsch. *Fundamentals of fluid mechanics.* Wiley, 2009.

[9] Robert W. Messler Jr. Chapter 3 - mechanical fasteners, integral attachments, and other mechanical joining methods. In Robert W. Messler, editor, *Joining of Materials and Structures*, pages 105 – 176. Butterworth-Heinemann, Burlington, 2004.

[10] G. Li, G. Shi, and N.C. Bellinger. 6 - assessing the riveting process and the quality of riveted joints in aerospace and other applications. In M.C. Chaturvedi, editor, *Welding and Joining of Aerospace Materials*, Woodhead Publishing Series in Welding and Other Joining Technologies, pages 181 – 214. Woodhead Publishing, 2012.

[11] NavyBMR. Aircraft hardware. `http://navybmr.com/study\%20material/14014a/14014A\_ch6.pdf`. Accessed on 27/05/2016.

[12] R.S. Khurmi and J.K. Gupta. *Machine Design*. Eurasia Publishing House, 2005.

[13] A. Skorupa and M. Skorupa. *Riveted Lap Joints in Aircraft Fuselage: Design, Analysis and Properties*. Solid Mechanics and Its Applications. Springer Netherlands, 2012.

[14] Ajax Fasteners Australia. Rivet handbook. `http://www.ajaxfast.com.au/sitepdfs/AjaxRivetsHandbook.pdf`. Accessed on 16/03/2016.

[15] Fabrizio Moroni and Alessandro Pirondi. *Technology of Rivet: Adhesive Joints*, pages 79–108. Springer Berlin Heidelberg, Berlin, Heidelberg, 2011.

[16] T. Sadowski, M. Kneć, and P. Golewski. Experimental investigations and numerical modelling of steel adhesive joints reinforced by rivets. *International Journal of Adhesion and Adhesives*, 30(5):338 – 346, 2010. Special Issue on Joint Design.

[17] P.P. Camanho and F.L. Matthews. Stress analysis and strength prediction of mechanically fastened joints in frp: a review. *Composites Part A: Applied Science and Manufacturing*, 28(6):529 – 547, 1997.

[18] Collings T. A. The strength of bolted joints in multi-directional cfrp laminates. *Journal of Composites*, 1977.

[19] L. J. Hart-Smith. *Mechanically-Fastened Joints for Advanced Composites — Phenomenological Considerations and Simple Analyses*, pages 543–574. Springer US, Boston, MA, 1980.

[20] Tomas Ireman. Three-dimensional stress analysis of bolted single-lap composite joints. *Composite Structures*, 43(3):195 – 216, 1998.

[21] L.J.Hart-Smith. Bonded-bolted composite joints. *Journal of Aircraft*, 22(11):993–1000, 1985.

[22] D Duthinh. Connections of fiber-reinforced polymer (frp) structural members: a review of the state of the art. *National Institute of Standards and Technology*, 2000.

[23] Zlatan Kapidžić, Larsgunnar Nilsson, and Hans Ansell. Finite element modeling of mechanically fastened composite-aluminum joints in aircraft structures. *Composite Structures*, 109:198 – 210, 2014.

[24] Indira Gandhi National Open University. Basics of riveted joints. `www.ignou.ac.in/upload/Unit-3-60.pdf`. Accessed on 17/03/2016.

[25] Lucas Filipe Martinsda Silva, António Gonçalves de Magalhães, and Marcelo Francisco SF de Moura. *Juntas adesivas estruturais*. Publindustria, 2007.

[26] S.Vedhagiri Wen S.Chan. Analysis of composite bonded/bolted joints used in repairing. *Journal of Composite Materials*, 35(12):1045–1061, 2001.

[27] Jin-Hwe Kweon, Jae-Woo Jung, Tae-Hwan Kim, Jin-Ho Choi, and Dong-Hyun Kim. Failure of carbon composite-to-aluminum joints with combined mechanical fastening and adhesive bonding. *Composite Structures*, 75(1–4):192 – 198, 2006. Thirteenth

International Conference on Composite StructuresICCS/13Thirteenth International Conference on Composite Structures.

[28] S A Grammatikos, E Z Kordatos, T E Matikas, and A S Paipetis. Service and maintenance damage assessment of composite structures using various modes of infrared thermography. *IOP Conference Series: Materials Science and Engineering*, 74(1):012006, 2015.

[29] Pawel Malinowski, Tomasz Wandowski, and Wieslaw Ostachowicz. The use of electromechanical impedance conductance signatures for detection of weak adhesive bonds of carbon fibre–reinforced polymer. *Structural Health Monitoring*, 14(4):332–344, 2015.

[30] Maxwell Davis and David Bond. Principles and practices of adhesive bonded structural joints and repairs. *International Journal of Adhesion and Adhesives*, 19(2):91 – 105, 1999.

[31] A.P. Vassilopoulos. 18 - construction engineering: Fatigue life prediction of adhesively bonded textile composites. In Valter Carvelli and Stepan V. Lomov, editors, *Fatigue of Textile Composites*, Woodhead Publishing Series in Composites Science and Engineering, pages 441 – 481. Woodhead Publishing, 2015.

[32] Lucas F M da Silva and R D Adams. Techniques to reduce the peel stresses in adhesive joints with composites. *International Journal of Adhesion and Adhesives*, 27(3):227 – 235, 2007.

[33] V.K. Ganesh and T.S. Choo. Modulus graded composite adherends for single-lap bonded joints. *Journal of Composite Materials*, 36(14), 2002.

[34] J.N Boss, V.K Ganesh, and C.T Lim. Modulus grading versus geometrical grading of composite adherends in single-lap bonded joints. *Composite Structures*, 62(1):113 – 121, 2003.

[35] MD Banea and Lucas FM da Silva. Adhesively bonded joints in composite materials: an overview. *Proceedings of the Institution of Mechanical Engineers, Part L: Journal of Materials Design and Applications*, 223(1):1–18, 2009.

[36] Naveen Rastogi, Som R Soni, and Arvind Nagar. Thermal stresses in aluminum-to-composite double-lap bonded joints. *Advances in Engineering Software*, 29(3–6):273 – 281, 1998.

[37] Lucas F.M. da Silva, R.D. Adams, and M. Gibbs. Manufacture of adhesive joints and bulk specimens with high-temperature adhesives. *International Journal of Adhesion and Adhesives*, 24(1):69 – 83, 2004.

[38] J.A.B.P. Neto, R.D.S.G. Campilho, and L.F.M. da Silva. Parametric study of adhesive joints with composites. *International Journal of Adhesion and Adhesives*, 37:96 – 101, 2012. Special Issue on Joint Design 3.

[39] WW Wright. A review of the influence of absorbed moisture on the properties of composite materials based on epoxy resins. *RAE Technical Memorandum, Mat324*, 1979.

[40] AJ Kinloch. Durability of structural adhesives. *Applied Science Publishers, 22 Rippleside Commercial Estate, Ripple Road, Barking, Essex IG 11 OSA, England, 1983.*, 1983.

[41] Parker B. M. The effect of composite pre-bond moisture on adhesive-bonded cfrp-cfrp joints. *Journal of Composites*, 14:226–232, 1983.

[42] RDSG Campilho, MD Banea, JABP Neto, and LFM Da Silva. Modelling of single-lap joints using cohesive zone models: effect of the cohesive parameters on the output of the simulations. *The Journal of Adhesion*, 88(4-6):513–533, 2012.

[43] R.D.S.G. Campilho, M.D. Banea, J.A.B.P. Neto, and L.F.M. da Silva. Modelling adhesive joints with cohesive zone models: effect of the cohesive law shape of the adhesive layer. *International Journal of Adhesion and Adhesives*, 44:48 – 56, 2013.

[44] M Ridha, VBC Tan, and TE Tay. Traction–separation laws for progressive failure of bonded scarf repair of composite panel. *Composite Structures*, 93(4):1239–1245, 2011.

[45] *Simulia Abaqus/CAE v6.12 User's Manual*.

[46] Gordon Kelly. Load transfer in hybrid (bonded/bolted) composite single-lap joints. *Composite Structures*, 69(1):35 – 43, 2005.

[47] Wei-Hwang Lin and Ming-Hwa R Jen. The strength of bolted and bonded single-lapped composite joints in tension. *Journal of Composite Materials*, 33(7):640–666, 1999.

[48] FL Matthews. Joining fibre-reinforced plastics. *Elsevier Applied Science Publishers Ltd, Crown House, Linton Road, Barking, Essex IG 11 8 JU, UK, 1987.*, 1987.

[49] S. Guo. Design and analysis of composite structures - AVD MSc Course Appointments. April 2015.

[50] Saphire products limited - the rivet supply company. `http://www.sapphireproducts.co.uk/4620t6.htm`. Accessed on 19/04/2016.

[51] Alaattin Aktas and M. Husnu Dirikolu. An experimental and numerical investigation of strength characteristics of carbon-epoxy pinned-joint plates. *Composites Science and Technology*, 64(10–11):1605 – 1611, 2004.

[52] Seong-Yoon Yoo, Cheol-Hwan Kim, Jin-Hwe Kweon, and Jin-Ho Choi. The structural analysis and strength evaluation of the rivet nut joint for composite repair. *Composite Structures*, 136:662 – 668, 2016.

[53] S. Guo and R. Morishima. Numerical analysis and experiment of composite sandwich t-joints subjected to pulling load. *Composite Structures*, 94(1):229 – 238, 2011.

[54] Pedro M G P Moreira, Paulo J Tavares, R.D.S.G. Campilho, and T.A.B. Fernandes. Icsi 2015 the 1st international conference on structural integrity funchal, madeira, portugal 1st to 4th september, 2015 comparative evaluation of single-lap joints bonded with different adhesives by cohesive zone modelling. *Procedia Engineering*, 114:102 – 109, 2015.

[55] N.S. Gokhale. *Practical Finite Element Analysis*. Finite To Infinite, 2008.

[56] A Blom, H Ansell, T Nyman, and J Schön. Fatigue of composite airframe structures. In *Proceedings of the International Conference on Fatigue of Composites*, pages 22–31, 1997.

Appendixes

8.5 Appendix A

Saphire Rivet Catalogue

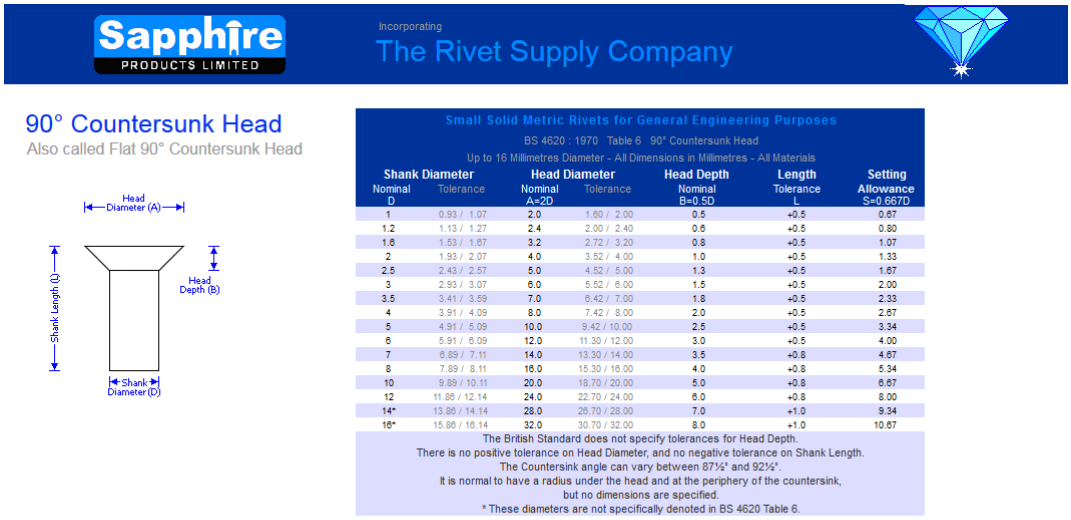

Figure 8.54: Saphire Rivet Catalogue; [50]

8.6 Appendix B

Wing box geometries

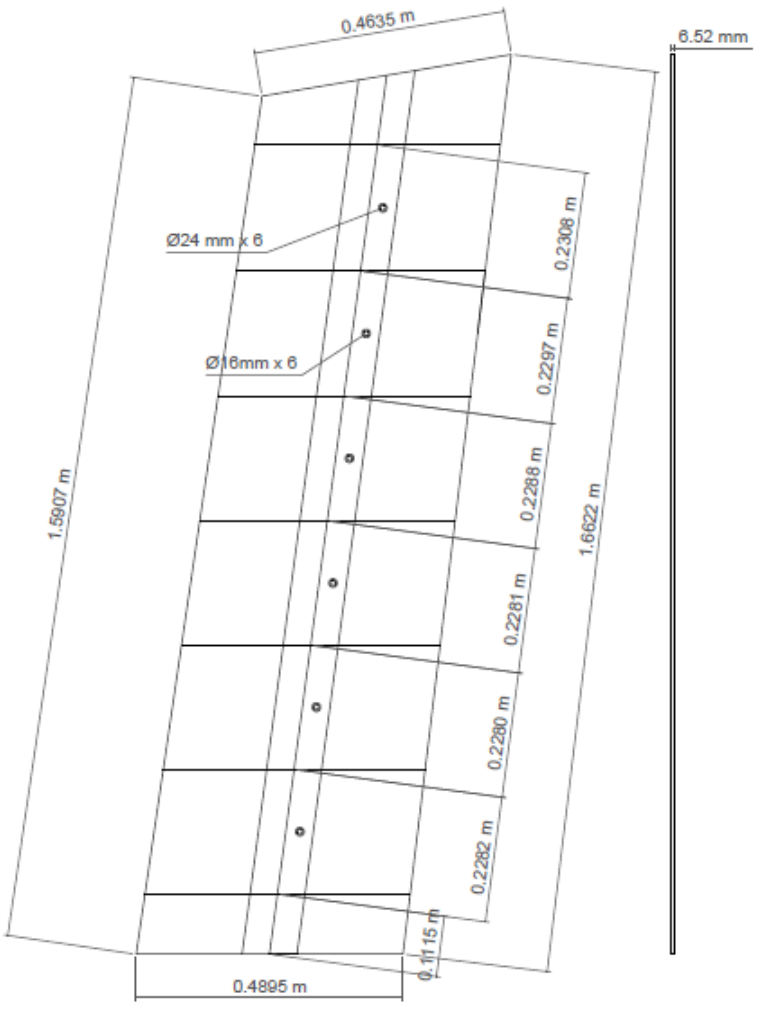

Figure 8.55: Geometry of the top skin;

Figure 8.56: Geometry of the bottom skin;

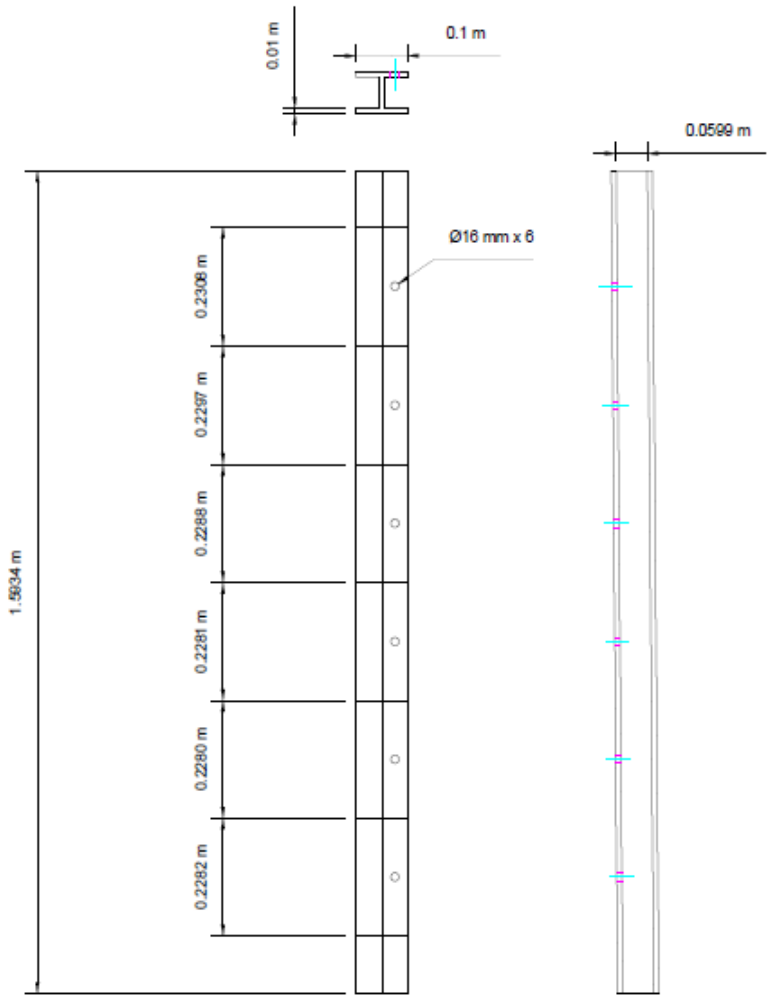

Figure 8.57: Geometry of the rib;

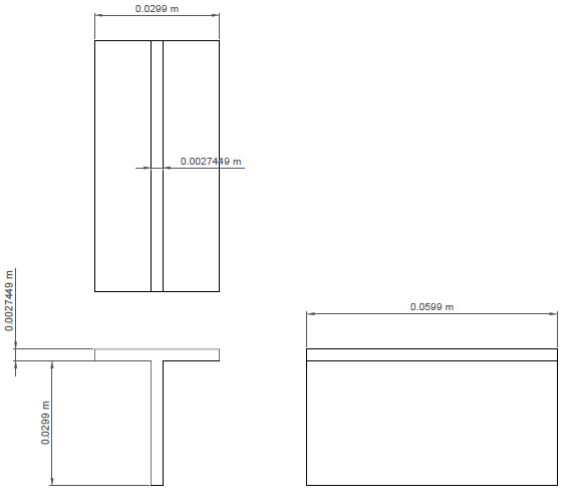

Figure 8.58: Geometry of the stiffeners;

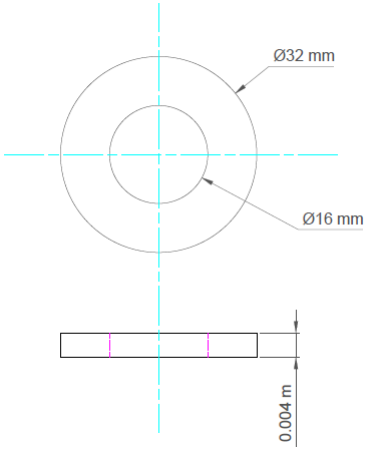

Figure 8.59: Geometry of the washers;

8.7 Appendix C

Shear stress distribution of adhesive overlap - SLJ

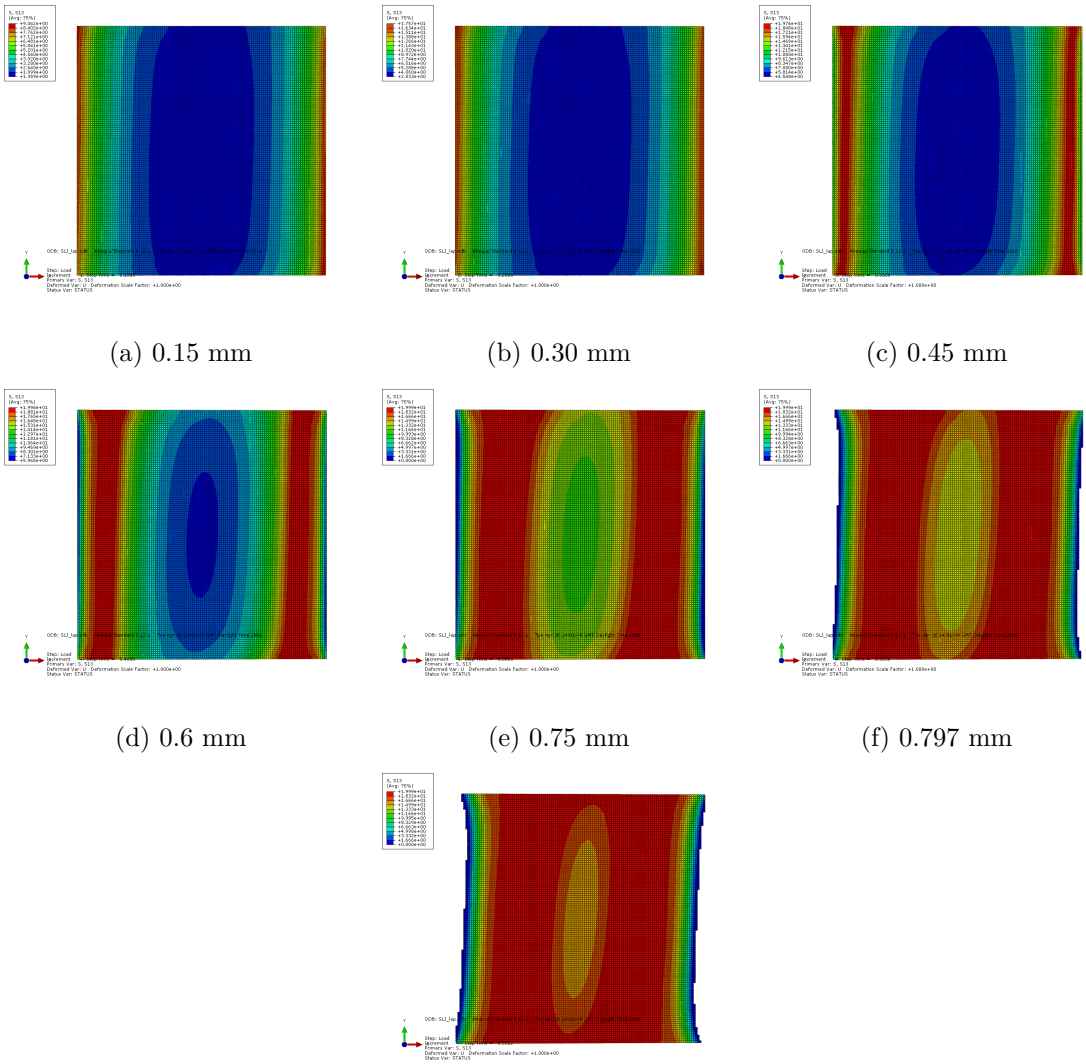

(a) 0.15 mm (b) 0.30 mm (c) 0.45 mm

(d) 0.6 mm (e) 0.75 mm (f) 0.797 mm

(g) 0.799 mm

Figure 8.60: Shear stress distribution of adhesive overlap from SLJ along the increase of applied displacement;

Shear stress distribution of adhesive overlap - SLJ+H

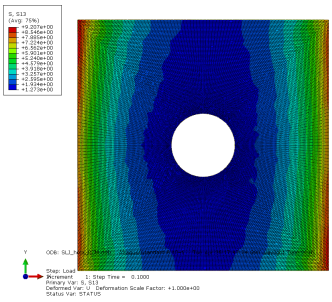

(a) 0.15 mm

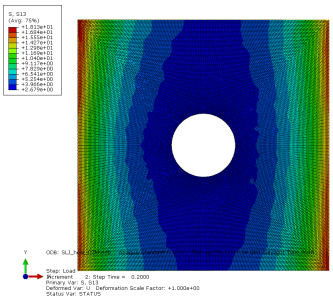

(b) 0.30 mm

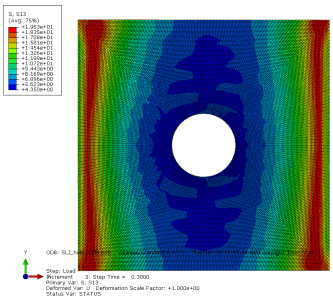

(c) 0.45 mm

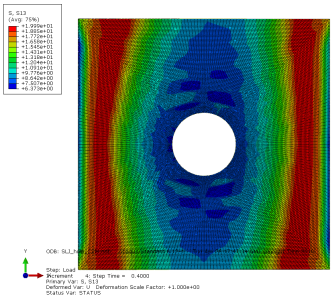

(d) 0.6 mm

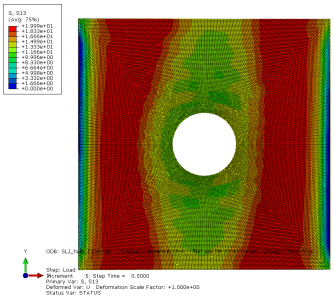

(e) 0.75 mm

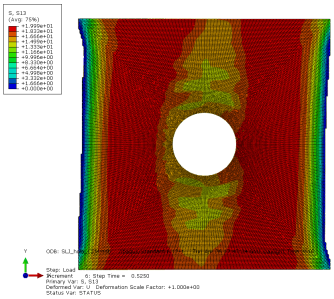

(f) 0.788 mm

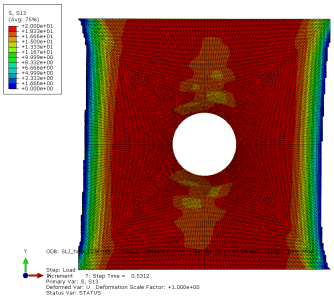

(g) 0.797 mm

Figure 8.61: Shear stress distribution of adhesive overlap from SLJ+H along the increase of applied displacement;

Shear stress distribution of adhesive overlap - CRM

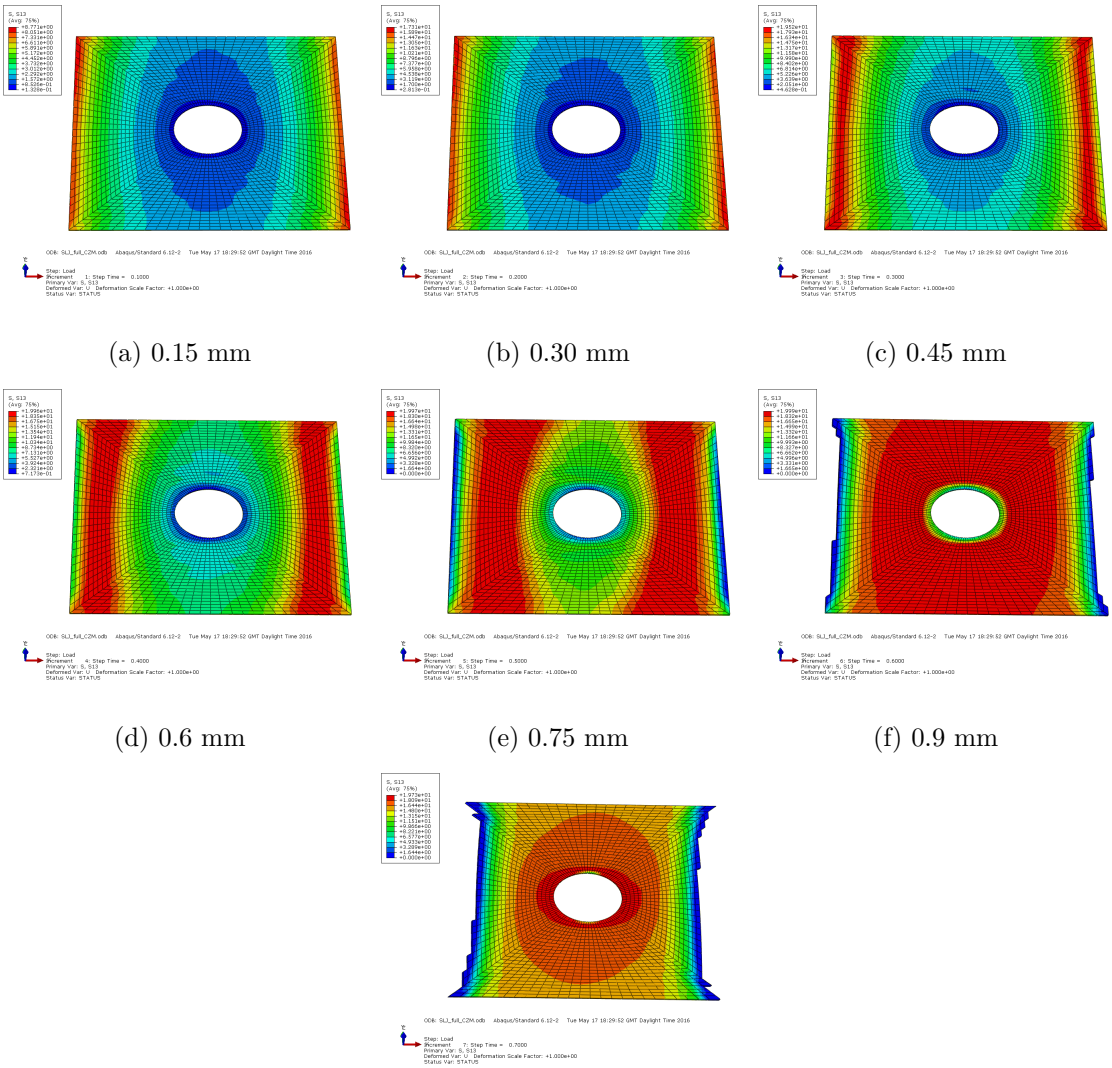

(a) 0.15 mm (b) 0.30 mm (c) 0.45 mm

(d) 0.6 mm (e) 0.75 mm (f) 0.9 mm

(g) 1.05 mm

Figure 8.62: Shear stress distribution of adhesive overlap from CRM along the increase of applied displacement;

Shear stress distribution of adhesive overlap - TRM

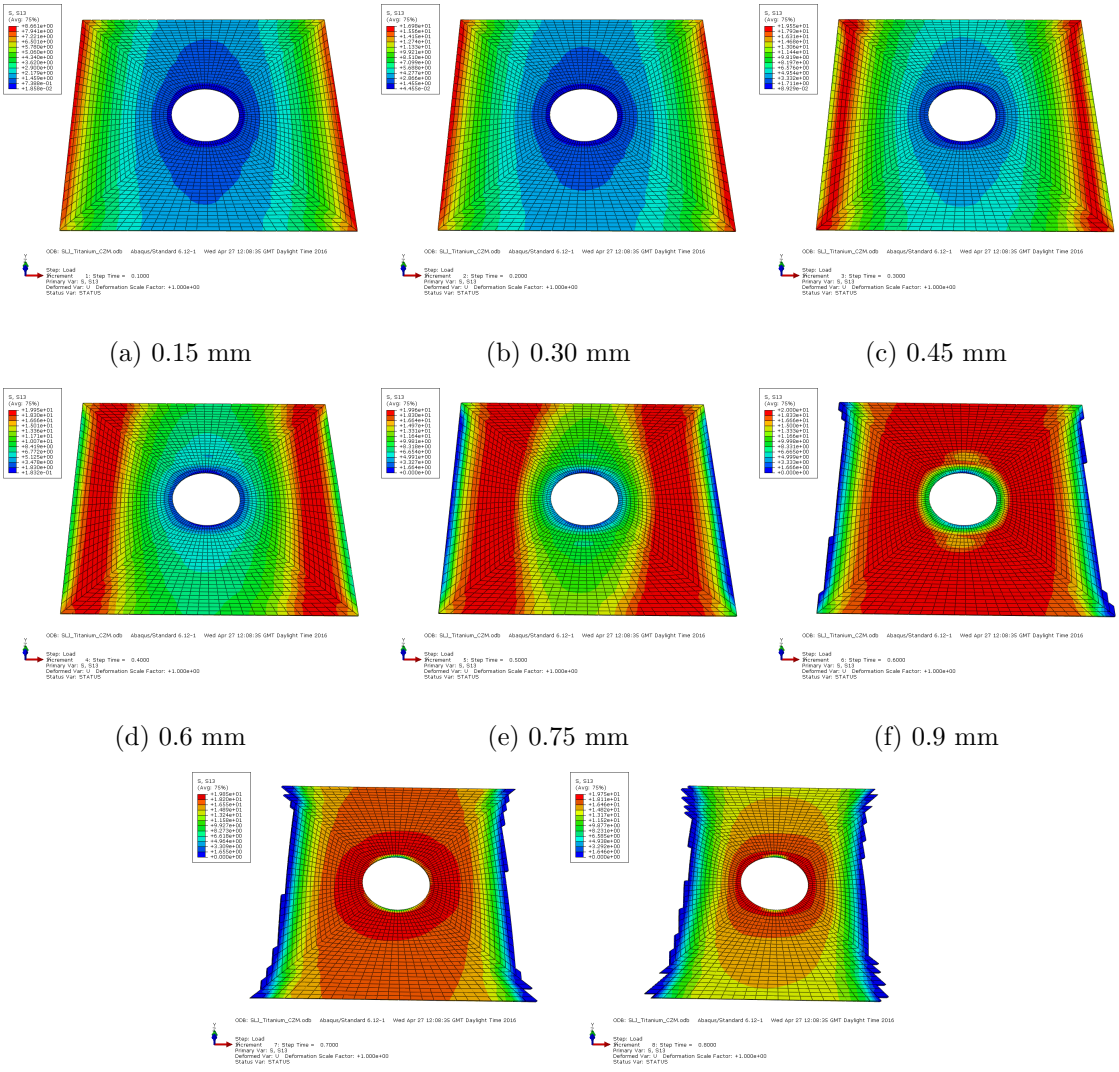

(a) 0.15 mm (b) 0.30 mm (c) 0.45 mm

(d) 0.6 mm (e) 0.75 mm (f) 0.9 mm

(g) 1.05 mm (h) 1.20 mm

Figure 8.63: Shear stress distribution of adhesive overlap from TRM along the increase of applied displacement;

8.8 Appendix D

This appendix contains the values distribution from the quadratic nominal stress criterion used on *Abaqus*®. Values = 1 or filled with red colour on the contour plot means that the damage initiation has started on that region and thenceforward, the stress evolution is governed by the damage evolution law.

Damage Initiation Criterion - SLJ

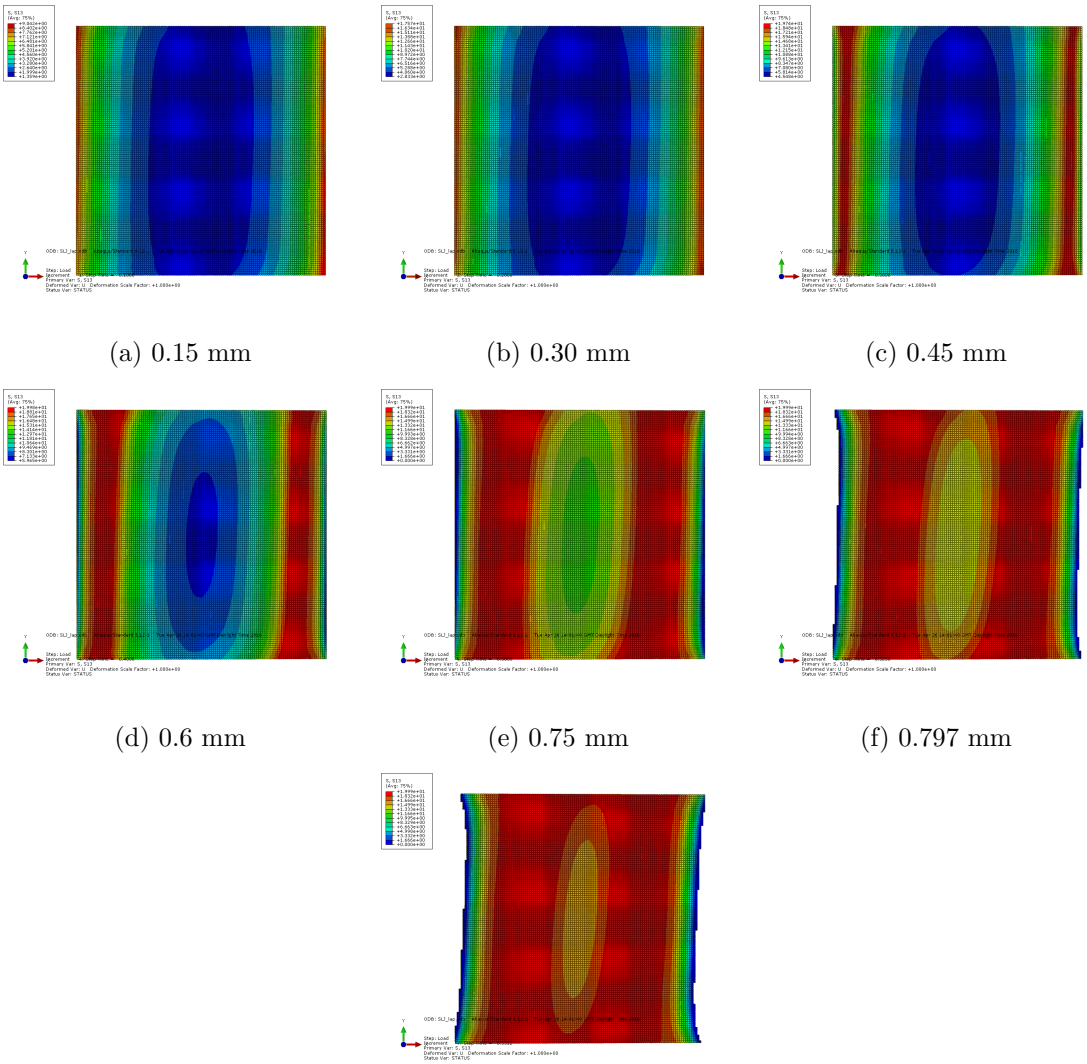

(a) 0.15 mm (b) 0.30 mm (c) 0.45 mm

(d) 0.6 mm (e) 0.75 mm (f) 0.797 mm

(g) 0.799 mm

Figure 8.64: Damage initiation criterion of adhesive overlap from SLJ along the increase of applied displacement;

Damage Initiation Criterion - SLJ+H

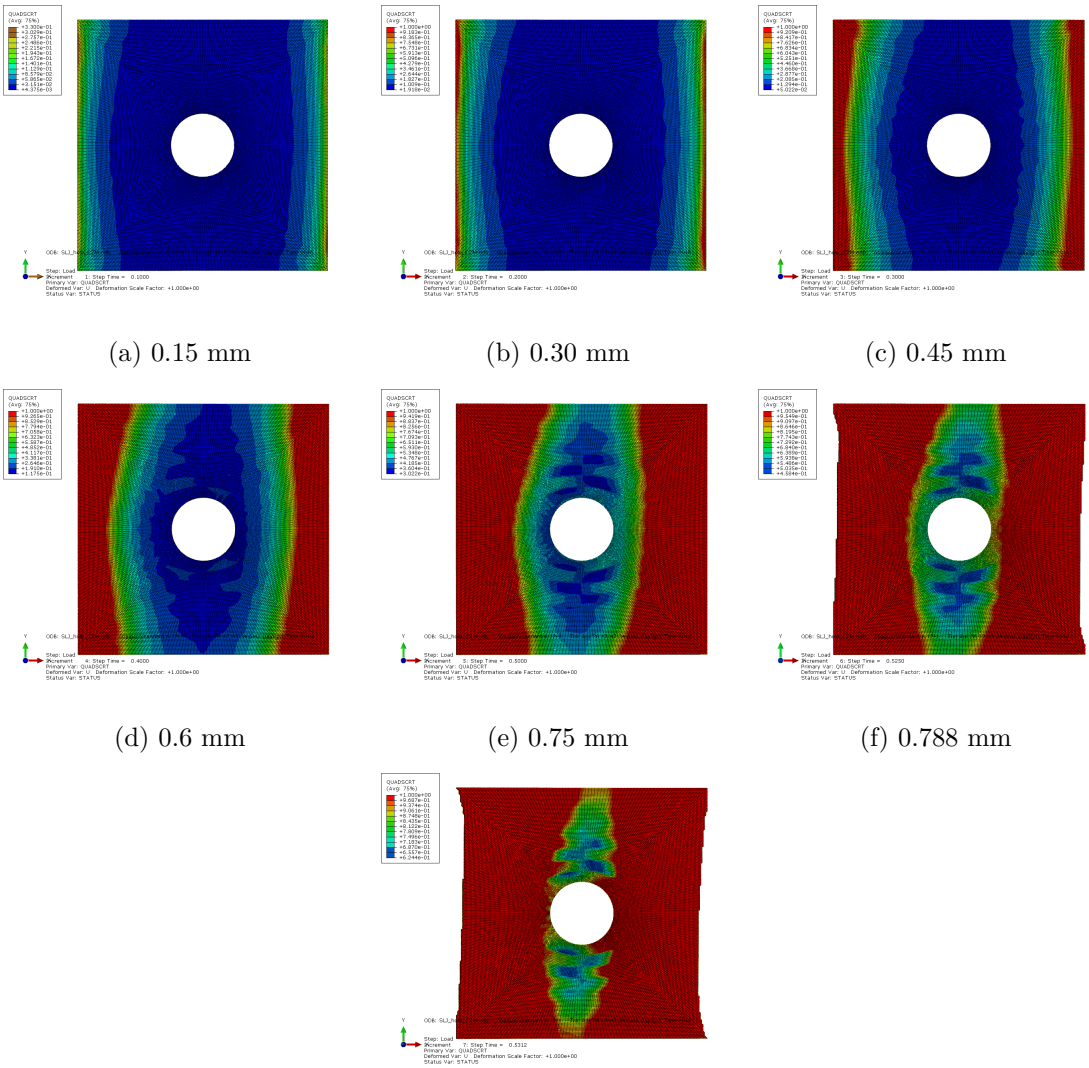

(a) 0.15 mm (b) 0.30 mm (c) 0.45 mm

(d) 0.6 mm (e) 0.75 mm (f) 0.788 mm

(g) 0.797 mm

Figure 8.65: Damage initiation criterion of adhesive overlap from SLJ+H along the increase of applied displacement;

Damage Initiation Criterion - CRM

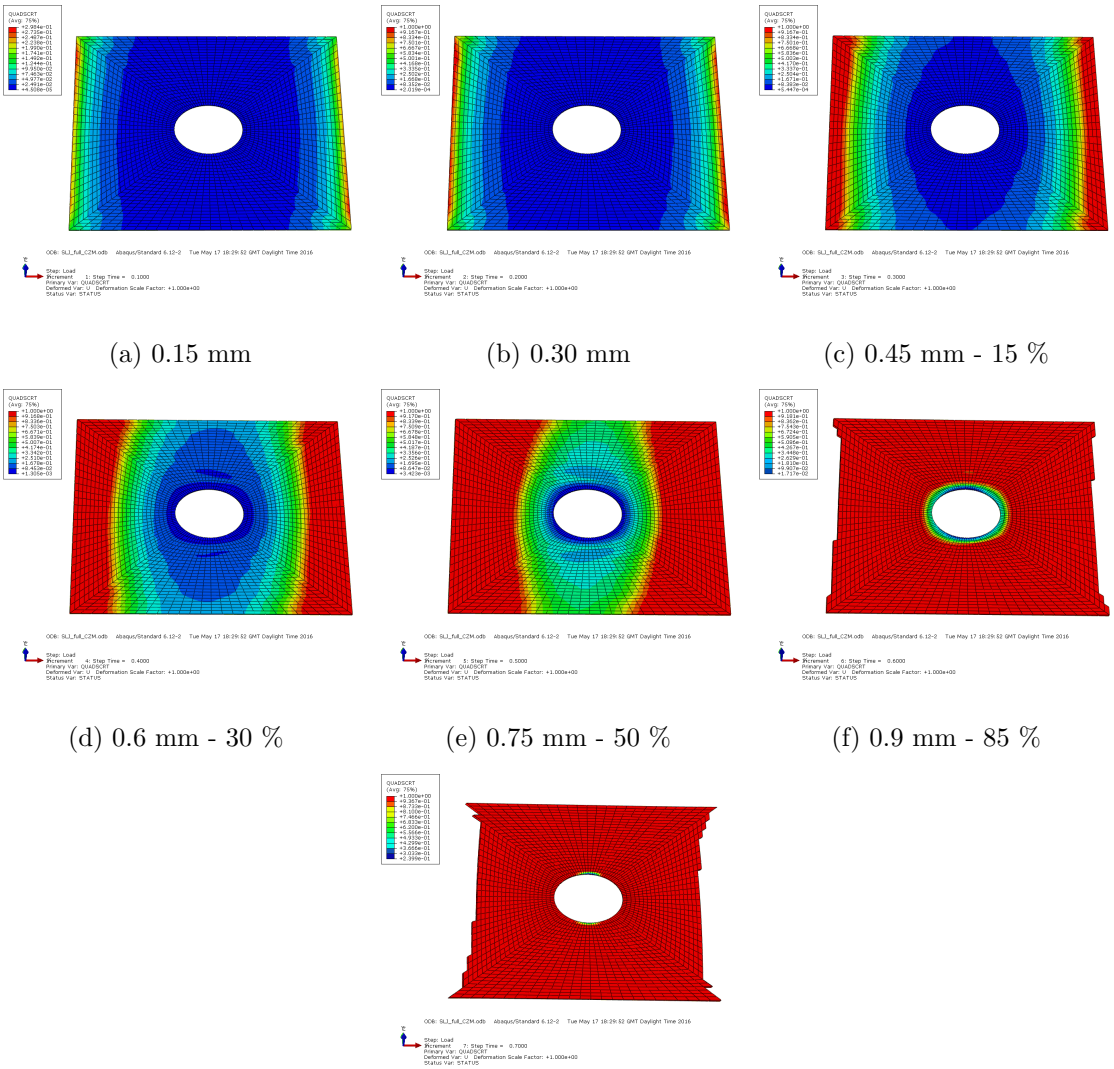

(a) 0.15 mm (b) 0.30 mm (c) 0.45 mm - 15 %

(d) 0.6 mm - 30 % (e) 0.75 mm - 50 % (f) 0.9 mm - 85 %

(g) 1.05 mm - 95 %

Figure 8.66: Damage initiation criterion of adhesive overlap from CRM along the increase of applied displacement/damage;

Damage Initiation Criterion - TRM

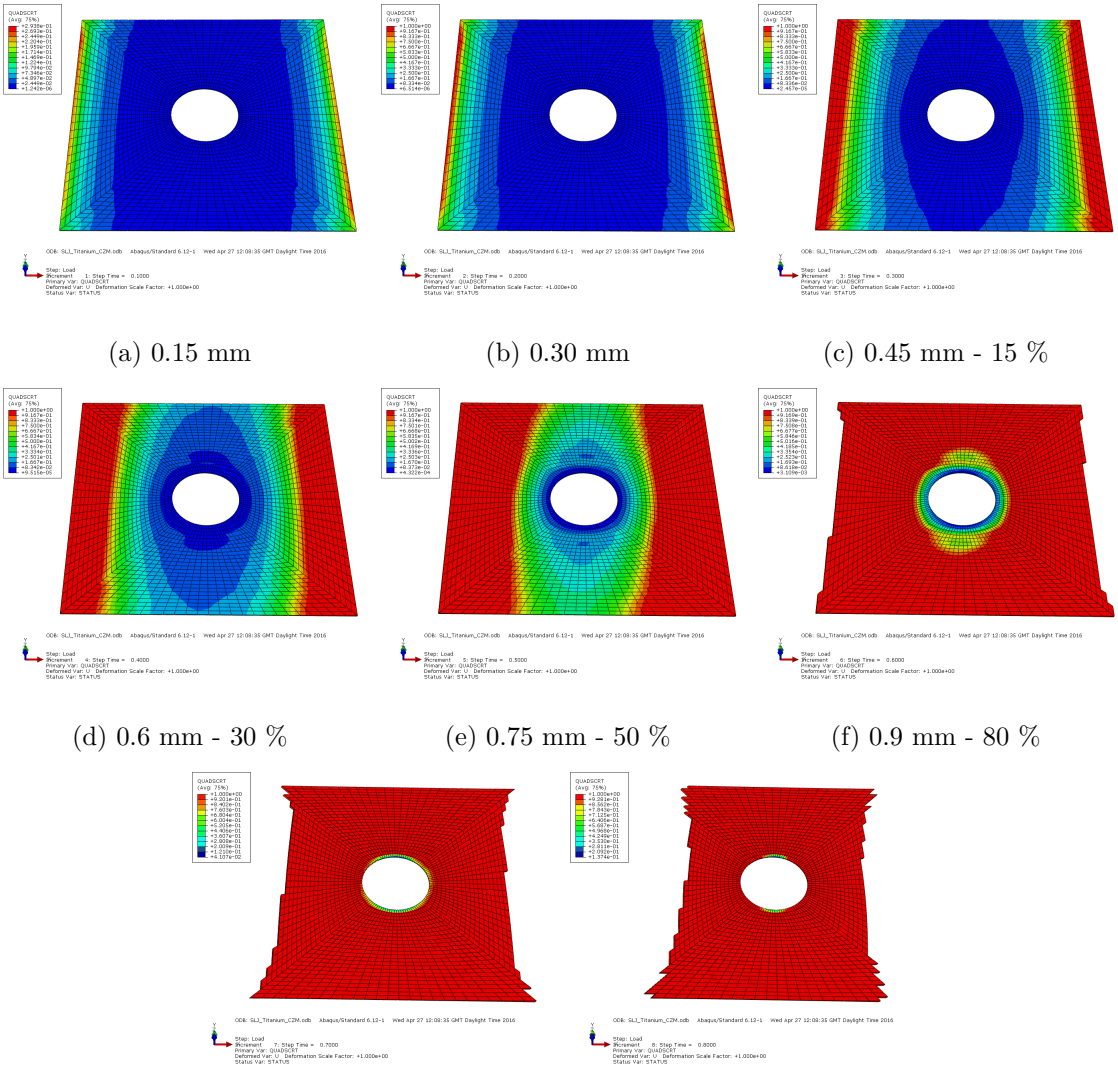

(a) 0.15 mm (b) 0.30 mm (c) 0.45 mm - 15 %

(d) 0.6 mm - 30 % (e) 0.75 mm - 50 % (f) 0.9 mm - 80 %

(g) 1.05 mm - 90 % (h) 1.20 mm - 95 %

Figure 8.67: Damage initiation criterion of adhesive overlap from TRM along the increase of applied displacement;

8.9 Appendix E

Stress distribution of composite rivets and rods

This appendix illustrates the pulling stress distribution of 6 rivets and 6 rods tested along the WBM. That representation was performed for each level of damage and designated according to the adopted nomenclature.

WBM

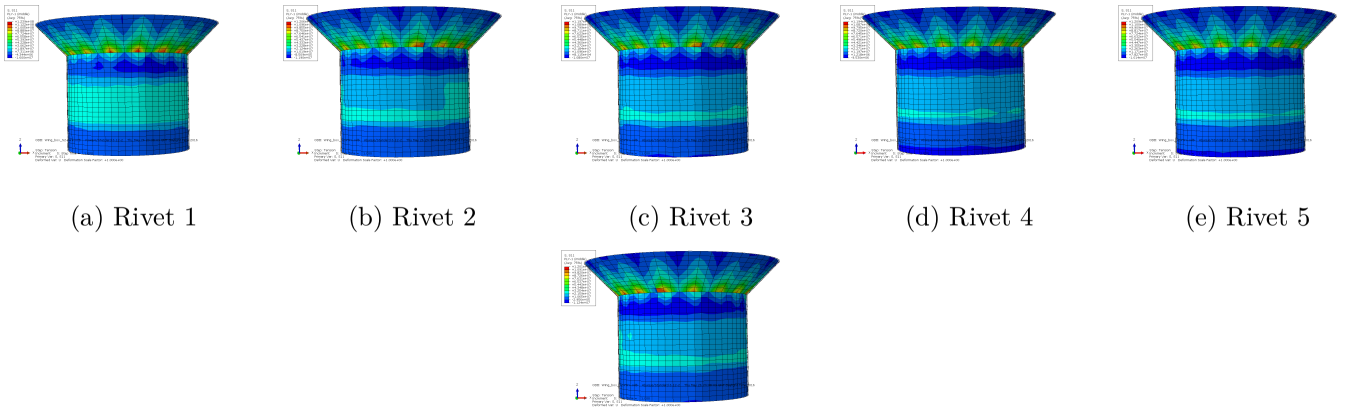

(a) Rivet 1 (b) Rivet 2 (c) Rivet 3 (d) Rivet 4 (e) Rivet 5

(f) Rivet 6

Figure 8.68: Pulling stress distribution of the rivets from WBM;

(a) Rod 1 (b) Rod 2 (c) Rod 3 (d) Rod 4 (e) Rod 5

(f) Rod 6

Figure 8.69: Pulling stress distribution of the rods from WBM;

WBDM I

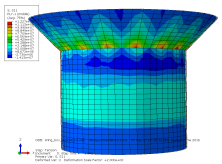

(a) Rivet 1

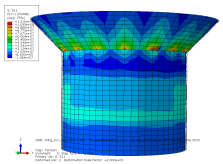

(b) Rivet 2

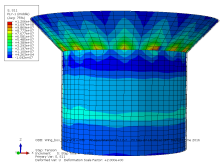

(c) Rivet 3

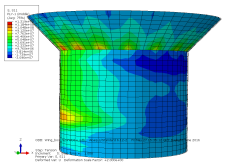

(d) Rivet 4

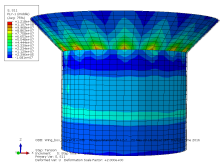

(e) Rivet 5

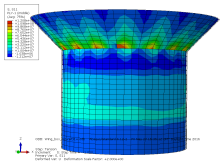

(f) Rivet 6

Figure 8.70: Pulling stress distribution of the rivets from WBDM I;

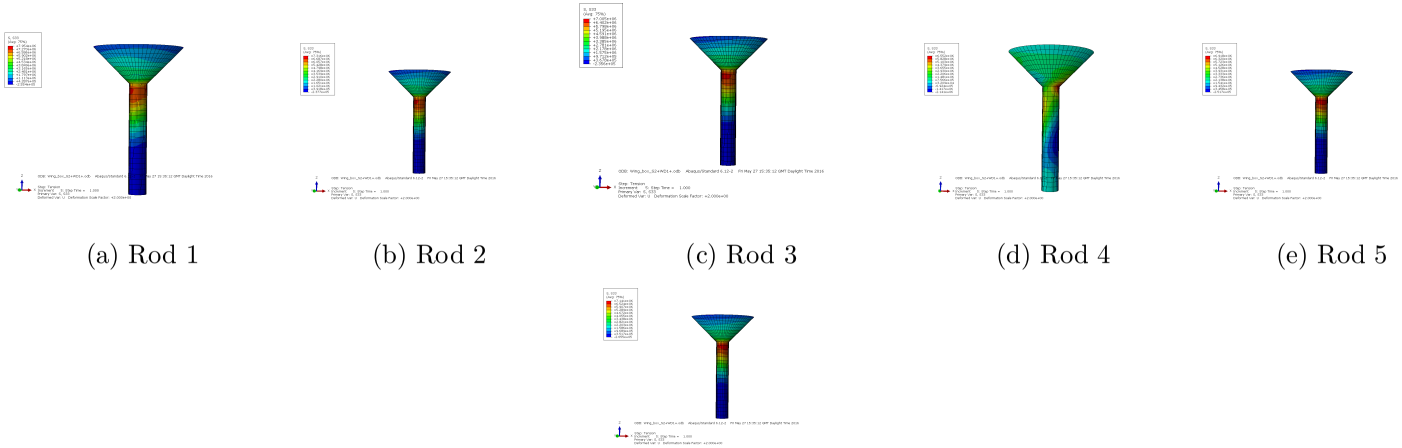

(a) Rod 1 (b) Rod 2 (c) Rod 3 (d) Rod 4 (e) Rod 5

(f) Rod 6

Figure 8.71: Pulling stress distribution of the rods from WBDM I;

WBDM II

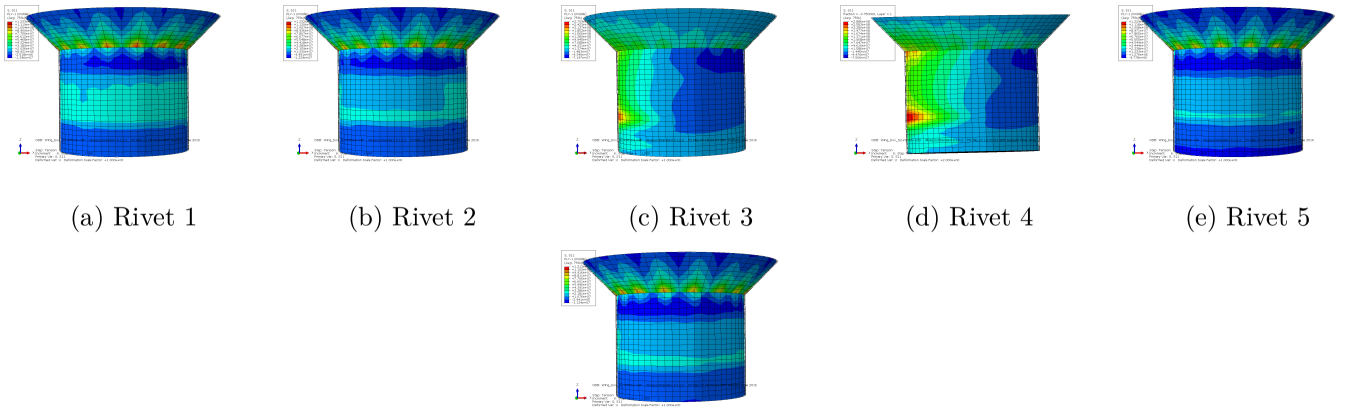

(a) Rivet 1 (b) Rivet 2 (c) Rivet 3 (d) Rivet 4 (e) Rivet 5

(f) Rivet 6

Figure 8.72: Pulling stress distribution of the rivets from WBDM II;

(a) Rod 1 (b) Rod 2 (c) Rod 3 (d) Rod 4 (e) Rod 5

(f) Rod 6

Figure 8.73: Pulling stress distribution of the rods from WBDM II;

WBDM III

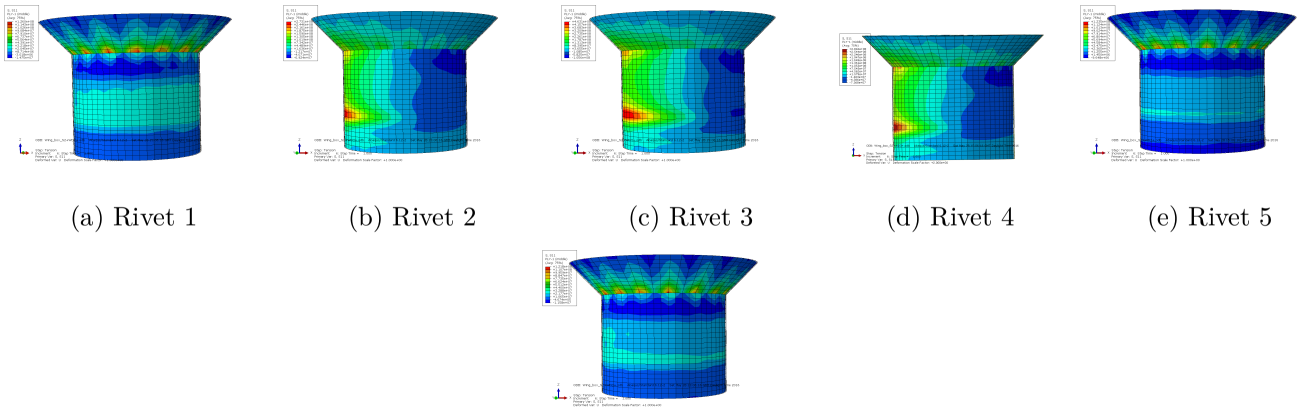

(a) Rivet 1 (b) Rivet 2 (c) Rivet 3 (d) Rivet 4 (e) Rivet 5

(f) Rivet 6

Figure 8.74: Pulling stress distribution of the rivets from WBDM III;

(a) Rod 1 (b) Rod 2 (c) Rod 3 (d) Rod 4 (e) Rod 5

(f) Rod 6

Figure 8.75: Pulling stress distribution of the rods from WBDM III;